

8-2019

# Cure Dependent Viscoelastic-Plastic Modeling of Adhesives to Capture CTE Effects in Multi-Material Structures

Akshat Agha

*Clemson University*, aagha@clemson.edu

Follow this and additional works at: [https://tigerprints.clemson.edu/all\\_dissertations](https://tigerprints.clemson.edu/all_dissertations)

---

## Recommended Citation

Agha, Akshat, "Cure Dependent Viscoelastic-Plastic Modeling of Adhesives to Capture CTE Effects in Multi-Material Structures" (2019). *All Dissertations*. 2466.

[https://tigerprints.clemson.edu/all\\_dissertations/2466](https://tigerprints.clemson.edu/all_dissertations/2466)

# **CURE DEPENDENT VISCOELASTIC-PLASTIC MODELING OF ADHESIVES TO CAPTURE CTE EFFECTS IN MULTI-MATERIAL STRUCTURES**

---

A Dissertation  
Presented to  
the Graduate School of  
Clemson University

---

In Partial Fulfillment  
of the Requirements for the Degree  
Doctor of Philosophy  
Automotive Engineering

---

by  
Akshat Agha  
August 2019

---

Accepted by:  
Dr. Fadi Abu-Farha, Committee Chair  
Dr. Srikanth Pilla  
Dr. Gang Li  
Dr. Garrett Pataky  
Dr. David Schmueser

# **ABSTRACT**

The effects of Coefficient of Thermal Expansion (CTE) mismatch in multi-material adhesive joints, induced during the manufacturing process, are expected to hinder the peak performance of the adhesive in the service life of the vehicle. With a goal to study and capture these effects, several innovative experimental techniques were performed to record and quantify the manufacturing process induced effects on an adhesive bonded multi-material joint. The tests to capture the effects of curing process on the structure were run at coupon level using a single lap shear geometry and at component level on a scaled-down automotive roof component. The other set of tests were done to determine the effect of manufacturing induced residual stresses on the performance of the adhesive joint.

This work then proposes a novel approach and a package of material models to model the properties of automotive adhesives during the heat curing process. The proposed material model package consists of a curing kinetics model, a cure and temperature dependent viscoelastic mechanical model and a temperature and rate dependent plastic model. The developed material models were coded into a user-defined material subroutine for LS-DYNA. The material card was used to run finite element simulations and was validated at coupon level and component level. The calibrated material models were fed into a finite element simulation and the prediction results were compared to the

experiments on a single lap shear joint and on a complex scaled-down roof component under different scenarios. A good agreement between the numerical and experimental data was achieved.

# **ACKNOWLEDGEMENTS**

First of all, I would like to express my gratitude to my advisor, Dr. Fadi Abu-Farha for his constant support and guidance during my study and research over the past three years at CU-ICAR. He was always energetic to help me with his great ideas to motivate me in my academic and personal life, whenever I needed a push. The most valued lesson I have learnt from him is to always think big and focus on the bigger picture. I would also like to thank my committee members, Dr. Srikanth Pilla, Dr. Gang Li, Dr. Garrett Pataky, and Dr. David Schmueser for their time and inspiring suggestions on my research and review of the manuscript.

I would like to take this opportunity to sincerely thank Dr. Tim Welters and Dr. Georges Romanos from Henkel Corporation, Germany for mentoring me during the project and providing their valuable technical inputs. Their expert comments and precious technical discussions helped me improve the quality of my research work. In addition, I cherished the collaboration experience and help of Dr. Rakan Alturk, Dr. Farbod Niaki, Nikhil, Abhishek, Deepak, Aravindhan, and all the other group mates. Furthermore, many thanks to the team of CU-ICAR engineers, Gary and Jeremy for helping me in preparing my test samples and being patient with me. I also appreciate the technical support from the Clemson University library and Palmetto cluster groups.

Finally, I would like to express my deepest thanks to my parents, my elder brother and my grandmother who had to put up with my physical and occasional mental absence.

Akshat Agha

# Table of Contents

<b>1. INTRODUCTION .....</b>	<b>1</b>
1.1 Motivation and Background .....	1
1.2 Problem, approaches and objectives.....	2
1.3 Outline of the thesis.....	7
<b>2. EXPERIMENTAL TECHNIQUES TO CAPTURE AND STUDY THE CURING INDUCED EFFECTS IN ADHESIVE BONDED STRUCTURES.....</b>	<b>9</b>
2.1 Introduction .....	9
2.2 Coupon level experiments to capture thermal effects during the heat curing process .....	13
2.2.1 Specimen geometry and materials .....	13
2.2.2 Experimental setup .....	15
2.2.3 Test Methodology .....	18
2.2.4 Results and Discussion .....	20
2.3 Experiments to evaluate the effects of residual stress on joint performance .....	26
2.3.1 Specimen geometry and materials .....	27
2.3.2 Experimental Setup.....	28

2.3.3 Results .....	30
2.3.4 Discussion.....	32
2.4 Component level experiments to capture curing induced effects .....	34
2.4.1 Experimental setup .....	34
2.4.2 Specimen Details.....	35
2.4.3 Test Process .....	39
2.5. Conclusion.....	40
<b>3. MATERIAL MODELING .....</b>	<b>42</b>
3.1 Introduction .....	42
3.2 Material Modeling .....	45
3.2.1 Curing Kinetics Model .....	46
3.2.2 Viscoelastic Model .....	50
3.2.3 Plastic Model.....	55
3.3 Experiments and model calibration.....	56
3.3.1 Calibration of curing kinetics model .....	56
3.3.2 Calibration of viscoelastic model .....	65
3.3.3 Calibration of plastic model.....	73
<b>4. USER-DEFINED MATERIAL SUBROUTINE (UMAT) IN LS-DYNA .....</b>	<b>79</b>

4.1 Implementation of viscoelastic material description .....	81
4.2 Implementation of plastic constitutive equation .....	86
4.3 Material card inputs and outputs .....	88
4.3.1 Inputs: .....	88
4.3.2 Outputs: .....	93
4.4 Material Card Verification:.....	94
4.4.1 Verification of curing kinetics model .....	94
4.4.2 Verification of viscoelastic model.....	95
4.4.3 Verification of viscoelastic-plastic coupled model .....	96
<b>5. FINITE ELEMENT SIMULATIONS AND MODEL VALIDATION .....</b>	<b>98</b>
5.1 Experiments for model validation at coupon level:.....	98
5.1.1 Finite element model:.....	99
5.1.2 Comparison of FE and experimental results.....	102
5.1.3 Computational results.....	108
5.1.4 Concluding remarks .....	110
5.2 Experiments for model validation at component level: .....	112
5.2.1 Finite Element Model.....	112
5.2.2. Comparison of FE predictions with experimental results .....	115

<b>6. CONCLUSIONS .....</b>	<b>125</b>
6.1 FEA prediction results .....	125
6.2 Concluding remarks .....	129
<b>7. REFERENCES .....</b>	<b>131</b>

# LIST OF FIGURES

Figure 1.1. A generalized automotive paint bake cycle.....	3
Figure 1.2 Effect of thermal expansion on an adhesive bonded structure .....	4
Figure 1.3 Research Motivation.....	7
Figure 2.1 Single lap shear joint specimen geometry, unbonded metal substrates and an uncured specimen.....	16
Figure 2.2 Force vs. strain curve for metal substrates – DP980 and AA7071 at room temperature.....	16
Figure 2.3 Specimen mounted on the INVAR grips and thermocouples attached at four locations.....	17
Figure 2.4 Test setup with furnace door closed (heating phase); with furnace door open (cooling phase).....	19
Figure 2.5 Surface temperature profiles obtained from the four thermocouples.....	21
Figure 2.6 Y-displacement contour map obtained from processing DIC results.....	24
Figure 2.7 Virtual extensometer of 30 mm length across the adhesive joint .....	25
Figure 2.8 Y-displacement on 30 mm gauge length across the joint for DP980 - AA7071 and AA7071 - AA7071 tests .....	25
Figure 2.9 Force measurements during the curing cycle for DP980 - AA7071 and AA7071 - AA7071 tests .....	26

Figure 2.10 Stress free (Type I) adhesive bonded single lap shear specimen preparation .....	28
Figure 2.11 Experimental setup for testing at 0.005/s and 0.5/s shear strain rates.....	29
Figure 2.12 Experimental setup for testing at 50/s fastest shear strain rate.....	30
Figure 2.13 Force-Strain curves for DP980-AA7071 lap shear specimens at shear strain rate of 0.005/s for stress free (type I) in blue and with residual stress (type II) in red....	31
Figure 2.14 . Force-Strain curves for DP980-AA7071 lap shear specimens at shear strain rate of 0.5/s for stress free (type I) in blue and with residual stress (type II) in red.....	31
Figure 2.15 Force-Strain curves for DP980-AA7071 lap shear specimens at shear strain rate of 50/s for stress free (type I) in blue and with residual stress (type II) in red.....	32
Figure 2.16 Comparison of force-strain curves for DP980-AA7071 lap shear specimens at shear strain rates of 0.005/s , 0.5/s and 50/s for stress free (type I) in blue and with residual stress (type II) in red .....	33
Figure 2.17 Experimental setup for component level validation on a scaled-down roof model .....	35
Figure 2.18 Steel frame, adhesive applied on the frame and aluminum flat panel mounted on the frame .....	36
Figure 2.19 Specimen with adhesive only, hard clamped at the top left corner .....	37
Figure 2.20 Joining process of friction element welds (Ejoweld) [Source: EJOT] .....	39
Figure 2.21 Specimen with adhesive and friction element welds.....	39

Figure 2.22 Thermocouple locations and temperature profile recorded on rear rail (1), rear panel (2), front panel (3) and front rail (4).....	40
Figure 3.1 Sample DSC heat flow scans normalized with specimen weight for different heating rates .....	58
Figure 3.2 Degree of cure vs. temperature obtained from DSC measurements on different heating rates .....	59
Figure 3.3 Degree of cure vs. time obtained from DSC measurements on different heating rates .....	59
Figure 3.4 Arrhenius plots and isoconversion line for $\alpha = 0.9$ .....	61
Figure 3.5 Activation energy variation with cure level, average activation energy ..	61
Figure 3.6 $f(\alpha)$ best fit curve for experimental curves .....	63
Figure 3.7 Comparison of model estimation vs experimental curves at non-isothermal condition .....	64
Figure 3.8 Comparison of model estimation vs experimental curves at isothermal condition .....	64
Figure 3.9 Shear storage modulus vs. frequency as a result of combined temperature- frequency sweep.....	67
Figure 3.10 Master curve showing shear storage, loss modulus and loss factor at 100 °C .....	68
Figure 3.11 Comparison of Log of experimental shift factors and WLF model estimation .....	69

Figure 3.12 Comparison of Prony series fitting vs experimental values .....	69
Figure 3.13 Development of shear modulus with time for a temperature ramp of 5oC/min .....	71
Figure 3.14 Development of shear modulus with time for a temperature ramp of 10oC/min .....	71
Figure 3.15 Comparison of experimentally obtained modulus growth with cure vs model estimation .....	72
Figure 3.16 Adhesive sheet preparation – cured between two steel sheets.....	73
Figure 3.17 Tensile specimen preparation using specially prepared die .....	74
Figure 3.18 Test setup for high temperature tensile tests on adhesives .....	75
Figure 3.19 Stress-Strain curves for the adhesive EP5089 at different temperatures at strain rate 0.001/s.....	75
Figure 3.20 Stress-Strain curves for the adhesive EP5089 at different strain rates at room temperature.....	76
Figure 3.21 Experiment vs. J-C model fit for stress-strain curves at different temperatures .....	77
Figure 3.22 Experiment vs. J-C model fit for stress-strain curves at different strain rates .....	77
Figure 4.1 General Approach for UMAT development.....	80
Figure 4.2 FE model results vs. mathematically calculated results for degree of cure ....	95

Figure 4.3 Single Element FE model; Comparison of FE model results vs. Prony series expansion .....	96
Figure 4.4 Viscoelastic-plastic model performance in FE simulation (dashed lines) vs. experimental stress-strain curves (solid lines); Geometry used for FE simulation .....	97
Figure 5.1 Lap shear joint geometry used for the experiments and FE model .....	101
Figure 5.2 Experimental setup; finite element model with 4 temperature regions carrying different temperature profiles; four thermocouple positioned on the grip rods and substrates.....	102
Figure 5.3 FE model showing 30 mm extensometer across the joint .....	102
Figure 5.4 Comparison of DIC measurements for Delta Y (30mm GL) vs. FE estimation for DP980-AA7071.....	104
Figure 5.5 Comparison of DIC measurements for Delta Z (30mm GL) vs. FE estimation for DP980-AA7071.....	105
Figure 5.6 Comparison of experimentally measured force vs. FE estimation for DP980-AA7071.....	105
Figure 5.7 Comparison of DIC measurements for Delta Y (30mm GL) vs. FE estimation for AA7071-AA7071.....	106
Figure 5.8 Comparison of DIC measurements for Delta Z (30mm GL) vs. FE estimation for AA7071-AA7071.....	107
Figure 5.9 Comparison of experimentally measured force vs. FE estimation for AA7071-AA7071.....	107

Figure 5.10 FE model prediction of residual stresses for 0.2 mm, 0.3 mm and 0.4 mm adhesive bead for DP980-AA7071 .....	109
Figure 5.11 FE model prediction of residual stresses for 0.2 mm, 0.3 mm and 0.4 mm adhesive bead for AA7071-AA7071 .....	109
Figure 5.12 FE predicted contour plots of effective stress in the substrates and residual stress in the adhesive for 0.2 mm, 0.3 mm and 0.4 mm adhesive bead (top to bottom) for DP980-AA7071 .....	111
Figure 5.13 Finite element model I with adhesive only, clamped on the top left corner .....	113
Figure 5.14 Material properties entered in FEA for aluminum panel and steel clamp and friction element welds .....	114
Figure 5.15 Finite element model II with adhesive and mechanical fixations .....	115
Figure 5.16 Points selected for comparison between the test and FE predictions.....	116
Figure 5.17 X-displacement prediction from finite element model vs. DIC generated values for Model I .....	119
Figure 5.18 Y-displacement prediction from finite element model vs. DIC generated values for Model I .....	119
Figure 5.19 Z-displacement prediction from finite element model vs. DIC generated values for Model I .....	120
Figure 5.20 X-displacement prediction from finite element model vs. DIC generated values for Model II .....	123

Figure 5.21 Y-displacement prediction from finite element model vs. DIC generated values for Model II .....	124
Figure 5.22 Z-displacement prediction from finite element model vs. DIC generated values for Model II .....	124
Figure 6.1 Effective stress in the adhesive bond for model I: with adhesive only (left) and model II: with adhesive and mechanical fixations (right).....	126
Figure 6.2 Z-displacement in the aluminum panel at the end of heating cycle for model I: with adhesive only (left) and model II: with adhesive and mechanical fixations (right) 127	
Figure 6.3 Z-displacement in the aluminum panel for a full size 1:1 roof component with adhesive and mechanical fixations .....	128
Figure 6.4 Effect of the choice of adhesive on the adhesive bond and the body structure stiffness .....	129

# LIST OF TABLES

Table 2.1 Properties of the used adhesive Teroson EP 5089 .....	14
Table 3.1 Literature survey on curing kinetics models .....	49
Table 3.2 List of works on viscoelastic modeling of polymers.....	51
Table 3.3 Calibrated parameters for curing kinetics model .....	63
Table 3.4 Parameters obtained for best fit of WLF function: Eq. (4) and Prony series: Eq. (5) .....	70
Table 3.5 J-C model parameters for EP5089 adhesive .....	76
Table 5.1 Material properties for substrates and INVAR grips used in the FE model ....	101

**THIS PAGE IS INTENTIONALLY LEFT BLANK**

# **Chapter 1**

## **1. INTRODUCTION**

### **1.1 Motivation and Background**

Enhanced concerns associated with increasing levels of emission of local pollutants (such as SO<sub>2</sub> and NO<sub>x</sub>) and global greenhouse gases (such as CO<sub>2</sub>) have resulted in the enforcement of the aggressive CAFÉ 2025 standards. Such ambitious standards have pushed the auto industry towards achieving enhanced fuel economy targets via a variety of strategies; vehicle lightweighting considered as one of the most effective and thus attractive choices. In an automotive body dominated by different grades of steels, significant weight reduction is possible by material substitution. However, the most suitable advanced lightweight materials, like aluminum and reinforced plastics, come at an increased price. To strike a balance between weight reduction benefits and cost, multi-material body construction serves as a viable solution. Regrettably, this solution – i.e. use of multi-material Body-in-White (BIW) design- is strongly affected by the difficulties

associated with multi-material joining where conventional joining techniques (like spot-welding) fail to deliver .

Adhesive Bonding is a viable method for joining dissimilar materials (ferrous metals, non-ferrous metals, fiber reinforced plastics, and others); it enables high performance and flexible joints while eliminating the weight and cost of fasteners (bolts, screws, rivets, etc.) associated with mechanical joining techniques (Tim Welters 2013, Bihamta 2017). It is therefore that structural adhesives and sealants have been used extensively, and their use continues to grow, in automotive body structures.

## **1.2 Problem, approaches and objectives**

The paint baking process of the body in white, which is also used for heat curing the adhesive, lasts approximately 30 minutes. As the body passes through the paint baking oven, the temperature of the body rises sharply to the range of 160-180°C and stays at that level for around 20 minutes before slowly cooling down to room temperature as shown in *Figure 1.1*. The paint baking cycle can hence be divided into (i) heating phase, when the body temperature rises, substrates expand freely and the adhesive slowly starts to cure, (ii) isothermal phase, when the adhesive cures hardens to a viscoelastic solid, while the substrates are in an expanded state (iii) cooling phase, when the temperature starts cooling and substrates start to contract to their initial state.

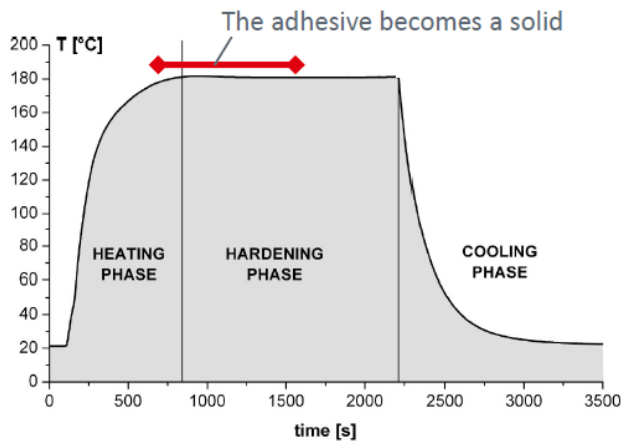


*Figure 1.1. A generalized automotive paint bake cycle*

The fact that structural adhesives need to be heat cured poses a critical problem pertaining to the differences in the coefficient of thermal expansion (CTE) of the joined parts; the mismatch of which has significant implications on the integrity and response of the BIW to external loading (mainly thermal). For example shown in *Figure 1.2*, a 1 m wide floating aluminum roof panel can expand by ~2.5 mm on each side at the maximum curing temperature (approximately 200 °C); steel roof bows of similar span would expand by ~half the magnitude simply because of the lower CTE value. As the adhesive cures at the peak temperature, it constraints the contraction in the substrates during the cooling down phase. This (when extended to all components and different joints in a BIW) leads to distortion in the structure, and more importantly residual stresses in the adhesive-bonded joints.

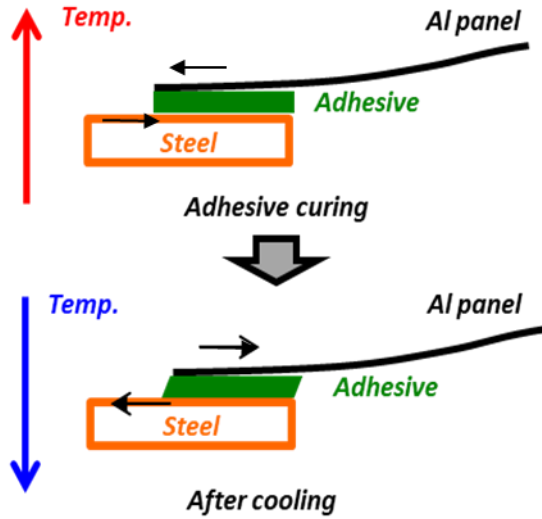


*Figure 1.2 Effect of thermal expansion on an adhesive bonded structure*

One of the main challenges when joining dissimilar material combinations like this is the assessment of the level and magnitude of residual stresses developing in the adhesive-bonded joint during the manufacturing process. Yet, it can be said with certainty that the presence of such residual stresses is detrimental to the performance of the adhesive bond and thereby of the automobile body structure during the service life of the vehicle, particularly in case of a crash event. Therefore, the use of adhesive-joined multi-material structures in the body of an automobile is hindered by the lack of information on the value and extent of residual stress developed in the bond. Due to the absence of any reliable and practical experimental techniques to measure residual stresses in adhesive-bonded joints, it is necessary to use numerical models to estimate such stresses to

account for changes that need to be made to render the car body safe in case of extreme events.

For the application of adhesives in automotive structures subjected to crash loading, it is also important to consider the rate dependent material properties of both substrates and the adhesives. Moreover, it has been shown in the literature that similar to most metals, the yield strength of an adhesive changes at high strain rates. This work attempts to study the rate dependent effects of residual stresses on the performance of the adhesive joint, which is a first for an automotive grade structural adhesive.

Automotive grade structural adhesives are predominantly epoxy based (thermoset) adhesives. The mechanical properties of the adhesive joint are entirely dependent on an internal variable called “the degree of cure ( $\alpha$ )”, which can be calculated using Differential Scanning Calorimetry (DSC) and modeled by curing kinetics models based on the temperature-time history (during a paint baking cycle). Several mechanical models (like Generalized Maxwell Model) are available in the literature which are capable of linking the degree of cure and its impact on properties, making them suitable to analyze the viscoelastic nature of certain materials (such as epoxies). However, these models are not entirely useful for structural adhesives that exhibit temperature-dependent viscoelastic-plastic properties upon full cure. The tests on fully cured adhesives show that they exhibit temperature dependent plastic behavior in addition to viscoelastic properties.

The study targets to fill the gap and develop a temperature and cure dependent viscoelastic-plastic material model, which can predict the cure-history dependent true response of adhesive joints – the first for automotive adhesives.

The cutting-plane algorithm was used for integrating the viscoelastic and plastic constitutive models to define the yield function. The model was coded into a user defined material subroutine (UMAT) in LS-DYNA. The performance of the material card was evaluated at coupon level by simulating a tensile specimen at various temperatures. The material card was then validated at component level by comparing the simulation results with a unique set of experiments on a small scale automotive roof model. The displacements in the heating phase and the distortions after the cooling phase were used to compare the finite element and experimental results.

It is precisely this task of developing a suitable numerical model that addresses all the aforementioned concerns that is sought to be accomplished in this work. The motivation for the research is pictorially shown in *Figure 1.3*. Exhaustive literature review has been undertaken on the published curing kinetics models, viscoelastic material models, high strain-rate fracture models, and a detailed understanding of the advantages and limitations of each of these models has been established. Based on this, a cure history dependent viscoelastic-plastic model for adhesives is sought to be developed that can: (a) evaluate the effects of heat curing process during manufacturing; and (b) aid in assessing

the impact of induced effects on the peak performance of the adhesive joints during the service life of the vehicle in extreme temperatures and crash conditions.

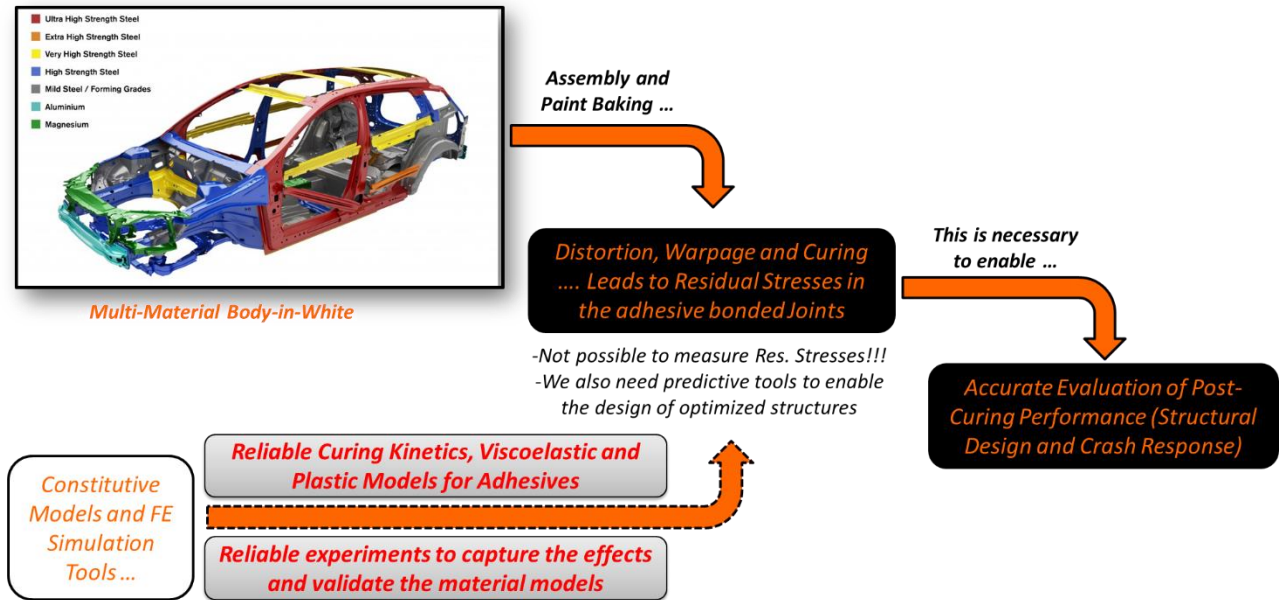


Figure 1.3 Research Motivation

### 1.3 Outline of the thesis

The presented dissertation consists of six chapters. Each chapter addresses one specific topic. Chapter 2 discusses some unique experiments to capture the behavior of substrates and adhesive during the heat curing process. The tests include simple tests at coupon level on a single lap shear joint using similar and dis-similar combination of metallic substrates, and more complex tests on component level involving scaled-down roof component with and without mechanical fixations. Another set of experiments tries to

evaluate the effect of manufacturing induced residual stresses on the performance of the adhesive joint.

Chapter 3 develops a suite of material models for adhesives to capture the curing process induced effects. The material models include a curing kinetics model, viscoelastic model, plastic model which work together to predict the behavior of the adhesive during and post curing process. The proposed material models are calibrated using differential scanning calorimetry (DSC) tests for curing kinetics, dynamic mechanical analysis (DMA) for viscoelastic, and tensile tests for plastic models. The approach used to calibrate the material models from the experimental data is shared.

Chapter 4 presents the theory behind the discussed material models and formulation for coding the developed models into a user-defined material subroutine in LS-DYNA. It also consists of simple simulations to verify the correctness of the material card on known set of experiments.

Chapter 5 consists of finite element simulations using the developed material card. The simulations are performed to validate the developed material card on single lap shear joint tests and scaled-down roof component tests, discussed in chapter 2.

Chapter 6 presents some conclusions derived from the study. It also suggests some design recommendations for adhesive bonded multi-material structures.

# **Chapter 2**

## **2. EXPERIMENTAL TECHNIQUES TO CAPTURE AND STUDY THE CURING INDUCED EFFECTS IN ADHESIVE BONDED STRUCTURES**

### **2.1 Introduction**

Enhanced concerns associated with increasing levels of emission of local pollutants (such as SO<sub>2</sub> and NOX) and global greenhouse gases (such as CO<sub>2</sub>) have driven the automotive industry towards producing enhanced fuel efficient vehicles. This is achieved by a variety of strategies with vehicle lightweighting considered as one of the most effective and thus attractive choices. In an automotive body dominated by different grades of steels, significant weight reduction is possible by material substitution. However, the most suitable advanced lightweight materials, like aluminum and reinforced plastics, come at an increased price. To balance out the weight reduction benefits and cost, multi-material body construction serves as a viable solution. Regrettably, this solution – i.e. use of multi-material Body-in-White (BIW) design- is strongly affected by the difficulties associated

with multi-material joining where conventional joining techniques (like spot-welding) fail to deliver.

Adhesive Bonding is a viable method for joining dissimilar materials (ferrous metals, non-ferrous metals, fiber reinforced plastics, and others); it enables high performance and flexible joints while eliminating the weight and cost of fasteners (bolts, screws, rivets, etc.) associated with mechanical joining techniques. It is therefore that structural adhesives and sealants have been used extensively, and their use continues to grow, in automotive body structures. Nevertheless, the fact that automotive structural adhesives need to be heat cured poses a critical problem pertaining to the differences in the coefficient of thermal expansion (CTE) of the joined parts; the mismatch of which has significant implications on the integrity and response of the BIW to external loading (mainly thermal).

As per the current trend in automotive industry, adhesive curing is combined with paint baking process considering the manufacturing process time and economic reasons. At an elevated temperature in the paint baking oven, the different components of the body structure expand at different rates and magnitudes depending on their different CTE and different air convection properties in local areas. After the adhesive is cured at the peak temperature, it constraints the thermal contraction in the components during the cooling down phase. This (when extended to all components and different joints in a BIW) leads to distortion in the structure, and more importantly residual stresses in the adhesive-

bonded joints. It is well established that the presence of such residual stresses is detrimental to the performance of the adhesive bond and thereby of the automobile body structure during the service life of the vehicle, particularly in case of a crash event.

Several authors in the past have experimentally shown the effects of residual stresses in adhesive bonded joints. Reedy et al. (Reedy and Guess 1996) studied the effect of fabrication residual stresses on the strength of a butt joint considering stress relaxation behavior of the adhesive at different temperatures. They concluded that the effects of the stresses diminish with time due to relaxation behavior of the adhesives. Kim and Lee (Kim and Lee 1998) found that the load bearing capability of an adhesive bonded joint is greatly influenced by the fabrication residual thermal stresses. Apalak et al. (M. Kemal Apalak \* 2002) showed that the thermal mismatch between the substrates can result in huge thermal strains and affect the adhesive bonded joint. Yu et al. (Yu, Ashcroft et al. 2006) studied the residual stresses due to curing shrinkage and thermal expansion in epoxy-steel bi-material beams. Kropka et al. (Jamie M. Kropka 2013) investigated the role of residual stress on joint strength on a napkin-ring joint geometry. Experimental investigations done by Teutenberg (Meschut, Hahn et al. 2014) show the effect of residual stress in a lap shear joint compared to a stress free joint at different degrees of cure of the adhesive. The results showed a considerable decrease in the displacement across the joint before fracture, along with a decrease in maximum force. Ma et al. (Ma, Tian et al. 2018) studied the effect of several curing curves on the residual stresses generated in the high-temperature phosphate adhesive bonded joint on a single lap joint.

In this chapter, three types of experiments are discussed:

- I. First, an innovative experimental approach is shown to capture the effects of heat curing on an adhesive bonded single lap shear joint during the curing process using optical measurement technique. The tests were conducted on two metal substrate combinations using an automotive grade structural adhesive.
- II. Then the effects of residual stresses on the strength of single lap shear joints at different strain rates are discussed. The joints with residual stresses produced using the mentioned approach in (i) were tested in tension and the performance of the joints with residual stress was compared to stress free joints. The highlight of this work is that the test were performed at three different shear strain rates ranging from low (0.005/s) to high (50/s).
- III. The approach used in the first type of tests on coupon level was then extended to a more complex scaled-down component level. The tests were conducted on an adhesive bonded roof component in two scenarios. First, the tests were done with adhesive only and second, the tests were done with adhesive and mechanical fixations on the periphery of the roof panel.

The experimental data generated by the discussed approach in this chapter will be very valuable to understand the thermal effects in the joint during the curing process which will aid in more accurate modeling of adhesive joints. And, the effects of the residual

stresses at different strain rates will help in studying the significance of the fabrication residual stresses at low to high strain rates, like in the case of a crash event.

## **2.2 Coupon level experiments to capture thermal effects during the heat curing process**

The automotive paint baking cycle, which is also used for curing the adhesives lasts approximately for 30 minutes. When the body in white passes through the paint baking oven, the temperature of the body structure rises to the range of 160-180°C, and then slowly cools down to room temperature (R.A. Dickie\* 1997). The duration and temperature of the paint baking cycle is specific to each automotive manufacturer. In this work, the test aimed to reproduce the effects caused by thermal expansion of similar and dissimilar substrates in an adhesive joint during the adhesive curing process in the automotive paint bake cycle. A testing approach was developed to capture the thermal displacements in an uncured specimen during the curing process, using digital image correlation (DIC). The test results provide insight about the relative displacement of substrates during the adhesive curing process.

### **2.2.1 Specimen geometry and materials**

The tests were conducted on adhesive bonded single lap shear joints as shown in *Figure 2.1*. The specimen consisted of two metal substrates joined by an adhesive layer. The substrates were 100 mm long and 20 mm wide. The overlap area of the adhesive bond

was 20x20 mm<sup>2</sup>. The thickness of the adhesive layer was controlled at t=0.30 mm by adding a very small quantity of solid glass microspheres in the adhesive.

The tests were run for two sets of substrate combinations. (i) Multi-material combination of DP980 steel and aluminum alloy AA7071; (ii) Similar material combination of aluminum alloy AA7071 with itself. The thickness of DP980 sheet was 1.42 mm while the thickness of AA7071 sheet was 2.55 mm. The mechanical properties of the used metal substrates at room temperature were obtained by standard uniaxial tension tests and are given in *Figure 2.2*. The metal substrates were carefully chosen based on a high yielding force value, in order to make sure that the substrates do not yield before the adhesive bond.

The adhesive used for the study was an automotive grade structural adhesive Henkel Teroson EP 5089, provided by Henkel Corporation. It is a heat curing, single component adhesive, based on toughened epoxy resin. It is specially developed to provide high peel and impact peel resistance over wide temperature range and is optimized for high crash forces. The mechanical properties of the adhesive as per the technical data sheet are shown in *Table 2.1*.

Young's Modulus (ISO 527-1)	1.6 GPa
Tensile Strength (ISO 527-1)	35 MPa
Shear Strength (DIN EN 1465)	>20 MPa
Elongation at break (ISO 527-1)	10%
Poisson Ratio	0.4

*Table 2.1 Properties of the used adhesive Teroson EP 5089*

## 2.2.2 Experimental setup

The experimental setup used for testing was built on an Instron universal load frame, similar to a tensile test configuration.

**Furnace:** The tests were performed on a specialized setup which consisted of a furnace installed on the universal load frame. The setup was arranged to have the mounting grips and the specimen inside the furnace to simulate automotive paint baking oven conditions. The furnace was designed to have a small glass window opening in the front door through which the specimen was monitored using DIC system. The furnace was capable of maintaining a temperature of up to 450°C.

**Grips:** The grip rods used in the test were made of nickel-iron alloy (INVAR) to minimize the thermal expansion in the grips. The grips were designed in such a way that they self-aligned the specimen and prevented rotation in the uncured specimen. The specimen mounts consisted of two holes which were used to hold each substrate in the proper orientation. A picture of the specimen mount is shown in *Figure 2.3*.

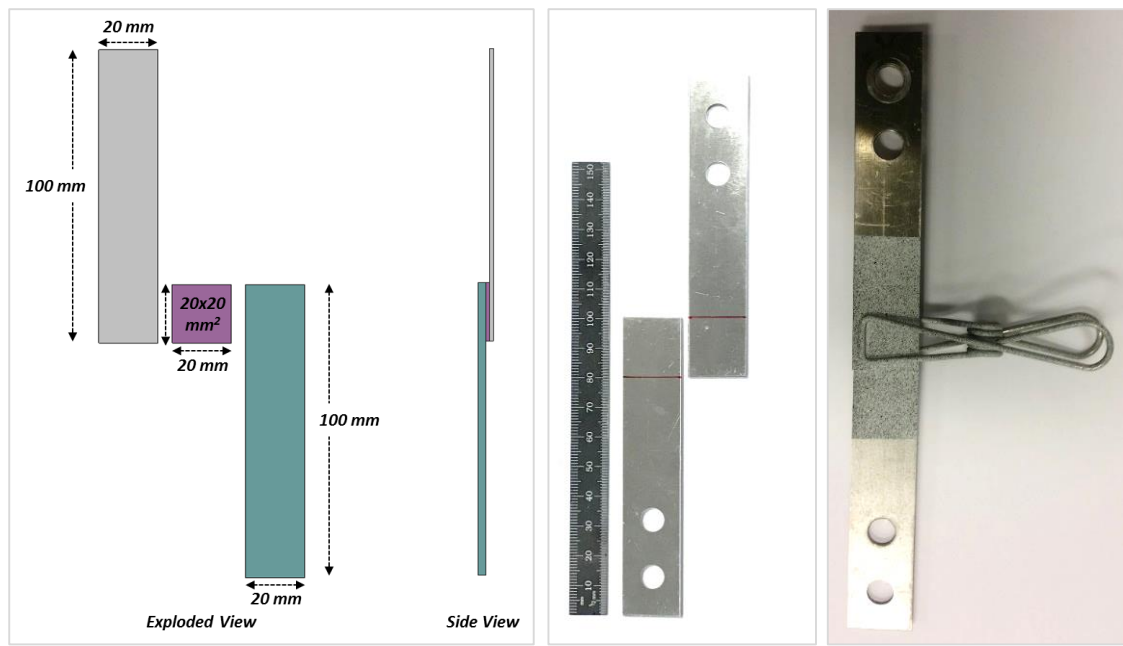


Figure 2.1 Single lap shear joint specimen geometry, unbonded metal substrates and an uncured specimen

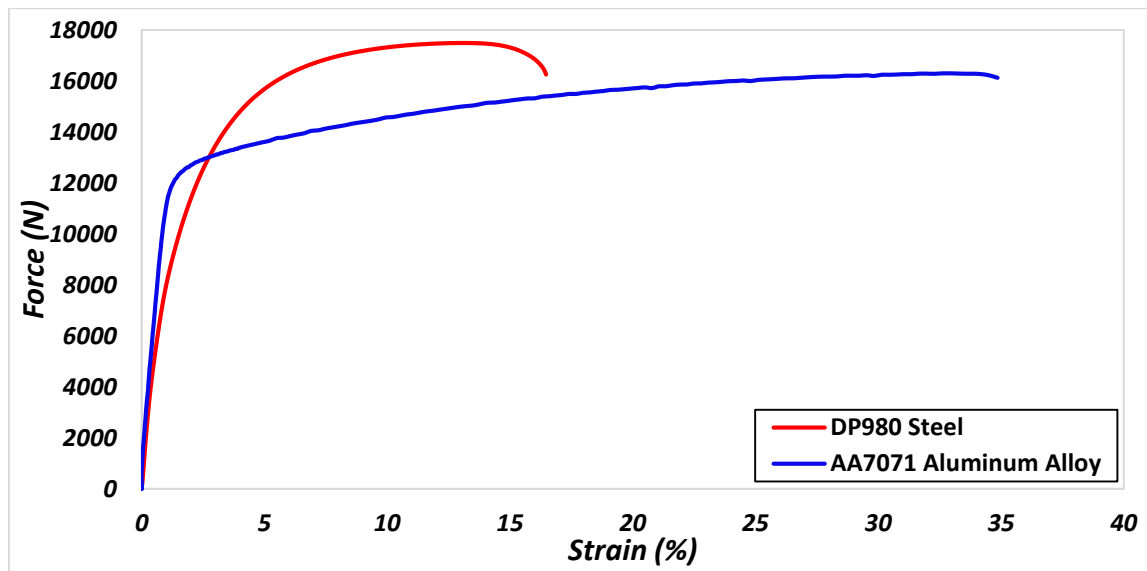


Figure 2.2 Force vs. strain curve for metal substrates – DP980 and AA7071 at room temperature



*Figure 2.3 Specimen mounted on the INVAR grips and thermocouples attached at four locations*

**Measurement devices:** There were three systems running in sync with each other, (i) DIC system for displacement measurement, (ii) temperature logger for temperature profile, (iii) load cell for force measurement.

- (i) Temperature measurement: Due to the design of the furnace and nature of hot air, the air at the top is always hotter than the bottom. Therefore, different portions of the grips and specimen experience different temperature profiles. Four K-type thermocouples were attached to the top grip, top substrate, bottom substrate and bottom grip to measure the surface temperature at four distinct points, as shown in *Figure 2.3*.

- (ii) DIC system: Digital Image Correlation (DIC) is an optical strain measuring technique, which makes use of cameras and image processing to derive 3D strains. The cameras capture the images of the specimen at a pre-defined frequency and the DIC software then compares the whole set of images (called as stages) to the reference stage, to determine the movement of the substrates with respect to time. In the test setup, Gom Aramis 5M system DIC system was used to capture the displacement in the substrates during the paint baking cycle.
- (iii) Force measurement: The top grip rod was attached to a 250kN load cell attached to the Instron load frame, to capture the tensile or compressive forces exerted by the specimen due to thermal expansion or contraction during the test.

### **2.2.3 Test Methodology**

The experiment was performed in two stages: (i) heating phase, and (ii) cooling phase.

- (i) Heating Phase: A single lap shear joint was prepared by applying adhesive on the mating surfaces of the two substrates. Spacer grade soda lime glass beads of 0.2 mm were added to the adhesive to ensure a minimum 0.2 mm thickness of the adhesive bead. The specimen was held together by a paper clip. Before mounting the specimen on the grips, a target region of 50 mm length across the joint was painted in black and white speckle pattern as per the DIC

standard, shown in *Figure 2.1*. The thermocouples were attached to the specimen and the grip rods and the furnace controller was set to 185°C. The heating phase was performed for 40 minutes and then the furnace door was opened for the cooling phase.

- (ii) Cooling Phase: In the cooling phase, the specimen was slowly cooled by natural cooling and the test was stopped when the temperature reading for all the thermocouples read 30°C.

The thickness of the adhesive joint for each specimen was measured after the test. The thickness of the adhesive bead was obtained by subtracting the thickness of the two substrates from joint thickness.

A picture of the complete test setup in heating and cooling phase is shown in *Figure 2.4*.

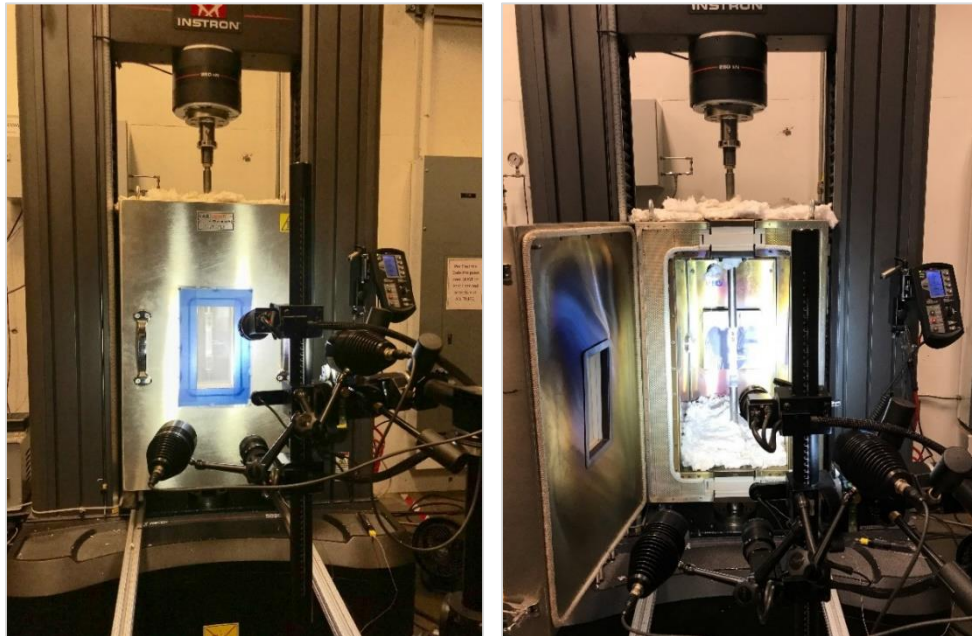


*Figure 2.4 Test setup with furnace door closed (heating phase); with furnace door open (cooling phase)*

## **2.2.4 Results and Discussion**

The temperature data from temperature logger, displacement data from DIC and the force data from the load cell were cross-referenced and studied together to get a holistic picture of the phenomenon due to thermal expansion during the adhesive curing process.

### **2.2.4.1 Temperature profiles**

A sample of the temperature measurements recorded during the tests is shown in *Figure 2.5*. It shows the temperature ramping up in the heating phase (0 to 2400 sec) and then slowly cooling down (2400 to 11000 sec). The temperature profile of the four points was found to be same for both substrate combinations (DP980 - AA7071 and AA7071 - AA7071). The temperature profile of the top and bottom substrates is nearly the same but it is different from the temperature profile of the top and bottom grip. The top grip heats at a faster rate than the bottom grip and cools at a much slower rate. This is due to the fact that the hot air inside the furnace rises up and heats the upper half of the furnace more rapidly than the lower half.

### **2.2.4.2. DIC results (Displacements)**

The image series recorded for the entire paint baking cycle was processed and the X/Y/Z displacement contour map for the target region was obtained. The relative Y-displacement in the two substrates during the curing process at different times is shown in *Figure 2.6*. A virtual extensometer of 30 mm (*Figure 2.7*) was created across the joint

with the end-point on each substrate. The relative Y-displacement across the joint for three repetitions for DP980 - AA7071 and AA7071 - AA7071 tests is shown in *Figure 2.8*. The legend in the plot also shows the thickness of the adhesive bead, measured after the test.

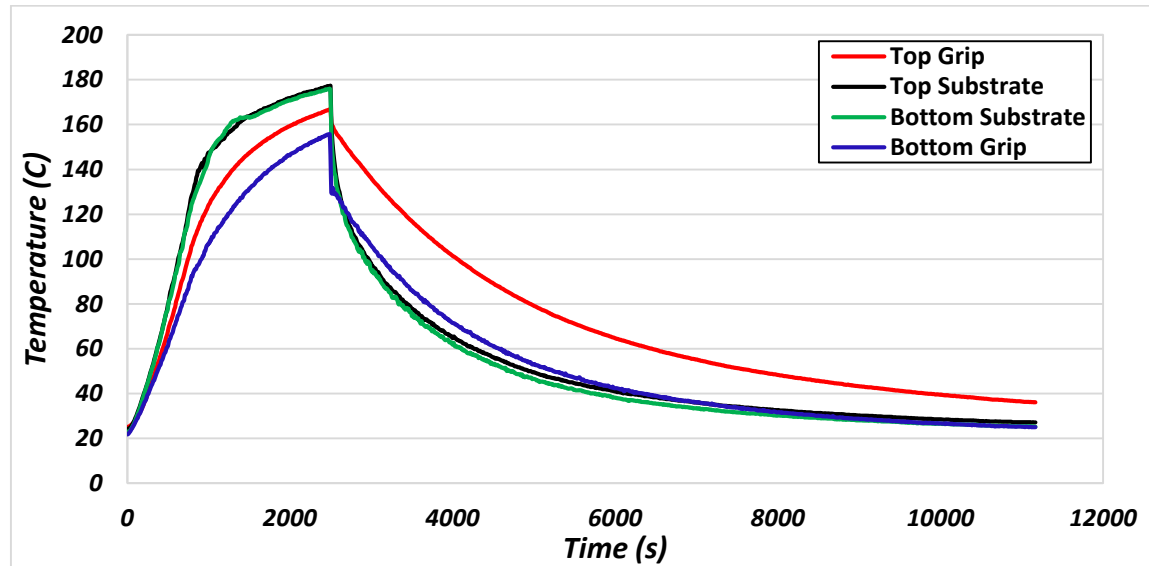


*Figure 2.5 Surface temperature profiles obtained from the four thermocouples*

#### 2.2.4.3. Force results

The force measurements recorded by the load cell attached to the top grip rod are shown in *Figure 2.9*.

#### **2.2.4.4. Discussion**

The trends in the temperature profile, Y-displacement and force measurements, when studied together, explain the effect of the heat curing process and the behavior of the adhesive joint during the curing process.

During the heating phase, as the temperature of the two metallic substrates and the grip rods starts rising, they begin to expand. The top substrate, being constrained to the grip rods at its top end, tends to move down in the negative Y direction. Similarly, the bottom substrate moves upwards, in the positive Y direction. This is represented by a negative relative Y-displacement in the heating phase (*Figure 2.8*). On the other hand, the uncured adhesive is compliant in the beginning and does not pose any restriction to the movement of the substrates, thereby giving a negligible force in the beginning (*Figure 2.9*). With increasing temperature and time, the adhesive starts curing at around 1800 seconds and the adhesive modulus starts rising. Due to this, the adhesive starts restricting the further expansion of the substrates and the load cell picks up compressive forces. The temperature of the system keeps rising till the end of the heating phase, generating further expansion in the substrates and the grips. Therefore, the Y-displacement keeps rising in the negative direction and the compressive force keeps mounting on the adhesive.

At the onset of the cooling phase, the temperature of the system starts dropping. Due to this, the substrates and the grips begin to contract and the direction of the displacement is reversed. The substrates start moving away from each other, back to their original state.

The fully cured adhesive bond now starts opposing the thermal contraction and the load cell starts picking tensile forces. As a result of the bond, the substrates fail to retract to their initial state and this is shown by a residual Y-displacement at the end of the cooling phase.

It was observed that the level of negative forces at the end of heating phase was significantly lower than the positive forces at the end of the cooling phase. This behavior is well explained by the temperature and cure dependent properties of the adhesive. At the peak temperature, although the adhesive gets fully cured, the effect of the high temperature keeps the adhesive modulus low and the adhesive stays more compliant. At lower temperatures, the modulus of the fully cured adhesive rises sharply and the tensile force applied by the adhesive reach much higher levels. These tensile forces applied by the adhesive set the residual stress in the adhesive bond.

***Effect of substrate combination:*** The Y-displacement on 30mm GL for AA7071 - AA7071 combination show a higher negative peak as compared to DP980 - AA7071 combination, at the end of heating phase owing to a higher coefficient of thermal expansion for aluminum. A higher level of thermal expansion and contraction in the aluminum substrate leads to a higher displacement across the joint and produces a higher force at the end of the cooling phase.

**Effect of adhesive bondline thickness:** The behavior of the joint was very sensitive to the thickness of the adhesive bead. Due to manual application of adhesive in specimen preparation, it was a challenge to ensure same thickness for each specimen. Therefore, the thickness of each specimen was recorded after the test. It was found that the thickness of the aluminum bead of each sample had a relation with the final force value at the end of cooling phase. The force for a thinner adhesive bead specimen was higher than the thicker bead specimen. A thin adhesive bead leads to a stiffer joint which produces a higher force at the end of the cooling phase.

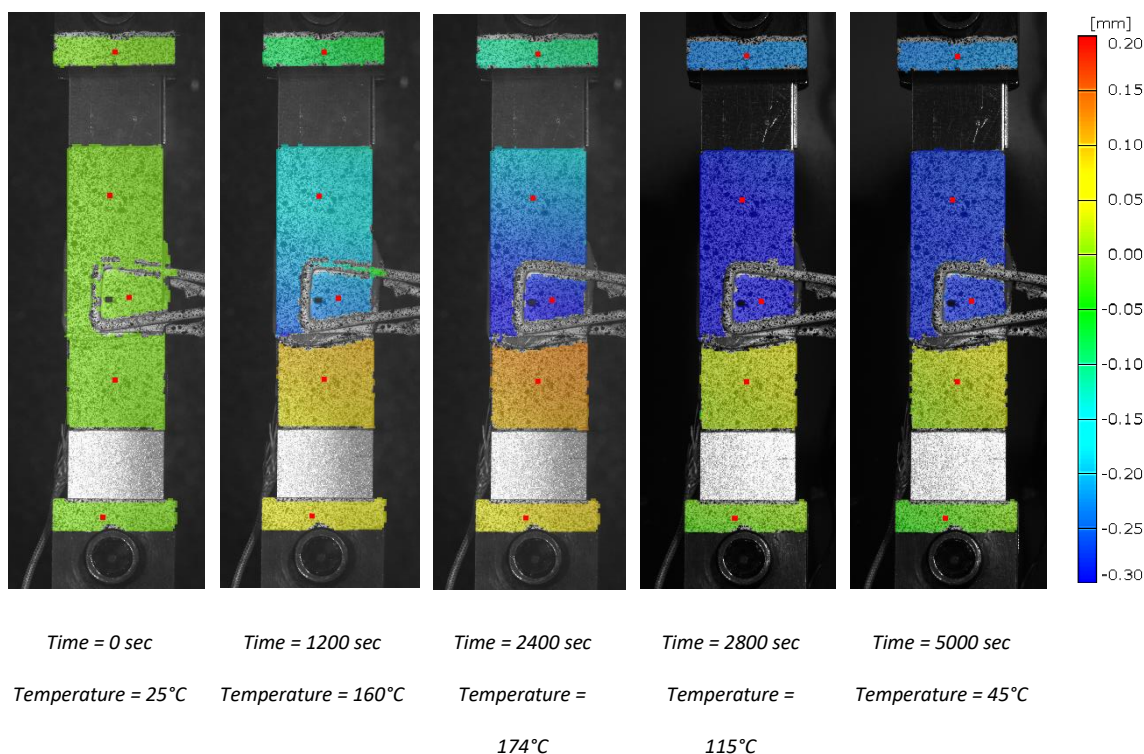


Figure 2.6 Y-displacement contour map obtained from processing DIC results

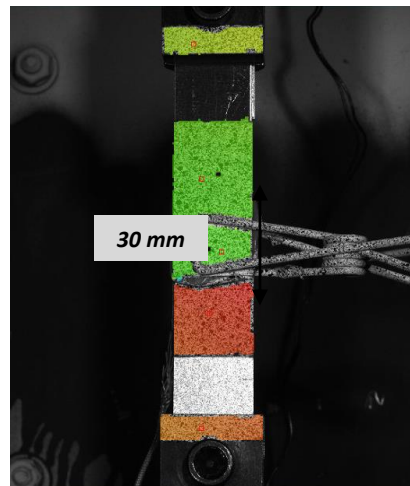


Figure 2.7 Virtual extensometer of 30 mm length across the adhesive joint

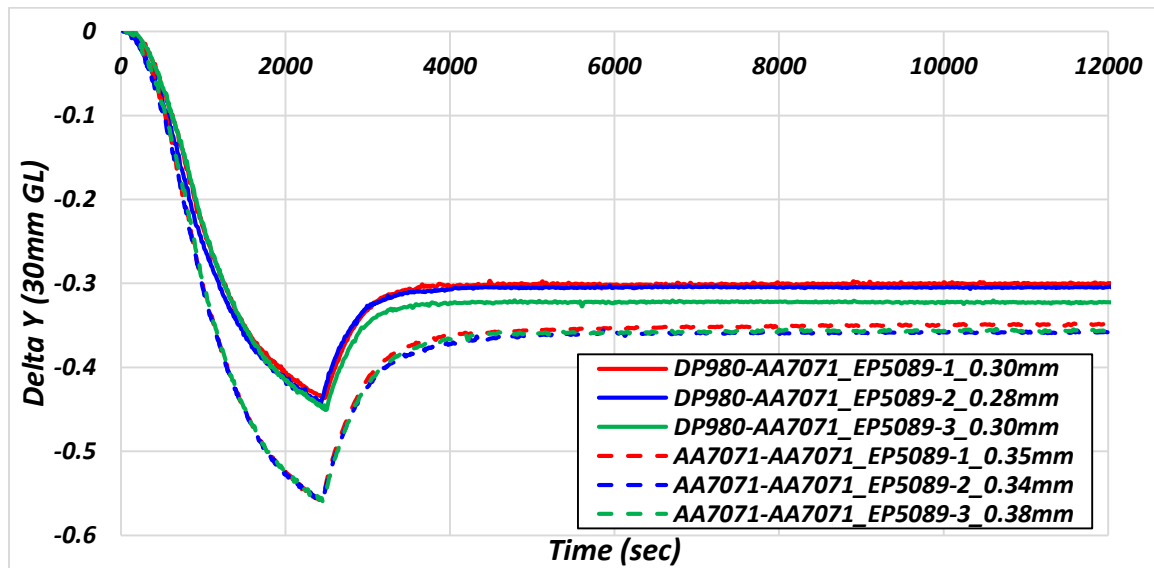


Figure 2.8 Y-displacement on 30 mm gauge length across the joint for DP980 - AA7071 and AA7071 - AA7071 tests

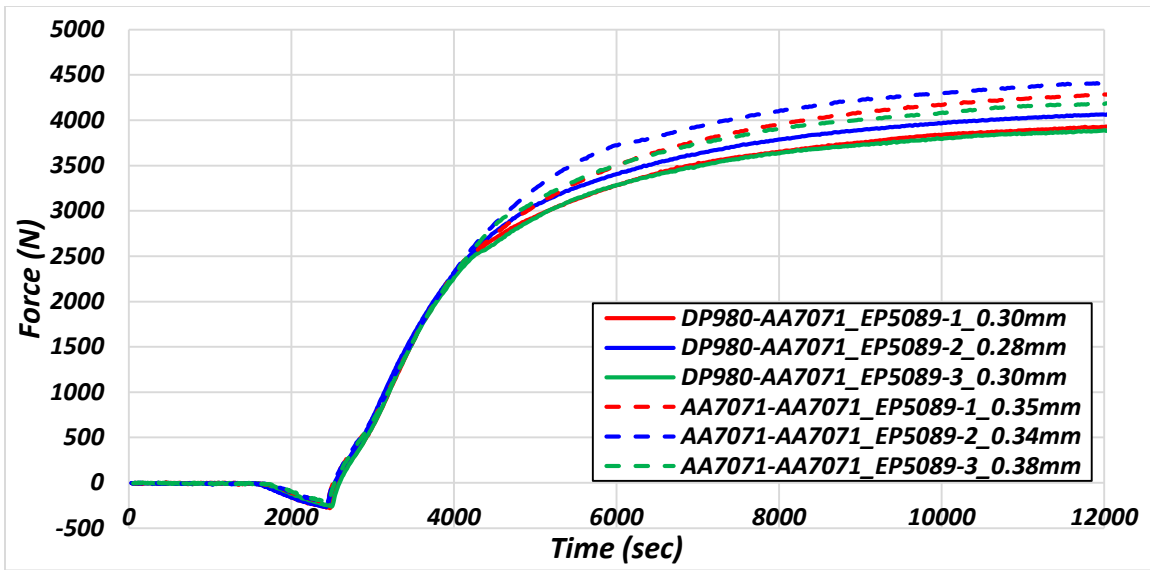


Figure 2.9 Force measurements during the curing cycle for DP980 - AA7071 and AA7071 - AA7071 tests

Based on the results of this test, it is safe to say that the manufacturing process of a heat cured adhesive joint puts residual stresses on the adhesive bond and causes distortion in the substrates. The effects of thermal expansion during the curing process will be much more magnified on a full vehicle level. Therefore, it is important to understand the significance of these process induced residual stresses on the performance of the joint, which is discussed in the next section.

## 2.3 Experiments to evaluate the effects of residual stress on joint performance

In the last set of experiments, it was established that thermal expansion in the metallic substrates induces residual stress in the adhesive bonded joint during the heat curing

process. In this section, the single lap shear joints with residual stresses were pulled in tension and the results were compared to the performance of the joints without residual stresses. The joints were tested at multiple shear strain rates, ranging from very slow rate 0.005/s to high rate 50/s. The test results provide insight about the effects of residual stress at high rates which will help in predicting the joint behavior at the time of events like crash.

### **2.3.1 Specimen geometry and materials**

The tests were run on a single lap shear specimen geometry discussed in the previous section 2.1. The tests were performed on the same adhesive Henkel EP 5089 and on a multi-material substrate combination of DP980 - AA7071.

Two types of samples were prepared for the tests- Type I: stress free samples, and Type II: with residual stress.

The stress free samples (type I) were prepared by curing the specimens without constraining the substrates, to allow free movement due to thermal expansion. The specimens were cured for 30 minutes at 180°C. *Figure 2.10* shows the method for specimen preparation.



*Figure 2.10 Stress free (Type I) adhesive bonded single lap shear specimen preparation*

The type II specimens were prepared on the same setup and following the same procedure as discussed in the previous sections 2.2 and 2.3.

### **2.3.2 Experimental Setup**

The tests were performed on two different experimental setups for the different shear strain rates.

The tests at 0.005/s and 0.5/s were done on an Instron quasi-static electromechanical load frame with a 250kN load cell. The single lap shear joint specimen was held using wedge grips and the strain measurement was done using Gom Aramis 3D DIC system which is capable of capturing images at up to 125 frames per second. *Figure 2.11* shows the experimental setup and the specimen mounted on the wedge grips.

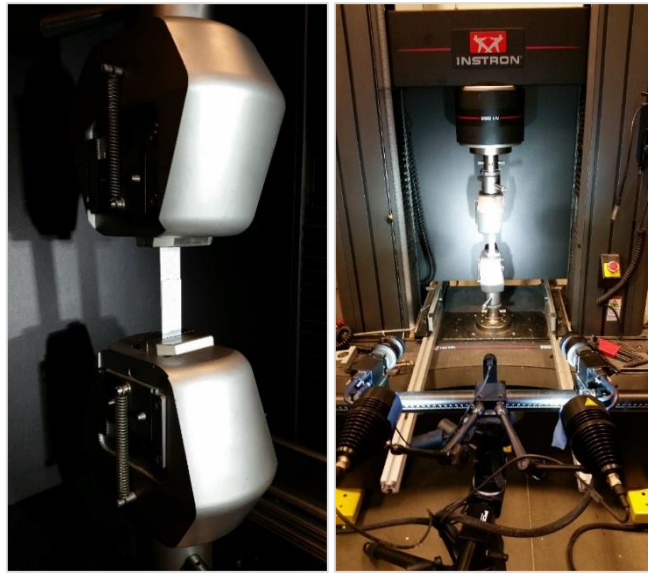


*Figure 2.11 Experimental setup for testing at 0.005/s and 0.5/s shear strain rates*

The tests at a shear strain rate of 50/s were performed on an Instron servo-hydraulic machine which was capable of going at higher speeds. The setup had a pair of hydraulic wedge grips and the strain measurement was done using Photron AX200 high speed camera at 100,000 frames per second. The experimental setup for high speed testing is shown in *Figure 2.12*.



*Figure 2.12 Experimental setup for testing at 50/s fastest shear strain rate*

### 2.3.3 Results

The DIC results were processed to obtain the displacement across the joint. A virtual extensometer of 30 mm was drawn with one end on each substrate, with an aim to keep to adhesive joint within the extensometer length. The change in the Y-length of the extensometer was divided by the pre-measured bond thickness to determine the value of the shear strain.

$$\text{Shear Strain} = \Delta Y / (\text{Bond thickness})$$

The force vs. shear strain curves for the tensile tests of lap shear adhesive joints for the three shear strain rates are given in *Figure 2.13*, *Figure 2.14* and *Figure 2.15*.

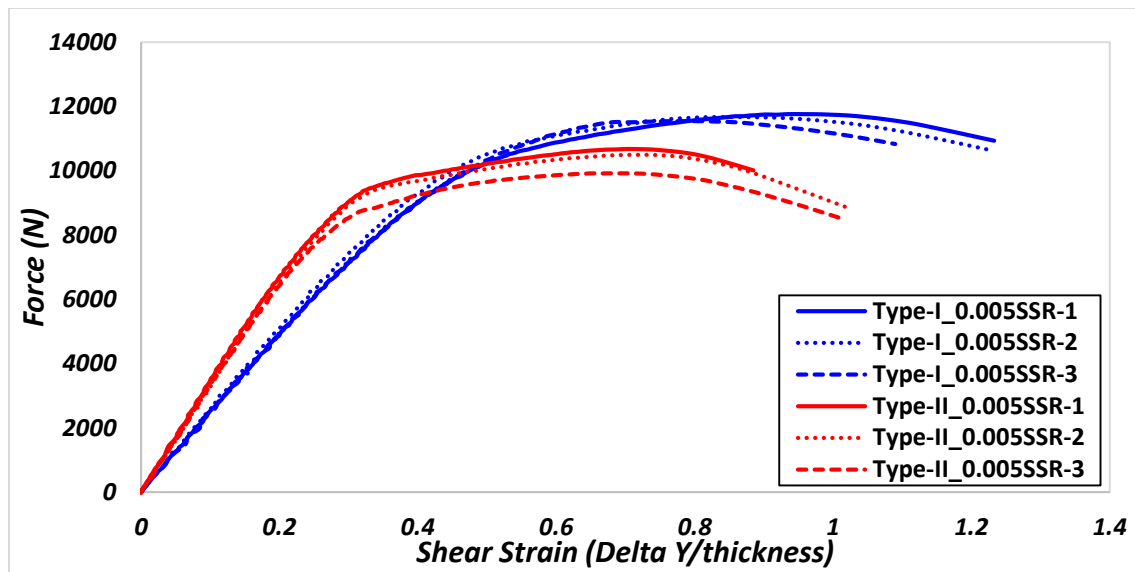


Figure 2.13 Force-Strain curves for DP980-AA7071 lap shear specimens at shear strain rate of 0.005/s for stress free (type I) in blue and with residual stress (type II) in red

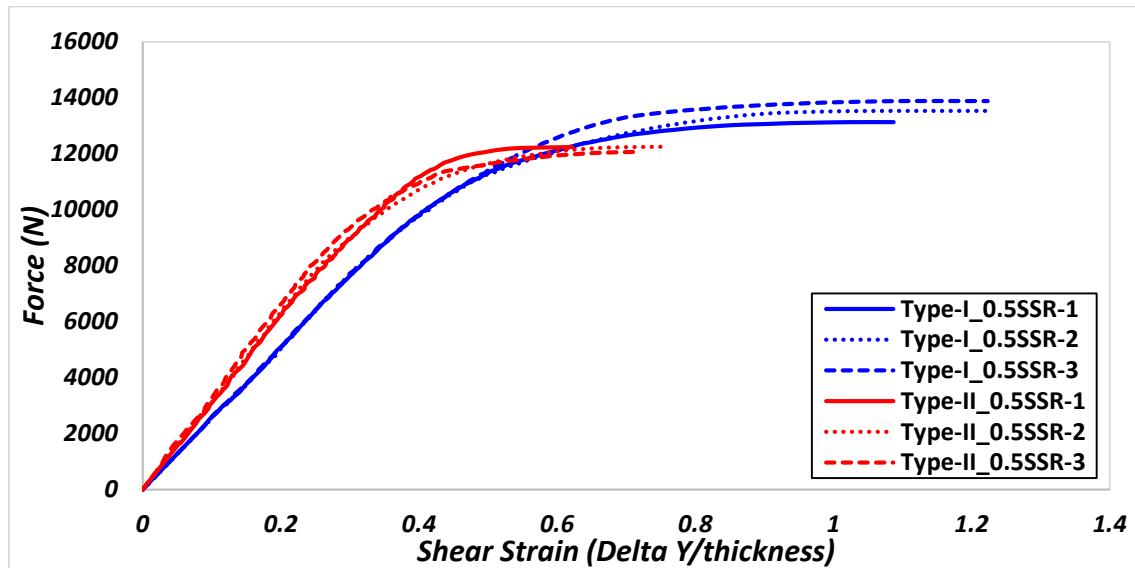


Figure 2.14 . Force-Strain curves for DP980-AA7071 lap shear specimens at shear strain rate of 0.5/s for stress free (type I) in blue and with residual stress (type II) in red

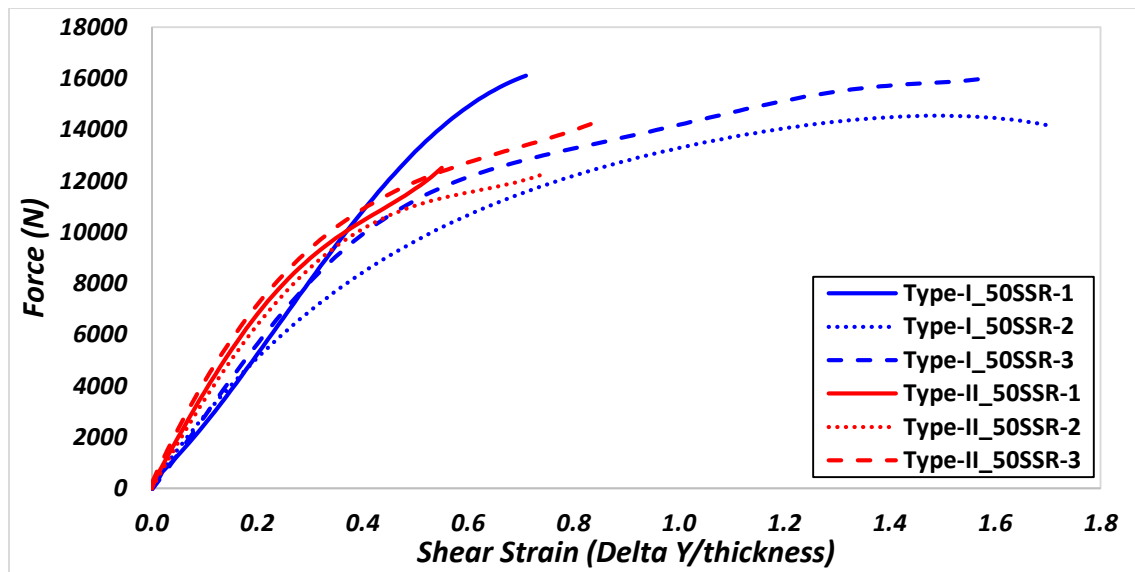


Figure 2.15 Force-Strain curves for DP980-AA7071 lap shear specimens at shear strain rate of 50/s for stress free (type I) in blue and with residual stress (type II) in red

### 2.3.4 Discussion

The force vs. shear strain curves for tension tests of lap shear joints at all three strain rates show linear nature in the beginning followed by some plasticity. There are some important conclusions derived from the tests:

- (i) An important difference between the curves for type II and type I is the initial slope of the curve. The stiffness of the specimens with residual stress is higher than the stress free specimens for all the strain rates.
- (ii) Another noticeable effect of residual stresses is the difference in maximum force to failure. The maximum force for the stressed specimen is lower than the stress free specimens for all the shear strain rates.

- (iii) There is a drop in maximum shear strain to failure when the specimens have residual stress as compared to stress free specimens.
- (iv) The results from the tension tests of single lap shear joints show large strain rate sensitivity. The maximum force to failure increases by 36% for the shear strain rate jump from 0.005/s to 50/s for stress free specimens. Similar increase in maximum force was observed for specimens with residual stress. A comparison of the curves for different strain rates for stress free (type I) and with residual stress (type II) specimens is shown in *Figure 2.15*.

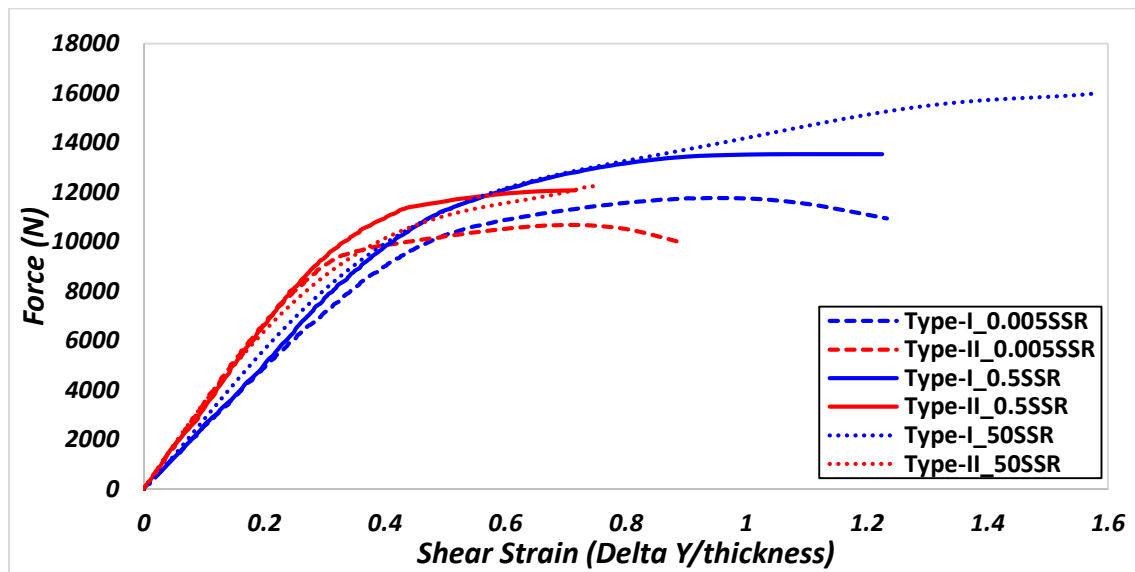


*Figure 2.16 Comparison of force-strain curves for DP980-AA7071 lap shear specimens at shear strain rates of 0.005/s, 0.5/s and 50/s for stress free (type I) in blue and with residual stress (type II) in red*

## **2.4 Component level experiments to capture curing induced effects**

The next set of experiments were carried out on scaled-down automotive roof component. A scaled-down roof model with aluminum roof panel and steel roof bows was cured inside a specially prepared heating chamber with glass door to facilitate optical strain measurements using DIC. The tests were conducted in two scenarios: (i) With adhesive only, (ii) with adhesive and mechanical fixations. The displacements in the roof panel and roof bows due to the thermal expansion and contraction were recorded by DIC to capture the distortion in the structure during the heating and cooling phase of the automotive paint baking cycle.

### **2.4.1 Experimental setup**

The experimental setup used for the component level validation consisted of a heating chamber with a wide glass window opening on one door. The glass window allowed a large field of view for the DIC cameras. The test started with the chamber door closed and after the end of the heating cycle, the door was opened to allow natural cooling during the cooling down phase of the temperature cycle. The test setup is shown in *Figure 2.17*. There were four thermocouples attached at four different locations on the aluminum panel and steel roof bows.

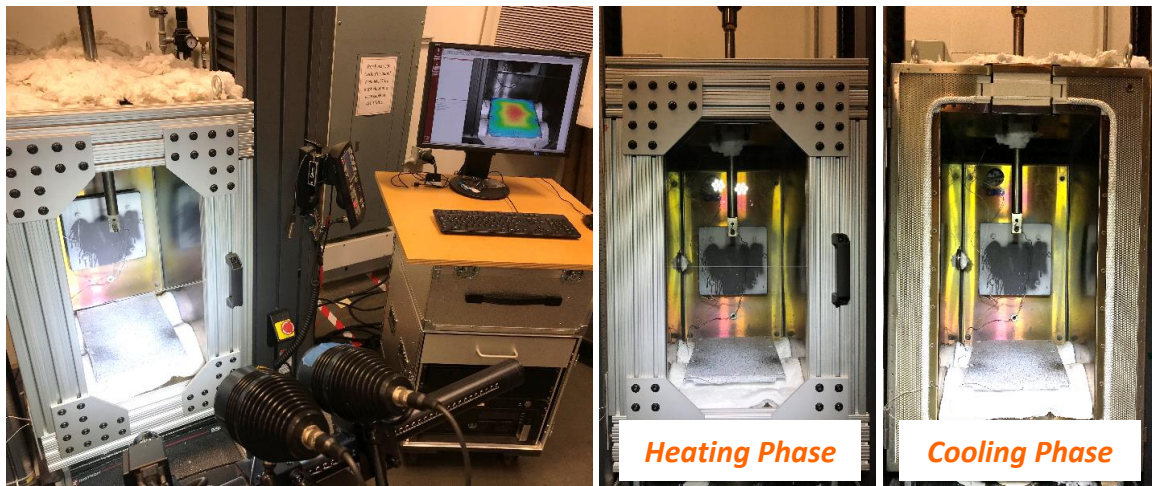


*Figure 2.17 Experimental setup for component level validation on a scaled-down roof model*

## 2.4.2 Specimen Details

The roof component design was based on BMW X3 roof component aspect ratio. The scaled-down component was 1/36<sup>th</sup> scaled down model of BMW X3 roof (1900 mm x 1100 mm) by area. The roof component consisted of steel roof rails made of U-channel (3 mm thick) welded together to form a rigid frame. The component was 320 mm x 220 mm in size which had a flat aluminum panel (1.1 mm thick) of 300 mm x 200 mm bonded to it. An adhesive layer of 0.2 mm with a bondline width of 10 mm was applied on the steel frame. *Figure 2.18* shows the welded steel frame, adhesive applied on the target area and aluminum flat panel positioned on top of the steel frame and adhesive.

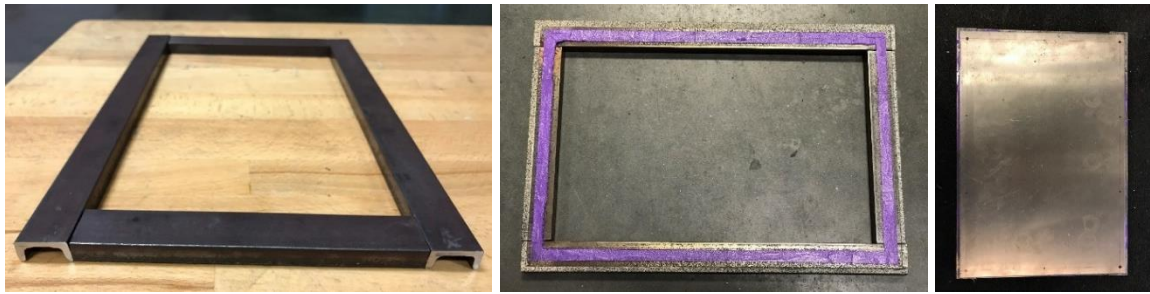


Figure 2.18 Steel frame, adhesive applied on the frame and aluminum flat panel mounted on the frame

The tests were conducted in two scenarios:

- *Scenario 1:* With adhesive only
- *Scenario 2:* With adhesive and mechanical fixations

**Scenario 1:** With adhesive only: The flat aluminum panel was stuck on the steel frame with adhesive only. In this case, the top left corner of the component was clamped with a heavy duty C-Clamp to lock the movement in X, Y and Z directions. The other three corners were held together by spring clamps to lock only the movement in Z-direction and to ensure proper bonding to the adhesive. The specimen for scenario 1 is shown in

Figure 2.19.



*Figure 2.19 Specimen with adhesive only, hard clamped at the top left corner*

**Scenario 2:** With adhesive and mechanical fixation: In this case, the flat aluminum panel was stuck on the steel frame with adhesive and held together by Friction Element Welds (Ejoweld) at a gap of 100 mm. Friction element welds are a technology developed by EJOT corporation. Friction element weld is an innovative option to join different materials and semi-finished parts. It offers the possibility to join multi-material-designs, especially lightweight materials such as aluminum and advanced high-strength steel, with a friction element setting tool suitable for robots. EJOWELD® friction welding is used to join overlapping work pieces without pre-hole. A requirement for this method is the accessibility of the joining point on both sides. This was one of the reasons for choosing a steel U-slot for building the frame of the roof component.

The process of joining is shown in *Figure 2.20*. The steel friction element penetrates the upper layer (e.g. aluminum) and welds onto the base plate, which is made of high-

strength and advanced high-strength steel. The friction, which is generated by appropriate process control and the application of mechanical forces, acts directly on the friction element. The produced frictional heat acts on the element and the base plate without reaching the melting temperature. An adhesive bond is only created between the friction element and the base plate. Between the friction element and the upper layer just force and form closure is achieved. When the head of the element has reached the upper plate, the rotation stops and an increased axial force is applied to the friction element. Hence, the upper layer gets fixed between the head of the friction element and the base plate. The friction element thus fulfills two separate tasks during the joining process. On the one hand, it penetrates the cover sheet without altering its properties, and on the other hand it reliably generates the frictional heat to create the steel-steel bonding.

Having friction element welds ensured that the panel was locked in X, Y and Z directions, and the expansion was limited at the weld locations. This scenario was closer to an actual roof construction in body-in-white. The specimens for scenario 2 with adhesive and mechanical fixation is shown in *Figure 2.21*.

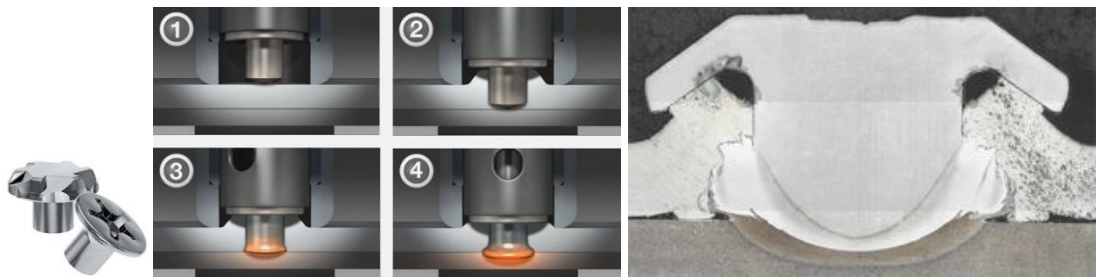


Figure 2.20 Joining process of friction element welds (Ejoweld) [Source: EJOT]

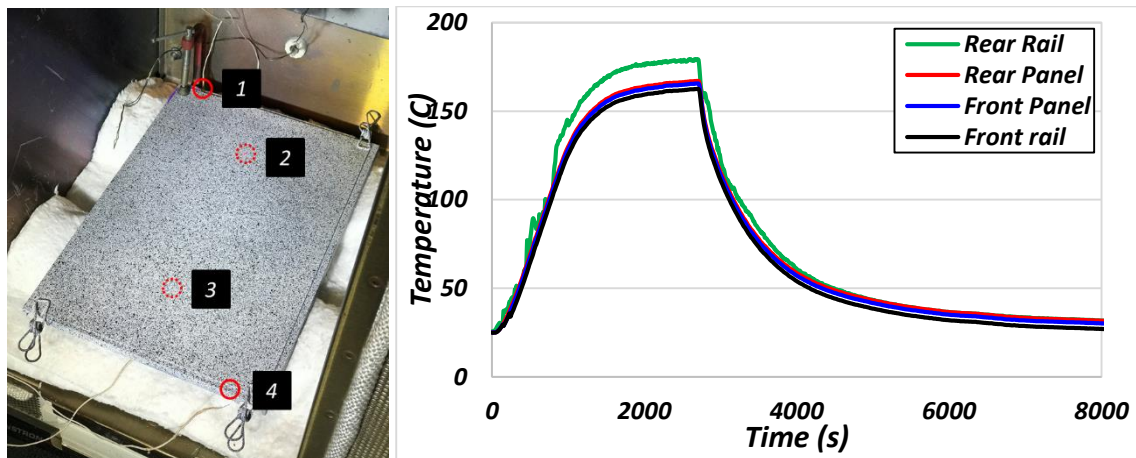


Figure 2.21 Specimen with adhesive and friction element welds

### 2.4.3 Test Process

After the specimens were prepared, the test specimen with uncured adhesive between the aluminum flat panel and steel frame was painted in speckle pattern, required for DIC system. The four thermocouples were attached to the component before placing it in the heating chamber. Two thermocouples were attached to the back of the aluminum panel and two were attached to the steel frame at locations shown in *Figure 2.22*. The chamber was heated to 180°C for a period of 45 minutes and then was let to cool down naturally.

The deformations in the panel were recorded by DIC cameras during the whole thermal cycle. A sample temperature profile recorded during the test for the four thermocouples is shown in *Figure 2.22*. The temperature at the rear rail, captured by thermocouple 1 was higher than the rest of the locations because of its proximity to the fan and heating elements of the heating chamber. The temperature profiles recorded from the experiments were later fed into the FE simulations. The test was stopped when the temperature dropped below 30°C.



*Figure 2.22 Thermocouple locations and temperature profile recorded on rear rail (1), rear panel (2), front panel (3) and front rail (4)*

The detailed results from the tests are shared in chapter 5 in the section for component level validation and compared to the finite element model results.

## 2.5. Conclusion

In this chapter, two sets of experiments were discussed. The first set of experiments is an innovative approach to study the effects of thermal expansion on the adhesive joint

during the heat curing process. The experimental results shed some light on the behavior of the adhesive bonded joint for a multi-material substrate combination and a similar material substrate combination. It established that the adhesive bonded joint is subjected to residual stress at the end of curing process due to thermal expansion in the substrates. The second set of experiments presented the effect of residual stresses on the performance of a single lap shear joint. The performance of the joint with residual stresses was compared to stress free joints at varying strain rates. The results showed that the residual stresses hinder the peak performance of the joint by limiting the maximum force to failure and the total strain to failure. On the basis of the derived results, it is necessary to include the effects of manufacturing induced effects in the design process of adhesive bonded structures.

# **Chapter 3**

## **3. MATERIAL MODELING**

The thermal loading during the manufacturing process of an adhesive bonded multi-material joint affects the performance of the adhesive bond, which is previously established experimentally in chapter 2. A novel approach was developed to model the properties of automotive adhesives during the heat curing process. The material model was calibrated using Differential Scanning Calorimetry (DSC) and Dynamic Mechanical Analysis (DMA) results on the epoxy based single-component adhesive.

### **3.1 Introduction**

In the previous chapter, it was experimentally shown that the process induced residual stresses affect the performance of the adhesive bonded joints. It is therefore crucial to understand and consider the influences of heat-curing process induced stresses in the design of the adhesive joint and the body structure. Due to the absence of any direct and reliable experimental technique to measure the residual stresses in the adhesive bond

(Marques, da Silva et al. 2014), one of the main challenges here is the assessment of the nature and magnitude of residual stresses developing in the adhesive-bonded joint during the manufacturing process. Therefore, the use of adhesive-joined multi-material structures in the body of an automobile is hindered by the lack of information on the value and extent of residual stress developed in the bond.

Several attempts have been made in the past to model the residual stresses in epoxy resins in carbon fiber composite structures to study the delamination behavior. Some works use an elastic constitutive model for the purpose (Travis A. Bogetti 1992, Xiaogang Huang 2000, Brauner, Bauer et al. 2014), while some complex formulations use viscoelastic models (Kim 1996, M. Kaliske 1997, Ruiz 2004, Saseendran 2016, Courtois, Hirsekorn et al. 2018). Notable work has been done by Adolf and Martin (Douglas Adolf 1996) to calculate the stresses in crosslinking polymers depending on curing behavior. The basic idea in their work was to estimate the cure level and linking it to the mechanical properties of the polymer. It was also established later that automotive adhesives exhibit a small plastic behavior in addition to viscoelastic behavior which makes it difficult to directly adopt the existing models for automotive adhesives (da Silva, das Neves et al. 2009).

The literature suggests that the adhesives show some plastic behavior after getting fully cured (Budhe, Banea et al. 2017). Just like metals, the adhesives show rate dependent and temperature dependent plastic properties (Hu, Han et al. 2013, May, Voß et al. 2014).

The strength of the adhesive drops with increasing temperature. The effect of the plastic model is of significance during the cooling down phase of the adhesive bond in a paint baking cycle. At the start of the cooling phase, when the adhesive is fully cured, it begins to show viscoelastic-plastic behavior. At this stage, the viscoelastic modulus and the yield strength of the adhesive is low due to the high temperature. As the temperature decreases with time, the viscoelastic modulus and the yield strength increase together. At any stage, if the effective stress in the adhesive bond becomes higher than the yield strength of the adhesive, the adhesive accumulates plastic strains. In light of this, it is necessary to model the plastic component of the adhesive to accurately model the curing induced effects on the adhesive bond.

This work builds on the idea of using two distinct models for automotive adhesives, first for determining curing level and second for predicting the mechanical behavior based on the calculated cure level. This chapter presents a cure dependent viscoelastic-plastic approach. The plastic properties were determined by performing tensile tests on fully cured adhesive at different temperatures and strain rates. The stress-strain curves were fit to a phenomenological constitutive model. The goal of this work is to develop an efficient and easy to implement approach for characterization and modeling of adhesives during curing in order to predict manufacturing induced effects on the adhesive joint. The proposed material model will enable determination of the geometrical distortions in an automotive body structure generating due to adhesive heat curing process and provide an estimation of the residual stresses developed in the adhesive bond. The prediction

results for manufacturing process induced stresses from this model can be used as a starting point for further component level and full-vehicle level crash simulations. The application of the proposed adhesive curing model can also be extended to the innovative single-shot manufacturing process that has been recently developed to manufacture composite-metal hybrid components in one operation(S. Farahani 2018, H. Kazan 2019). The developed model in this work can be used to predict the final geometry of the hybrid part by calculating the distortion induced by this manufacturing process. Moreover, the calibrated material model can be fed into the numerical simulation of this hybrid process to determine the residual stress within the interfacial layer thus predicting the chance of delamination (Farahani, Yelne et al. 2019).

This chapter starts with a short discussion on the theory behind the proposed material models, followed by the experiments performed for model calibration and the detailed mathematical approach to calibrate the material models.

## **3.2 Material Modeling**

When a body-in-white passes through a paint baking oven, different components of the structure are heated at different rates and extents depending on their thermal material properties, local air convection characteristics, design intricacy and location of the component giving rise to very different temperature-time histories across the component, which directly affects the uniformity of adhesive curing (R.A. Dickie\* 1997, Zhang, Xu et al. 2009). Since the mechanical properties of an adhesive bond are highly

dependent on the quality of curing, it is crucial to accurately determine the degree of cure in order to accurately model the mechanical behavior of the adhesive during curing and post-curing. Then, we need a mechanical model which can predict the mechanical properties of the adhesive depending on the degree of cure and temperature.

Adhesives are known to show viscoelastic behavior while they are being cured, and viscoelastic-plastic behavior after getting fully cured. In this study, it is assumed that the displacements due to CTE mismatch effects are small, due to which the adhesive sees only viscoelastic deformation. Therefore, the scope of this study is limited to viscoelastic regime for simplicity. It is well established that heat cured adhesives exhibit chemical shrinkage on curing. It is also shown in several studies that the stresses generated due to chemical shrinkage are relatively small and their relevance for automotive applications are insignificant as compared to other phenomenon, like CTE mismatch of substrates (Marques, da Silva et al. 2014). The measurement of shrinkage properties entails several tests on the Thermo-mechanical analyzer (TMA) (Daoqiang Lu 2000), which has been skipped from the scope of this study in order to reduce model complexity.

Hence, this work is divided into two models, (i) Curing Kinetics model and (ii) Viscoelastic mechanical model

### **3.2.1 Curing Kinetics Model**

The process of conversion of an adhesive from viscoelastic liquid state to a viscoelastic-plastic state in the presence of a catalyst is called as curing of adhesive. As discussed

earlier, the automotive grade structural adhesives are heat cured adhesives, which need to be exposed to elevated temperatures for curing. When a thermosetting epoxy is heated, it undergoes a chemical reaction and gets cured to form a three-dimensional cross-linked network which is irreversibly locked in place and can't be reformed or reprocessed. The degree of cure/conversion (represented as  $\alpha$ ) of an adhesive is a function of the temperature-time history that the adhesive is exposed to and is represented as a number ranging from 0 to 1. The rate of conversion w.r.t time can be mathematically described as:

$$\frac{d\alpha}{dt} = f(\alpha) \cdot K(T) \quad (1)$$

where,  $f(\alpha)$  is a phenomenological reaction model, while  $K(T)$  is the temperature dependent function defined by an Arrhenius relationship, which is:

$$K(T) = A \exp(-E_a/RT) \quad (2)$$

where,  $A$  is the pre-exponential constant,  $E_a$  is the activation energy,  $R$  is the universal gas constant and  $T$  is the temperature. The formulation discussed in this approach is applicable to epoxy based adhesives which have autocatalytic nature, i.e. the reaction progresses automatically after the initiation. A brief compilation of the curing kinetics models is shown in *Table 3.1*.

<b>Reference</b>	<b>Yr</b>	<b>Material</b>	<b>Time function</b>	<b>Activation Energy Method</b>	<b>Cure function</b>	<b>Equation</b>
Musa R. Kamal	1974	Epoxy Resin	-	-	4 parameter based equation	$\frac{d\alpha}{dt} = (k_1 + k_2 \alpha^m)(1-\alpha)^n$
M.E.Ryan et al.	1979	DGEBA	-	-	Kamal Model (1974)	"
R.A. Dickie et al.	1997	2-C Urethane enamel	Arrhenius Eqn.	Curve fitting	First order eqn.	$\frac{d\alpha}{dt} = k(1-\alpha)$
Mauro Zarrelli et al.	2002	Epoxy Resin	Modified Arrhenius	Non-linear least squares fitting	Combined autocatalytic and diffusion control model	$\frac{d\alpha}{dt} = k_1 (1-\alpha)^{n1} + k_2 (1-\alpha)^{n2} \alpha^m$
D. Rosu et al.	2002	DGEBA, DGEHQ	Arrhenius Eqn.	Isoconversional method (Málek)	2 parameter autocatalytic model (Sestak-Berggren eqn.)	$\frac{d\alpha}{dt} = \alpha^m (1-\alpha)^n$
Xiao-Wang Yang et al.	2008	DGEBA	"	Friedman Isoconv. method	"	"
Cai, Hongyang et al.	2008	DGEBA	"	Isoconv. Method by Vyazovkin	Kamal Model (1974)	$\frac{d\alpha}{dt} = (k_1 + k_2 \alpha^m)(1-\alpha)^n$
Liu, Wenbin et al.	2008	DGEBF, TDE-85, DGEBA	"	(i)Kissinger, (ii)Ozawa (iii)Crane	-	-
Badrinarayanan et al.	2009	Soybean oil-styrene-DVB	"	(i)Kissinger's Eqn. (ii)Isoconversion method	<i>n</i> th order, <i>n</i> th order autoctalytic, Prout-Tompkins autocat.	$\frac{d\alpha}{dt} = (1-\alpha)^n$ $(1-\alpha)^n (1+k\alpha)$ $\frac{d\alpha}{dt} = \alpha^m (1-\alpha)^n$

Li, Gang et al.	2010	TGDDM/DD S	"	Isoconv. Method by Vyazovkin	Kamal Model (1974)	$\frac{d\alpha}{dt} = (k_1 + k_2 \alpha^m)(1-\alpha)^n$
Wang, Haimei et al.	2011	DGEBA	"	Kissinger- Akahira- Sunose (KAS)	Kamal Model (1974)	"
Hardis, Ricky et al.	2013	DGEBA	"	(i) Kissinger's Eqn. (ii) Ozawa- Flynn-Wall - $\alpha$	<i>n</i> th order, <i>n</i> th order autoxalytic, Prout- Tompkins autocat.	$\frac{d\alpha}{dt} = (1-\alpha)^n$ $(1-\alpha)^n(1+k\alpha)$ $\frac{d\alpha}{dt} = \alpha^m(1-\alpha)^n$
Welters, Tim et al.	2013	Automotive grade Adhesive	"	Isoconversional methods (i) Friedman (ii) Vyazovkin	Kamal Model (1974) with diffusion term	$\frac{d\alpha}{dt} = (k_1 + k_2 \alpha^m)(1-\alpha)^n * \frac{2}{1+e^{D(T)(\alpha-\alpha_c)}}$
Duemichen, E. et al.	2015	DGEBA	"	(i) Friedman isoconversion (ii) Ozawa- Flynn-Wall - $\alpha$	<i>n</i> th order autocatalytic	$\frac{d\alpha}{dt} = (1-\alpha)^n(1+k\alpha)$
Javdanitehran et al.	2016	DGEBA	"	Iterative scheme	Kamal Model (1974)	$\frac{d\alpha}{dt} = (k_1 + k_2 \alpha^m)(1-\alpha)^n$
Hu, Jianhua et al.	2016	Glycidyl ether of cresol formaldehyde novolac, DGEBA	"	Curve fitting	Kamal Model (1974) with diffusion term	$\frac{d\alpha}{dt} = (k_1 + k_2 \alpha^m)(1-\alpha)^n$ $f(\alpha)$
Erdmann, Maren et al.	2017	DGEBA Mix of DGEBA and DGEBF	"	Ozawa-Flynn- Wall - $\alpha$	<i>n</i> th order autocatalytic	$\frac{d\alpha}{dt} = (1-\alpha)^n(1+k\alpha)$

Table 3.1 Literature survey on curing kinetics models

Several reaction models are published in the literature which can satisfactorily predict the reaction rate of polymers. After an extensive literature survey, the reaction model chosen

for this work was Kamal's Model (Kamal 1974) which has been validated in several studies based on epoxy resins (Mauro Zarrelli\* 2002, Cai, Li et al. 2008, Liu, Qiu et al. 2008, Li, Huang et al. 2010, Wang, Zhang et al. 2011, Hu, Shan et al. 2016, Javdanitehran, Berg et al. 2016). The said model can be shown as:

$$f(\alpha) = (k_1 + k_2 \alpha^m)(1 - \alpha)^n \quad (3)$$

where,  $k_1$  is the zero conversion rate value,  $k_2$  is the auto-catalytic rate constant, m is the auto-catalytic exponent and n is the order of the reaction model.

### **3.2.2 Viscoelastic Model**

Adhesives are known to show time and temperature dependent viscoelastic behavior. The viscoelastic behavior of epoxies and other polymers published in the past. Table 3.2 shows a list of the models available in the literature.

Reference	Year	Model	Material	Cure-dependent	Remarks
Humfeld	1998	Maxwell model	Unknown adhesive	-	Residual stress due to thermal cycling
Park, Schapery	1999	Generalized Maxwell model	PMMA	-	Thermodynamics based model
Prasatya	2001	Generalized Maxwell model	Toughened epoxy resin	X	Neglects shear stresses

Ernst	2002	Generalized Maxwell model	Epoxy	X	Only thermal formulation	strain
Meuwissen	2006	Generalized Maxwell model	DGEBA-aliphatic poly-amine curing agent	X	Neglects validation	plasticity, no
Hossain	2009	Elastic	-	X	Elastic only, no validation	
Drabousky	2009	Generalized Maxwell model	Equine cortical bone	-		
Msallem	2010	Polynomial fitting	Epoxy resin	X	Epoxy matrix composites, neglects plasticity	
Babaei	2015	Generalized Maxwell model	Collagen gel (Biological tissue)	-	-	
Dufour	2016	Maxwell model with plasticity formulation	Epoxy adhesive Sikapower498	-	Includes formulation for dynamic loading with plasticity	
Dong	2017	Generalized Maxwell model	Epoxy based adhesive	-	Neglects plasticity	
Courtois	2018	Thermodynamics based model	DGEBA epoxy resin	X	Neglects plasticity, applicable to composite manufacturing processes – autoclave, RTM	

Table 3.2 List of works on viscoelastic modeling of polymers

The viscoelastic properties of an adhesive depend on the degree of cure, so the modeling approach was divided into two sections: (1) Viscoelastic model for fully cured material, (2) Cure dependent viscoelastic model.

### **3.2.2.1. Viscoelastic model for fully cured material**

The time and temperature dependent properties of a thermorheologically simple linear viscoelastic material at an unknown temperature (within the range) can be estimated from the properties at a certain reference temperature by using time-temperature superposition principle. The modulus vs. frequency curve at the reference temperature is known as master curve, and the properties at a lower or higher temperature can be obtained by shifting the master curve left or right on the frequency axis. The discrete shift factors for each temperature are recorded and fit to a continuous mathematical model, required for modeling. There are several models available in the literature which can be used to model the shift factors: Williams-Landel-Ferry (Malcolm L. Williams 1955), Doolittle (Doolittle 1951), Johari-Goldstein(Gyan P. Johari 1970), Adam-Gibbs (Adam and Gibbs 1965) etc. Owing to its versatility to a wide range of polymers, the shift factors were fitted to WLF shift function which is given by:

$$\text{Log}(\phi(T)) = -A \frac{T - T_{REF}}{B + T - T_{REF}} \quad (4)$$

where,  $T_{REF}$  is the reference temperature at which the master curve was drawn, and the properties are known, T is the current temperature, while A and B are curve fitting parameters.

The master curve which is a representation of the relaxation behavior of the viscoelastic material can be modeled by Generalized Maxwell Model (M. Kaliske 1997, Meuwissen,

de Boer et al. 2006, Hossain, Possart et al. 2008). The Generalized Maxwell model is mathematically expressed by Prony series expansion:

$$G(t, \alpha) = G_0(\alpha) \left( 1 - \sum_i \frac{G_{i,\alpha=1}}{G_{0,\alpha=1}} (1 - e^{-\beta_i t}) \right) \quad (5)$$

where,  $G_0(\alpha)$  is the instantaneous shear modulus as a function of degree of cure,  $i$  represents the number of terms in Prony series expansion,  $G_{i,\alpha=1}$  is the shear relaxation modulus for the  $i^{\text{th}}$  term for the fully cured material and  $\beta_i$  is the shear decay constant for the  $i^{\text{th}}$  term for the fully cured material.

### **3.2.2.2 Cure dependent viscoelastic model**

The fundamental need in establishing cure dependence is to predict the instantaneous modulus at a certain cure level and an approximation of the relaxation behavior at that cure level. A number of authors have discussed the phenomenon of gelification. A resin's gel point represents a certain degree of cure which is associated with the start of buildup of its mechanical properties (Courtois, Hirsekorn et al. 2018). Several authors assumed that below the gelation point, the adhesive is so compliant that the modulus is negligible and all the stresses are immediately relaxed (Douglas Adolf 1996, Abou Msallem, Jacquemin et al. 2010, Khoun and Hubert 2010). The gel point of a resin typically falls between a cure level of 0.6 and 0.7.

A number of authors have attempted to model the cure dependent modulus of polymers in different ways. The general approach used in modeling is to assume that the cure dependent relaxation behavior (i.e. the relaxation time) is same as that of a fully cured system, with the effective shift factor as a multiplicative product of temperature shift and cure shift (Meuwissen, de Boer et al. 2006, Saseendran 2016). Kim and White (Kim 1996) proposed an enhancement to Maxwell model by making instantaneous modulus, relaxation modulus and decay constants as a function of degree of cure. Another approach is to use phenomenological models like DiBenedetto equation which calculate the glass transition temperature based on the degree of cure and then use the glass transition temperature to predict the shift factors of the viscoelastic model (SINDEE L. SIMON). The approach used in this work is based on the work of Bogetti and Gillespie (Bogetti 1991), who used a mathematical equation to determine the cure dependent equilibrium modulus using the degree of cure and full cure equilibrium modulus. The dependency of the equilibrium modulus will be approximated by using the following equation (Meuwissen, de Boer et al. 2006) :

$$\mu_{\infty}(\alpha) = \mu_{\infty}(1) \left( \frac{\alpha^2 - \alpha_{gel}^2}{1 - \alpha_{gel}^2} \right)^{8/3} \quad (6)$$

where,  $\mu_{\infty}$  is the equilibrium modulus at full cure,  $\alpha_{gel}$  is the cure level at the point of gelification and  $\alpha$  is the cure level at which the modulus is to be determined. For the sake of keeping the formulation simple, we will initially assume that the relaxation behavior at

the time of curing is similar to the relaxation of fully cured material i.e. the temperature dependent shift factors will be used for modeling. The consequences of this assumption will be evaluated in the experimental validation section of the thesis.

### 3.2.3 Plastic Model

The plastic model defines the trend of the stress-strain curve of a material after the yield limit. For defining the temperature and rate dependent nature of adhesives, the plastic constitutive model in the current formulation should take the effects of temperature and strain rate. For the purpose, the flow stress is defined by Johnson-Cook flow stress model which is defined by the following equation:

$$\sigma = (A + B\varepsilon^n)(1 + C\log_{10}\dot{\varepsilon}^*)(1 - T^*)^m \quad (7)$$

$$T^* = (T - T_0)/(T_m - T_0) \quad (8)$$

$$\dot{\varepsilon}^* = \dot{\varepsilon}/\dot{\varepsilon}_{REF} \quad (9)$$

Where  $\varepsilon$  is the plastic strain,  $\dot{\varepsilon}$  is the plastic strain rate,  $\dot{\varepsilon}_{REF}$  is the reference quasi-static plastic strain rate,  $T_0$  is the reference temperature,  $T_m$  is the reference melt temperature, and A, B, C, m and n are material constants. The choice of the plastic model will be evaluated based on the fit of the experimental curves.

The modeling approach is based on two basic assumptions: (i) the conversion dependent behavior of the adhesive is modeled using viscoelastic material description. (ii) The plastic behavior of the adhesive is considered to be active only after attaining fully cured state. The reason behind this assumption is that the viscoelastic stresses in the partially cured adhesive are very small and do not ever cross the plastic yield limit.

The next section of the chapter will discuss the experiments performed and the approach used in calibrating the above material models for the experimental data.

### **3.3 Experiments and model calibration**

The adhesive used in this work is an automotive grade structural adhesive Henkel Teroson EP 5089. It is a single component epoxy based thermosetting adhesive. Two sets of tests were run on the adhesive to calibrate the material models. They are Differential Scanning Calorimetry (DSC) to calibrate the curing kinetics model and Dynamic Mechanical Analysis (DMA) to calibrate the viscoelastic mechanical model.

#### **3.3.1 Calibration of curing kinetics model**

Adhesive curing is an exothermic process which means that energy is expelled when an adhesive is being cured. The energy released during curing of a thermosetting adhesive can be captured using DSC tests as shown in several studies (Badrinarayanan, Lu et al. 2009, Hardis, Jessop et al. 2013, Sheng Dong 2017, Kazan, Zheng et al. 2019). This is achieved by exposing the uncured adhesive specimen to a controlled temperature ramp and analyzing the characteristics of the resulting exothermic cure peak while the adhesive

cures in the DSC. In this work, DSC measurements were performed using DSC Q20 model from TA Instruments. Prior to the test, a specified weight of Teroson EP 5089 adhesive was cooled in the machine from room temperature to -40°C for conditioning for at least 5 minutes. And then the DSC scans were run by heating the sample from -40°C to 250°C at constant heating rates of 0.5, 1, 2, 5, 10 and 20°C/min. DSC tests were also performed at isothermal conditions at 140°C and 160°C. A sample DSC map normalized with the adhesive weight for heating rates of 0.5, 1, 2 and 5 °C/min is shown in *Figure 3.1*.

For the slowest heating rate, the onset of the cure peak for this adhesive is 110 °C and the peak of the exotherm is located at approximately 130 °C. As the heating rate increases, the onset of the peak and the peak move to a higher temperature. For this adhesive, as per the data shown in *Figure 3.2*, the total heat of the reaction i.e. the area under the curve divided by the heating rate is 185J/g. The enthalpy results obtained from DSC tests did not vary too much for different heating rates and were found to be independent of the heating rate.

From the DSC measurements, it is now possible to determine the cure level assuming that the degree of conversion is proportional to the enthalpy generated by the reaction. If  $H_0$  is the reaction enthalpy,  $\Delta H$  is the heat generated in the curing process until a given time  $t$ ,  $\beta$  is the heating rate and  $T$  is the temperature, then the degree of cure can be defined by:

$$\alpha(t) = \frac{\Delta H}{H_0} = \frac{\int_0^t \phi(t') dt}{\int_0^\infty \phi(t') dt} \xrightarrow{dT=\beta dt} \frac{\int_0^T \phi(T') dT'}{\int_0^\infty \phi(T') dT'} = \alpha(T(t)) \quad (7)$$

Based on the above equation, the measured DSC results for EP 5089 were numerically transformed to give conversion level versus temperature and time as shown in *Figure 3.2* and *Figure 3.3* respectively. The same procedure was used to obtain degree of cure for all the non-isothermal and isothermal DSC measurements.

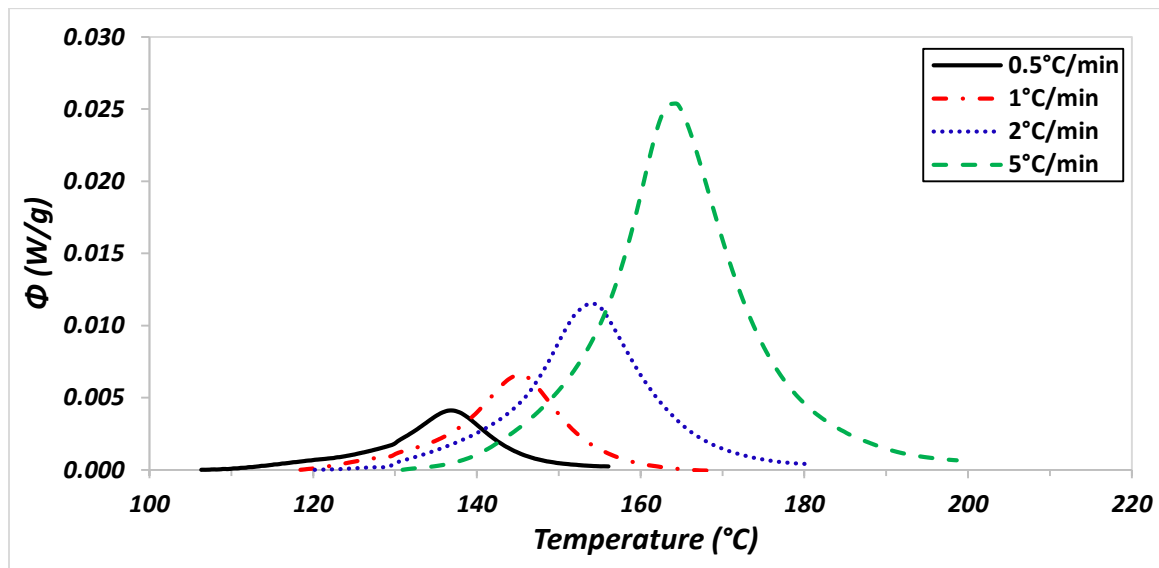


*Figure 3.1 Sample DSC heat flow scans normalized with specimen weight for different heating rates*

It is a clear observation from *Figure 3.3* that the adhesive cures at a faster rate for a higher heating rate. This means that an adhesive can be cured faster by increasing the cure temperature. But, there is a physical limit to the maximum curing temperature, limited by the degradation temperature of the particular adhesive and increased curing shrinkage at higher temperatures (Marques, da Silva et al. 2014).

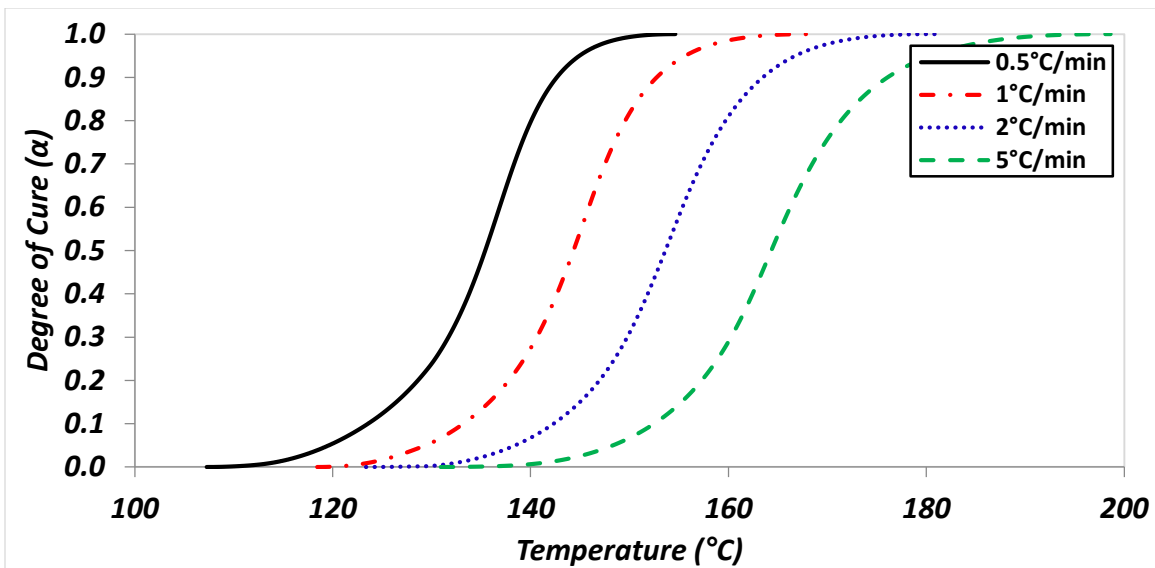


Figure 3.2 Degree of cure vs. temperature obtained from DSC measurements on different heating rates

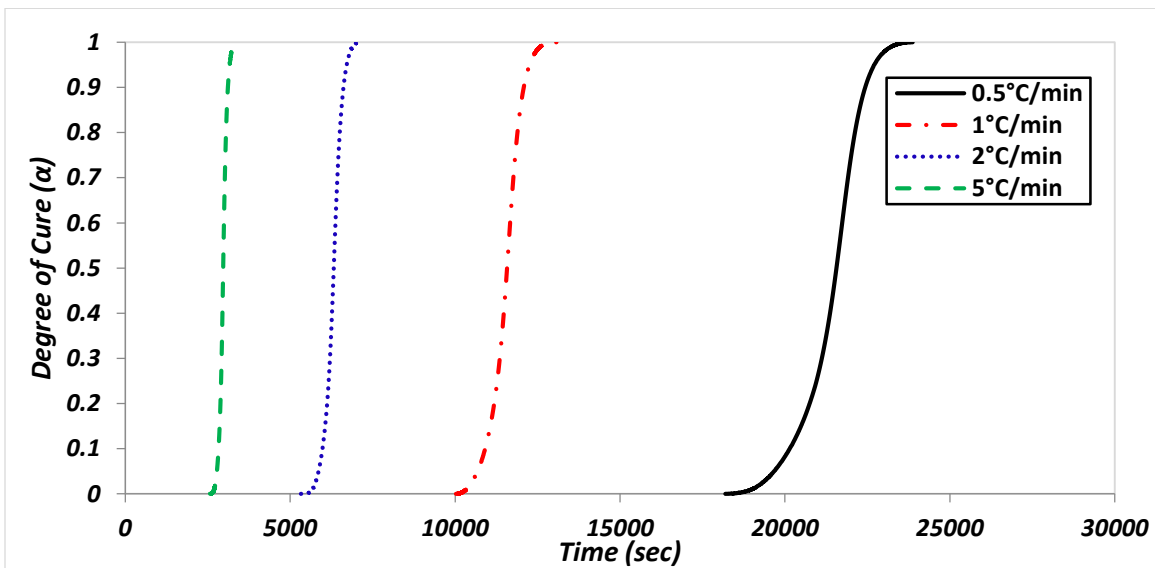


Figure 3.3 Degree of cure vs. time obtained from DSC measurements on different heating rates

The test data for heating rates of 0.5, 1, 2 and 5 °C/min was used for model calibration, while the results for heating rates of 10 and 20 °C/min and isothermal tests at 140 °C and 160 °C were used for the validation of curing kinetics model. The next task was to fit the

experimentally obtained degree of cure curves to Kamal's model. In this approach, first the activation energy of the reaction was calculated from the experimental data using isoconversion method (D. Rosu 2002, Cai, Li et al. 2008, Badrinarayanan, Lu et al. 2009, Li, Huang et al. 2010, Hardis, Jessop et al. 2013, Duemichen, Javdanitehran et al. 2015), using the logarithmic form of kinetics equation Eq. (1) combined with Eq. (2):

$$\ln \frac{d\alpha}{dt} = \ln[Af(\alpha)] - \frac{E_a}{RT} \quad (8)$$

The slope of  $\ln \frac{d\alpha}{dt}$  versus  $1/T$  for the same value of  $\alpha$  gives the value of activation energy.

The curves were drawn for cure levels ranging from 0.05 to 0.95. Then, isoconversion lines were drawn on the curves for different values of  $\alpha$  and the slope was recorded. *Figure 3.4* shows the curves for different heating rates and isoconversion line drawn for a cure level of 0.5.

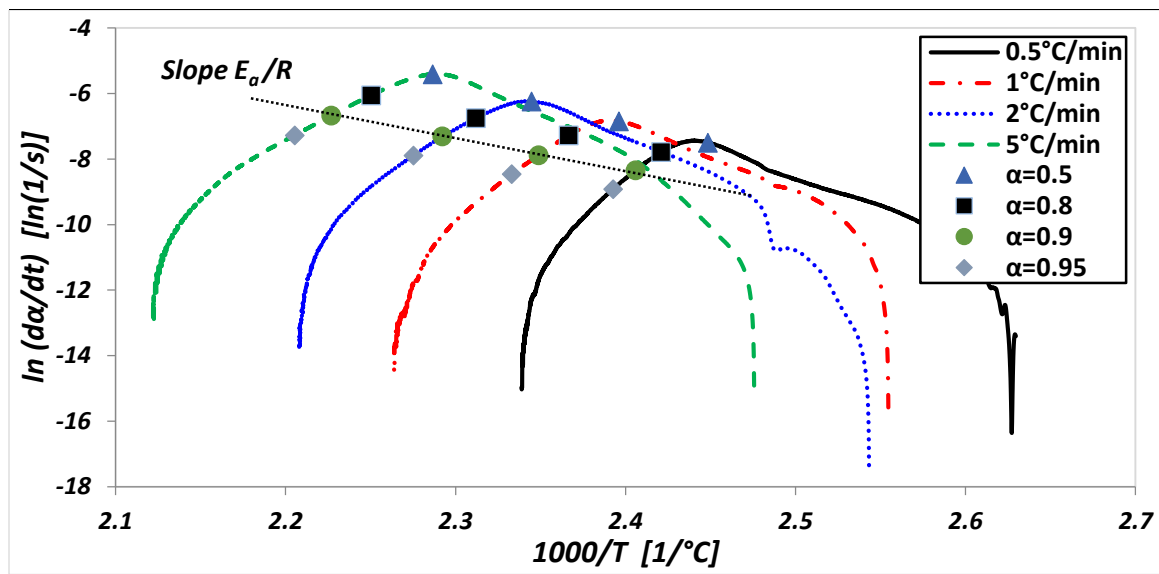


Figure 3.4 Arrhenius plots and isoconversion line for  $\alpha = 0.9$

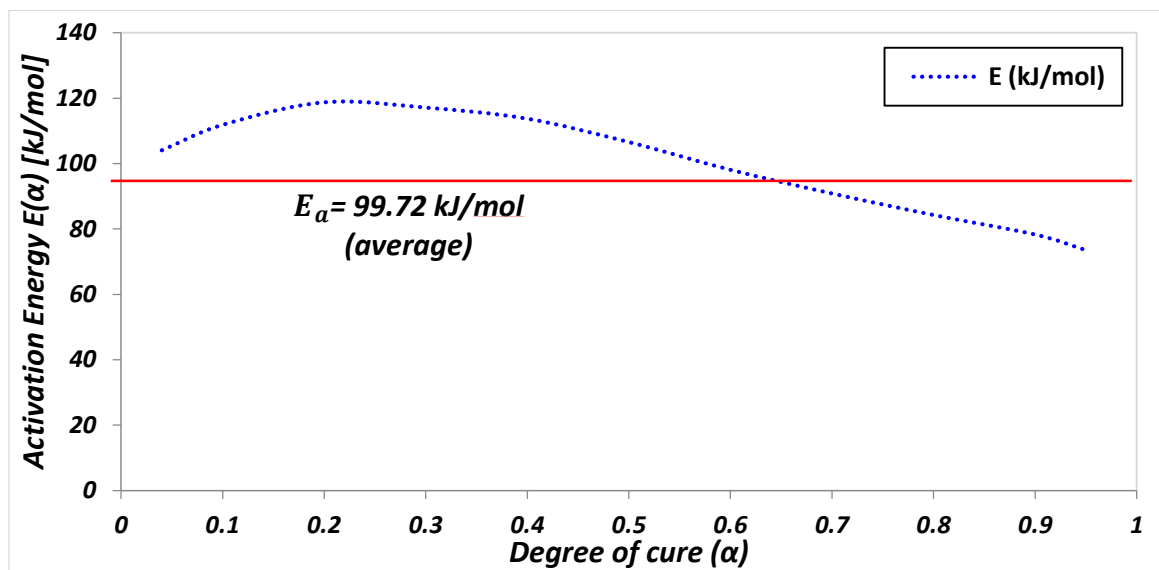


Figure 3.5 Activation energy variation with cure level, average activation energy line

The activation energy of the reaction varies as the reaction progresses. The values of activation energy as a function of cure level are shown in *Figure 3.4*. The activation energy

peaks as in the middle and there is a visible drop in the energy at the beginning and at the end of the reaction. For the sake of simplicity, an average activation energy (99.72 kJ/mol) was used for further calibration. To determine the value of the remaining parameters, Eq. (1) was written in the following form:

$$\frac{d\alpha}{dt} e^{\frac{E_a}{RT}} = Af(\alpha) \quad (9)$$

With all the parameters on the left hand side of Eq. (9) now known, a normalized plot for the left hand side was drawn for each heating rate. The obtained curves were fit to Eq. (3) using non-linear regression and the best fit curve parameters for  $f(\alpha)$  were obtained.

The last parameter - pre-exponential factor A was found by scaling the  $f(\alpha)$  approximation curve to the experimental data. The value of A is a function of the degree of cure. A large scatter was observed at  $\alpha$  close to 0 and 1. Therefore, the value of A was approximated for  $0.01 < \alpha < 0.99$ . The optimized values of all the fitting parameters of the curing kinetics Eq. (1) are given in *Table 3.3*.

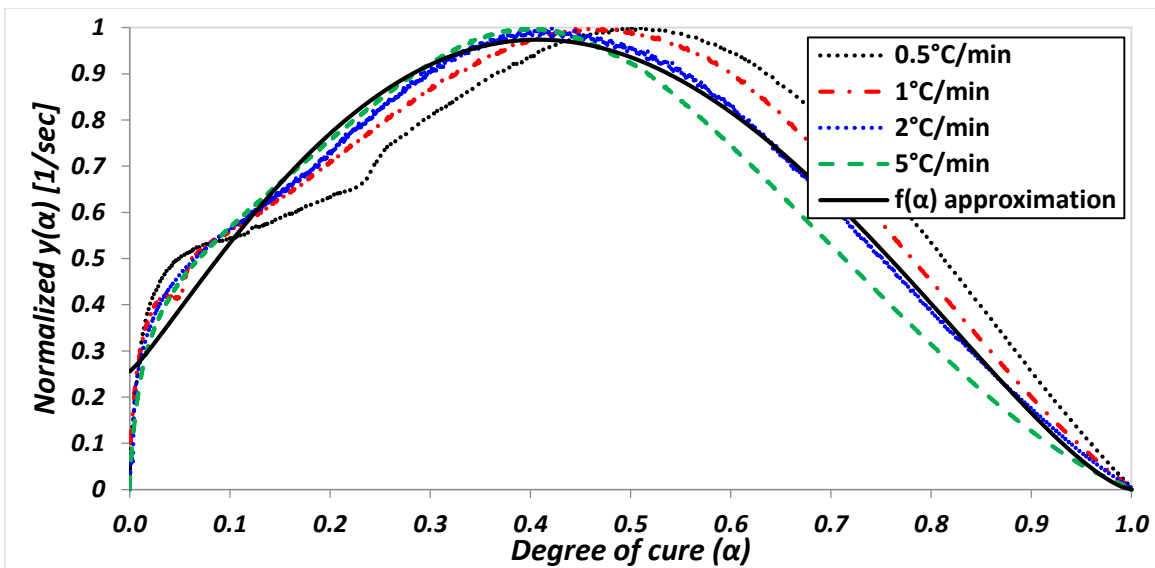


Figure 3.6  $f(\alpha)$  best fit curve for experimental curves

A	$E_a$ (kJ/mol)	$k_1$	$k_2$	m	n
$e^{22.06}$	99.72	0.26	5.16	1.15	1.46

Table 3.3 Calibrated parameters for curing kinetics model

The calibrated curing kinetics model yields very good estimations for the experimental curing curves for heating rates of 10 and 20 °C/min and isothermal tests at 140 °C and 160 °C. A comparison of the model estimation and experimental curves is shown in *Figure 3.7* and *Figure 3.8*.

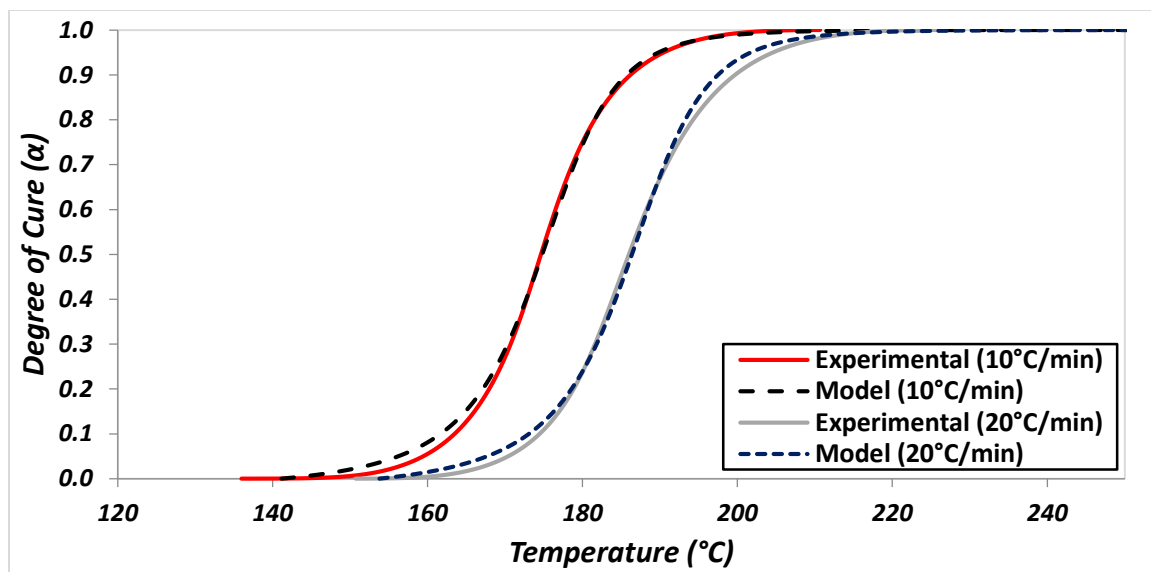


Figure 3.7 Comparison of model estimation vs experimental curves at non-isothermal condition

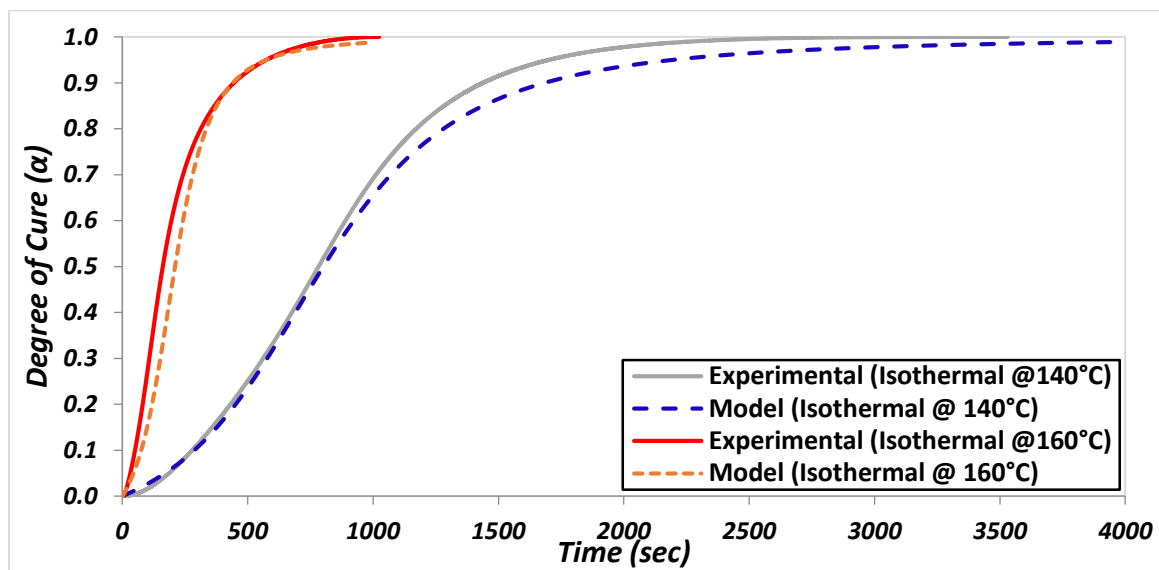


Figure 3.8 Comparison of model estimation vs experimental curves at isothermal condition

### **3.3.2 Calibration of viscoelastic model**

#### **3.3.2.1. Fully cured material**

Henkel Teroson EP 5089, being an epoxy based adhesive shows viscoelastic properties.

The viscoelastic properties dependent on temperature and frequency are measured using a dynamic mechanical analysis system (DMA). The output of the DMA tests are viscoelastic moduli (storage and loss modulus) measured at different frequencies and temperatures. According to the theory of viscoelasticity, the real part of the modulus – storage modulus  $\mu_S$  and the imaginary part of the modulus – loss modulus  $\mu_L$  combine to form a complex modulus  $\mu = \mu_S + i\mu_L$ , where  $i$  is the imaginary unit number. The damping loss factor can be calculated by  $\eta = \tan\delta = \frac{\mu_L}{\mu_S}$  where  $\delta$  is the phase shift between real and imaginary part of modulus.

In this work, DMA measurements were performed with a bar in a torsional configuration.

The DMA setup measures stress vs. strain curve which can be used to calculate complex moduli. The modulus was obtained for a fully cured specimen for a combined frequency and temperature sweep, with a 0.1% strain amplitude, for a frequency range of 0.1 Hz to 100 Hz at a temperature range of -50 °C to 200 °C at a step of 10 °C. The storage modulus as a result of combined temperature and frequency sweep from DMA tests is shown in *Figure 3.9*. As expected, it is visible that with a rise in temperature, the material softens and the modulus decreases.

Using time-temperature superposition principle applicable to linear viscoelastic materials, the modulus curves were shifted horizontally on the logarithmic frequency axis as described in several publications (Saseendran 2016). For a reference temperature of 100 °C, the curves at higher temperature in the lower portion of the plot were shifted to the left (to lower frequencies) and the curves at lower temperature were shifted to the right (to higher frequencies), in order to generate a smooth continuous curve. The frequency shift factors were recorded for each temperature and were later fit to WLF shift function, given in Eq. (4). The shifted modulus curve (known as Master curve at 100 °C) was drawn for storage, loss modulus and loss factor, as shown in *Figure 3.10*. The scatter in the loss modulus values at higher temperatures is a result of phase changes in the material due to the actual temperature going beyond the glass transition temperature of the full cured material.

The next task was to fit the shift factors and the experimental master curve at 100 °C to models given in Eq. (4) and Eq. (5) respectively. The log of shift factors was fit to WLF shift function using non-linear regression. A comparison of the experimental and estimated values is shown in *Figure 3.11*. It suggests that the shift factor is negative for temperatures higher than 100 °C and positive for temperatures lower than 100 °C, which means higher temperatures shift to the left and lower temperatures shift to the right on the frequency axis. The calculated parameters for Eq. (4) are given in *Table 3.4*.

The developed master curve was fit to 16 terms of Prony series expansion using numerical techniques. It can be challenging to fit the storage modulus and loss modulus simultaneously to Prony series. It was observed that transforming the master curve from frequency domain to time domain before fitting helps in easier calibration of the model. The results of best fit of Prony series expansion to the experimental values is shown in *Table 3.4* and *Figure 3.12*. The storage modulus estimation by the model has a good overlap with the experimental values. The estimations for loss modulus and loss factor are wavy, which is typical for Prony series expansion, but represent the general trend of the experimental values in a satisfactory manner.

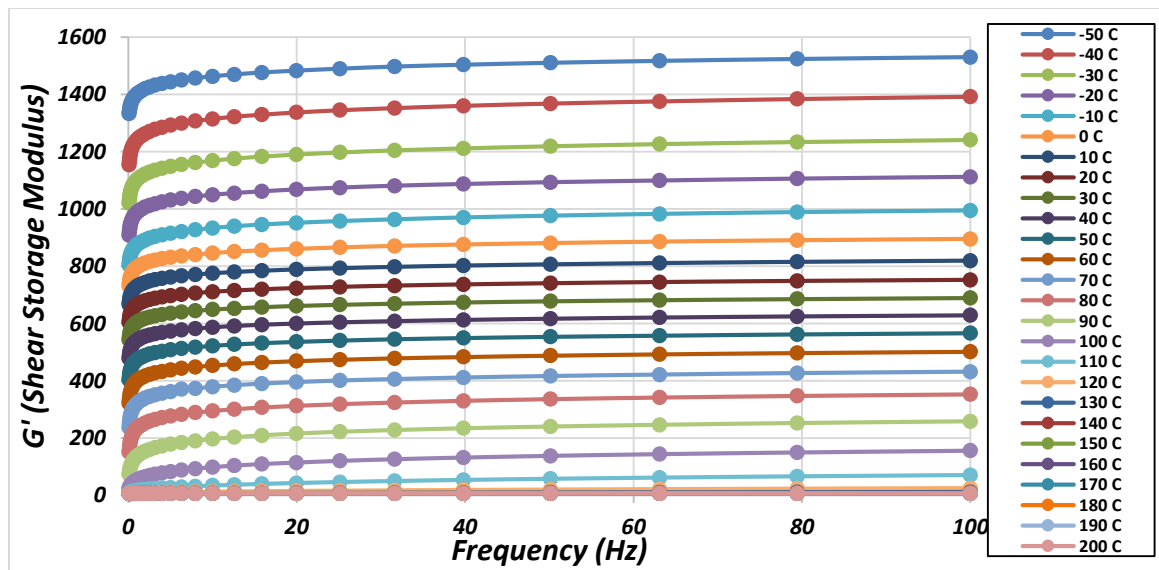


Figure 3.9 Shear storage modulus vs. frequency as a result of combined temperature-frequency sweep

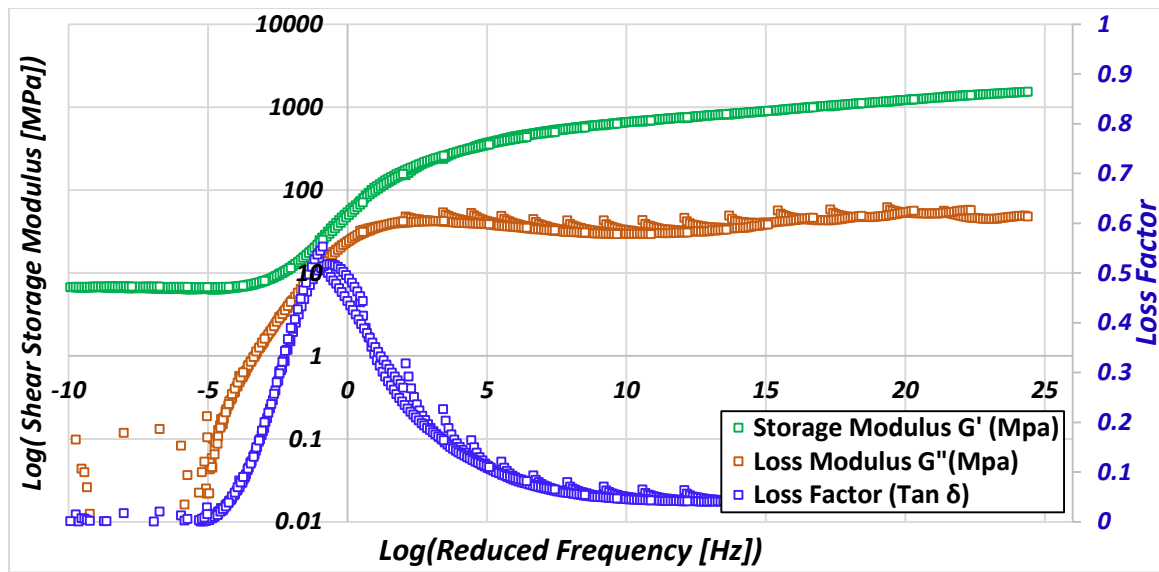


Figure 3.10 Master curve showing shear storage, loss modulus and loss factor at 100 °C

According to the Prony fitting results shown in *Table 3.4*, the instantaneous modulus ( $G_0$ ) of the material is 1577.67 MPa, while the long term modulus ( $G_\infty$ ) of the material is 6.63 MPa. This means that the material relaxes with time and after a fairly long time (~1E6 seconds) the modulus drops to 6.63 MPa.

The bulk modulus of the adhesive was calculated based on a Poisson's ratio of 0.4 and the instantaneous shear modulus of 1577.67 MPa. The bulk modulus was taken to be independent of time and conversion,  $K_\infty(\alpha) = K_0 = K_\infty = 7362.46$  MPa.

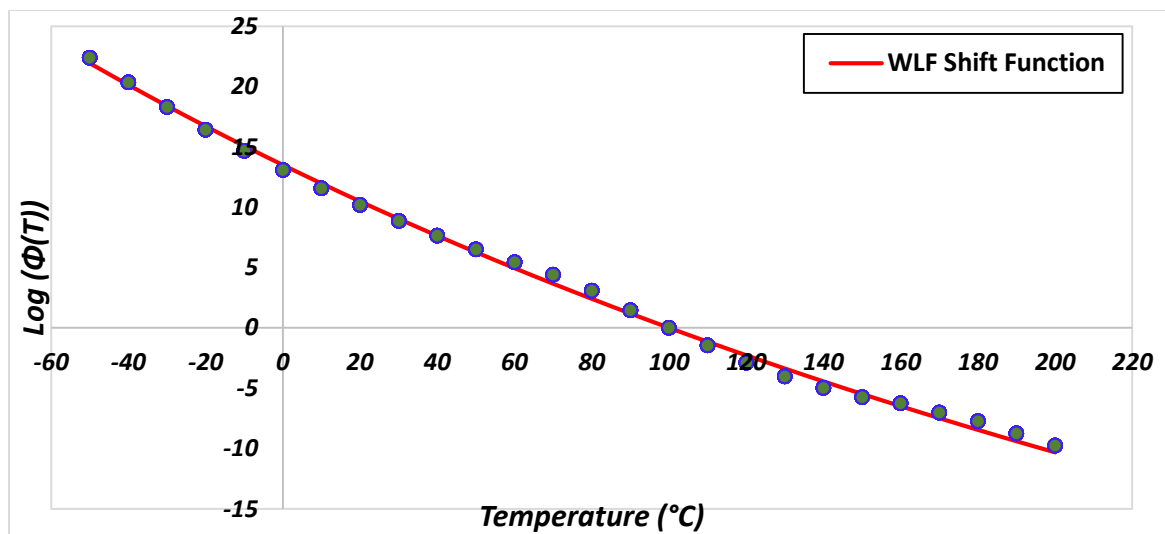


Figure 3.11 Comparison of Log of experimental shift factors and WLF model estimation

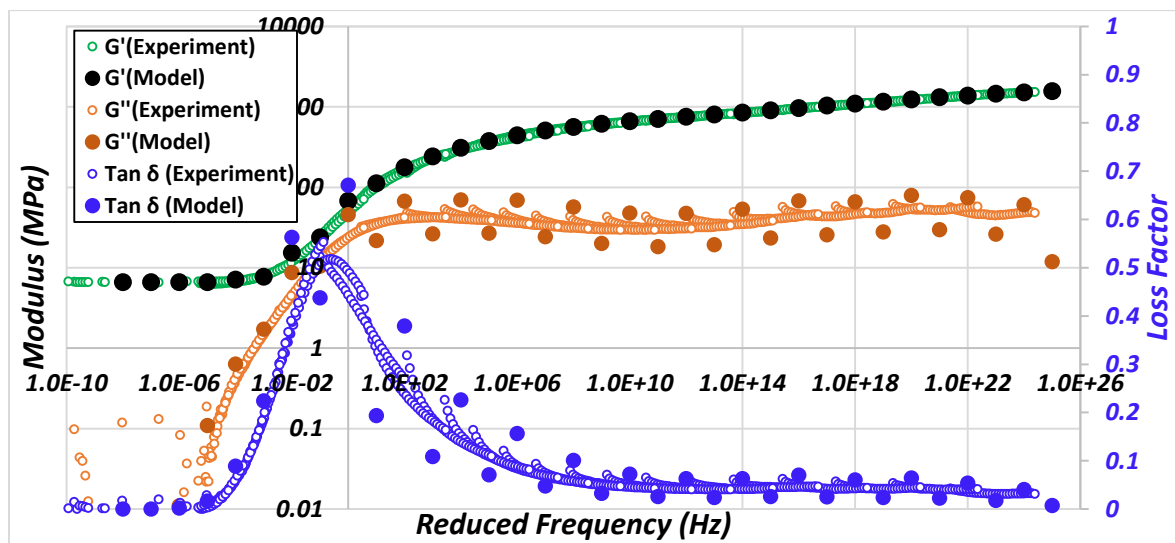


Figure 3.12 Comparison of Prony series fitting vs experimental values

	Shear Relaxation Modulus ( $G_i$ ) [Mpa]	Shear Decay Constant ( $\beta_i$ ) [Hz]		Shear Relaxation Modulus ( $G_i$ ) [Mpa]	Shear Decay Constant ( $\beta_i$ ) [Hz]
G1	119.0202	1.00E+24	G9	1.09E+02	1.00E+08
G2	143.4906	1.00E+22	G10	1.34E+02	1.00E+06
G3	153.1073	1.00E+20	G11	1.34E+02	1.00E+04
G4	126.4329	1.00E+18	G12	1.30E+02	1.00E+02
G5	131.2659	1.00E+16	G13	8.89E+01	1.00E+00
G6	102.4958	1.00E+14	G14	1.56E+01	1.00E-02
G7	91.12014	1.00E+12	G15	9.33E-01	1.00E-04
G8	91.78917	1.00E+10	G16	1.00E-16	1.00E-06
$G_0$	1577.67 MPa				
$G_\infty$	6.63 MPa				
WLF A	-87.93				
WLF B	751.29				

Table 3.4 Parameters obtained for best fit of WLF function: Eq. (4) and Prony series: Eq. (5)

### 3.3.2.2 Cure dependent viscoelastic model

To capture the curing dependency of the material, DMA tests were run on an uncured sample of the adhesive between two plates in torsional configuration at 0.3 rad/s oscillation with a 0.1% strain amplitude. The adhesive was allowed to cure in the DMA while two sets of tests were run with dynamic temperature ramps of 5°C/min and 10°C/min from room temperature to 180°C and 220°C respectively. The measurement results are shown in Figure 3.13 and Figure 3.14.

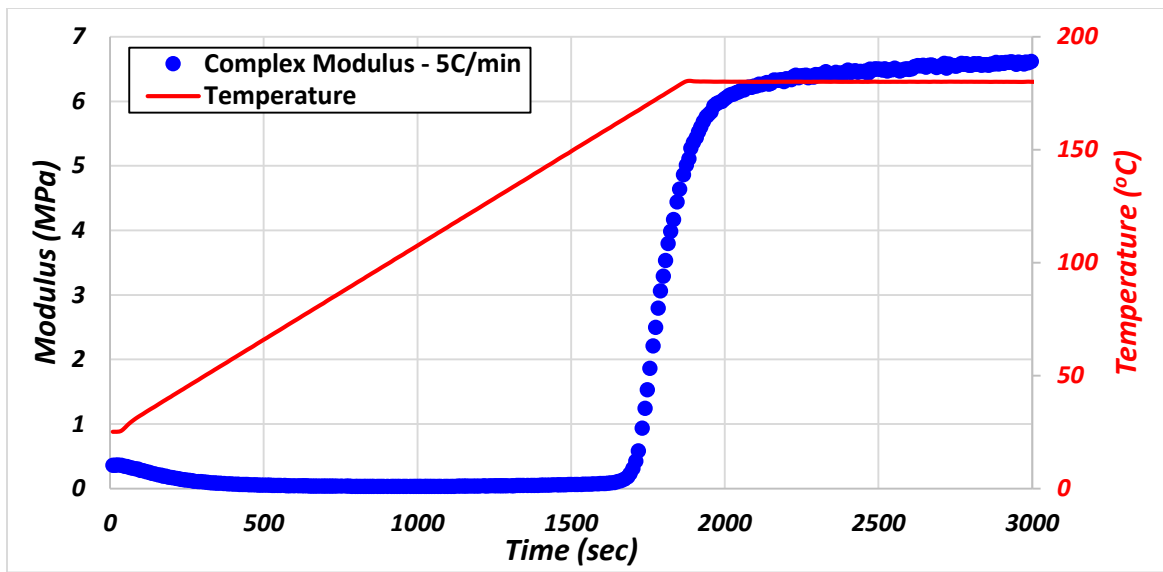


Figure 3.13 Development of shear modulus with time for a temperature ramp of 5°C/min

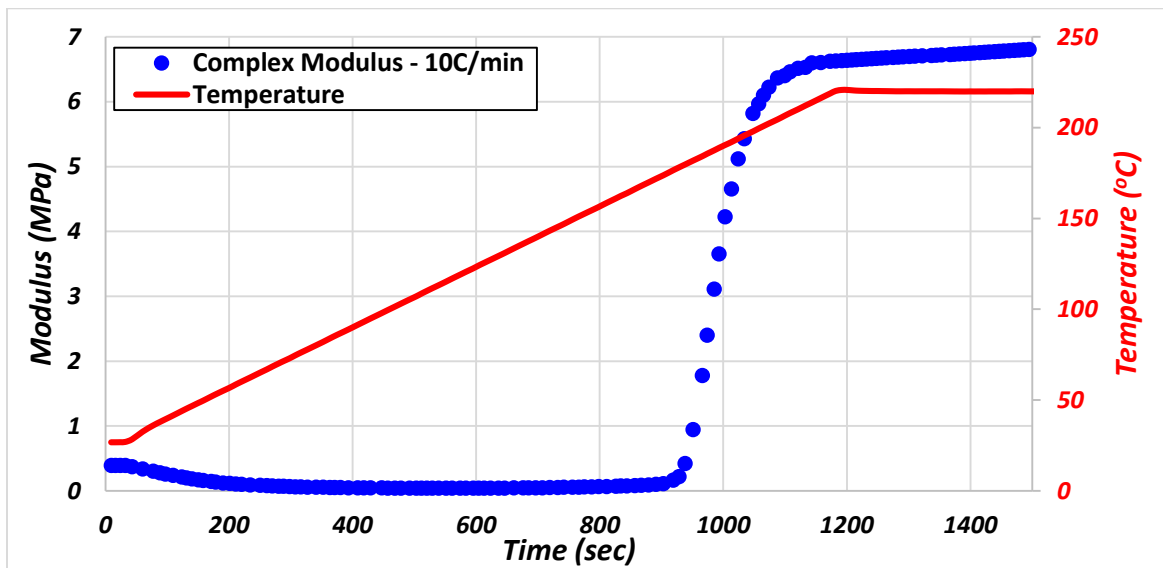


Figure 3.14 Development of shear modulus with time for a temperature ramp of 10°C/min

The test data shows that the modulus for the uncured adhesive was negligible in the beginning and as the temperature increased with time, the adhesive gets cured and the

modulus picks up and reaches a steady value which is very close to the value of equilibrium modulus (6.63 MPa) previously calculated by Prony series for full cured adhesive, in section 3.2.1. The experimental results were transformed from modulus vs time and temperature to modulus vs cure using the curing kinetics model developed in section 3.1. The experimental results were fit to Eq. (6) and the best fitting for the data is obtained at  $\alpha_{gel} = 0.56$  using the full cured equilibrium modulus value of 6.63 MPa. Figure 3.15 shows a comparison of the experimental results for modulus vs. cure along with the model estimation.

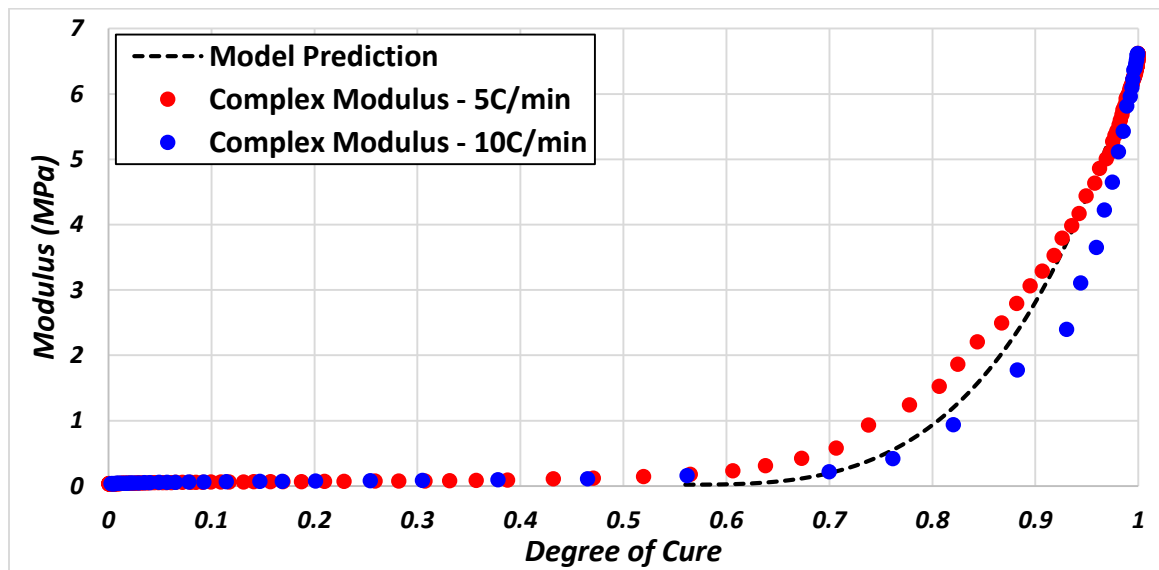


Figure 3.15 Comparison of experimentally obtained modulus growth with cure vs model estimation

Thus, the adhesive material models (i) curing kinetics model and (ii) viscoelastic mechanical models were calibrated for EP5089. In the next section, the plastic model was calibrated for a fully cured adhesive EP5089.

### 3.3.3 Calibration of plastic model

The plastic properties of the adhesive were studied by conducting tensile tests on fully cured adhesive specimens. The preparation of adhesive tensile specimens of uniform thickness and produced under same heating conditions was a tricky task. New methodology was developed to produce adhesive specimens by curing sheets of adhesive in a furnace and shearing them using a specially created die. The process started with curing a sheet of adhesive between two parallel steel sheets. The procedure is depicted schematically in Figure 3.16. Then the adhesive sheets were put into a specially prepared die to shear the tensile dog bone specimens from them as depicted in *Figure 3.17*.

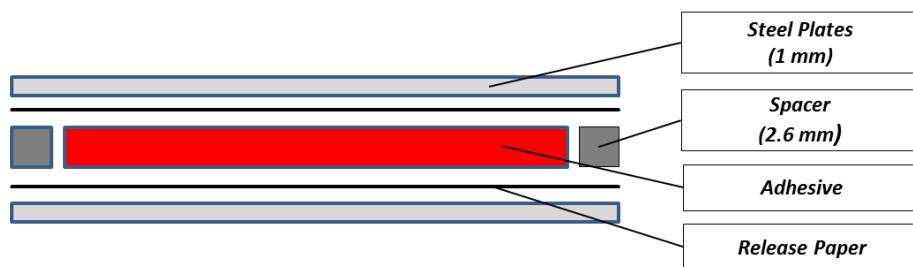
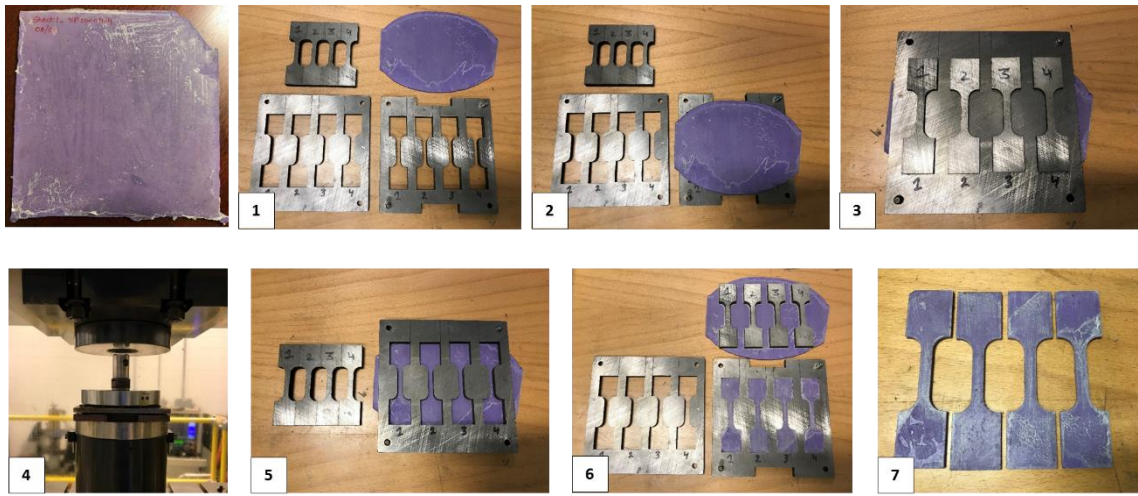


Figure 3.16 Adhesive sheet preparation – cured between two steel sheets



*Figure 3.17 Tensile specimen preparation using specially prepared die*

The adhesive specimens were then pulled in tension on an Instron quasi-static electromechanical load frame. The setup consisted of a furnace mounted on the load frame for conducting high temperature tests. The furnace had a small glass window opening through which optical strain measurements were done using Gom Aramis 3D DIC system. The test setup included specially designed grips for high temperature testing, which allow self-alignment of the specimen. The test setup is shown in *Figure 3.18*. The tests were performed at four temperatures ( $25^{\circ}\text{C}$ ,  $60^{\circ}\text{C}$ ,  $90^{\circ}\text{C}$ ,  $120^{\circ}\text{C}$ ) and three strain rates ( $1\text{E-}3 / \text{s}$ ,  $1\text{E-}2 / \text{s}$ ,  $1\text{E-}1 / \text{s}$ ). The tests at different strain rates were performed at room temperature, while the tests at different temperatures were performed at the quasi-static strain rate  $1\text{E-}3 / \text{s}$ .

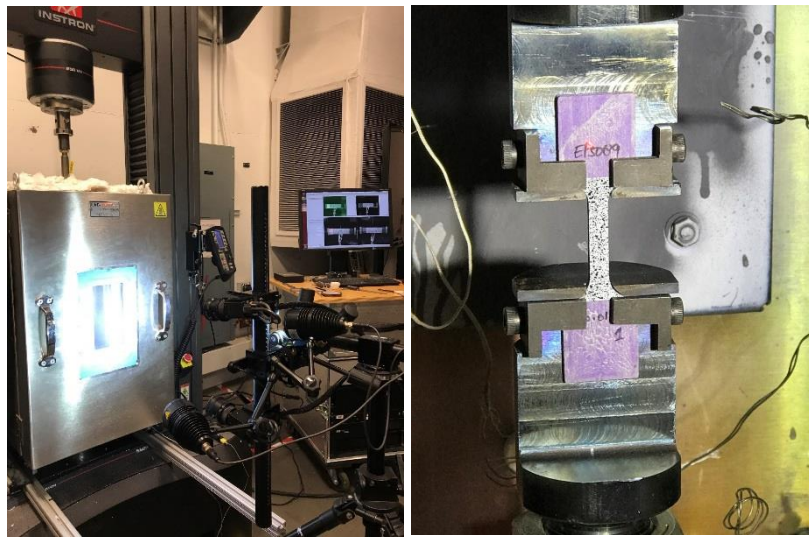


Figure 3.18 Test setup for high temperature tensile tests on adhesives

The stress-strain curves obtained from the tests are shown in *Figure 3.19* and *Figure 3.20*.

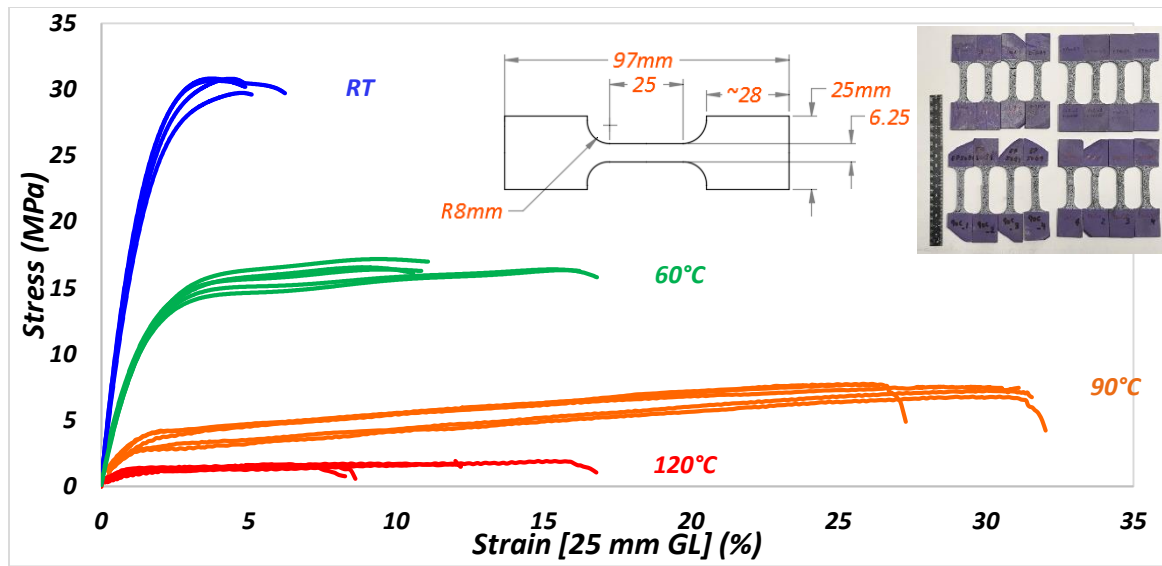


Figure 3.19 Stress-Strain curves for the adhesive EP5089 at different temperatures at strain rate 0.001/s

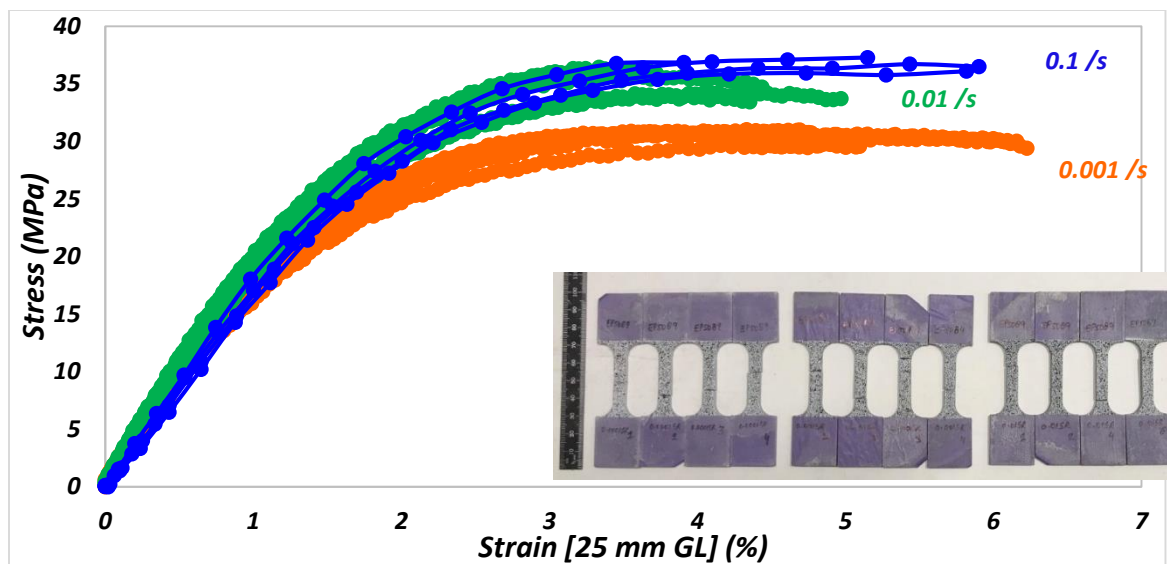


Figure 3.20 Stress-Strain curves for the adhesive EP5089 at different strain rates at room temperature

The stress strain curves show the temperature dependence of strength and the modulus. With increase in the temperature, there is a drop in the strength and the modulus of the adhesive. Similarly, the tests at different strain rates show that the strength of the adhesive rises with the increase in the strain rate. For the sake of uniformity, the trend of the curve beyond a strain of 2% was assumed plastic. The obtained plastic stress-strain curves were fit to John-Cook flow stress model and the best fit parameters for the model are given in *Table 3.5*. The model best fit vs. experimental curves are shown in *Figure 3.21* and *Figure 3.22*.

A	B	C	m	n	$T_o$	$T_m$	$\dot{\epsilon}_{REF}$
4.5	20.5	0.078	1.66	0.18	333	408	0.001

Table 3.5 J-C model parameters for EP5089 adhesive

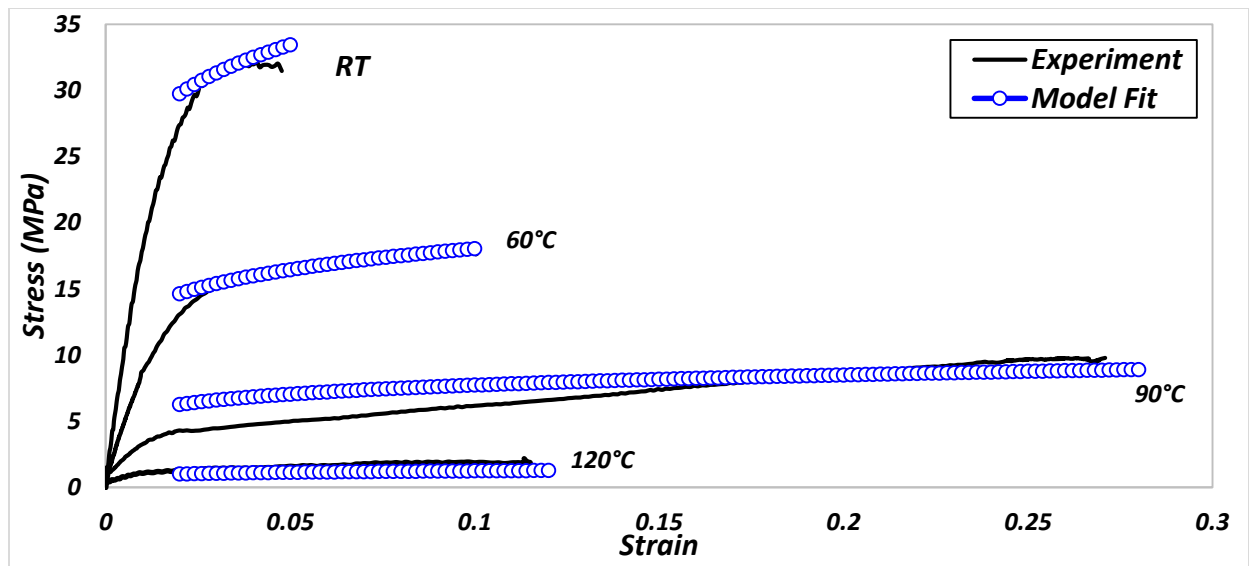


Figure 3.21 Experiment vs. J-C model fit for stress-strain curves at different temperatures

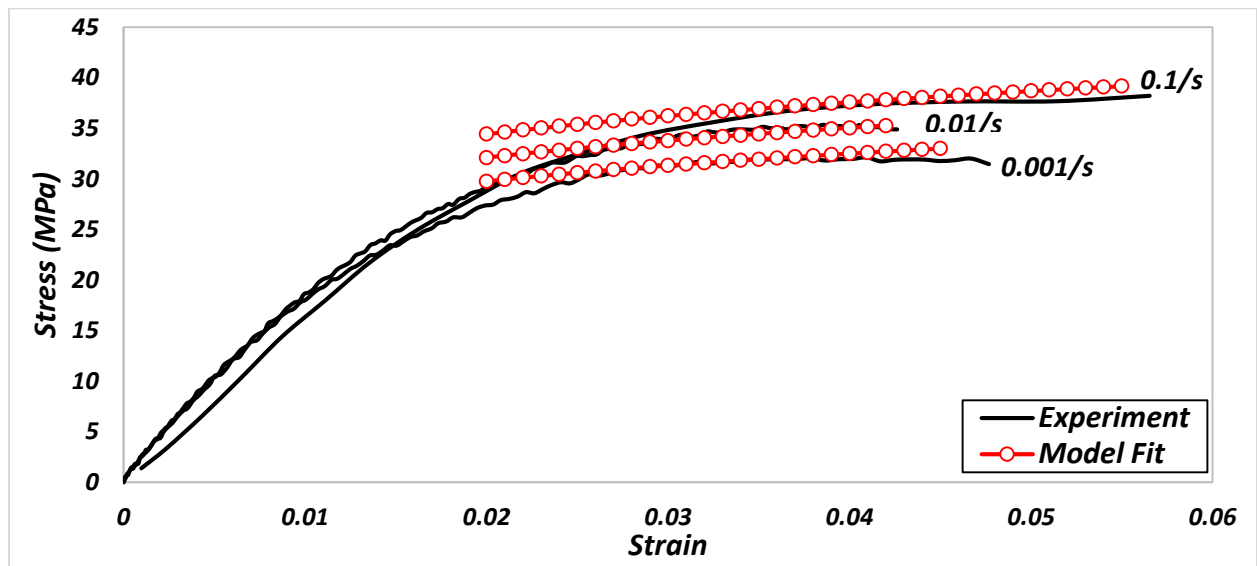


Figure 3.22 Experiment vs. J-C model fit for stress-strain curves at different strain rates

It is clear in *Figure 3.21* that the trend in the hardening of the stress-strain curves lowers with increasing temperature, except the curve at 90°C which is an anomaly. Considering the general level of yield stresses, the J-C model fits the stress-strain curves at different

temperatures and strain-rates very well, but is not able to capture the change in the hardening at 90°C.

Thus, the adhesive material models (i) curing kinetics model and (ii) viscoelastic mechanical model (iii) Plastic mechanical model were calibrated for EP5089. In the next chapter, an explicit formulation of the material models for a user defined material card in LS-DYNA will be discussed.

# **Chapter 4**

## **4. USER-DEFINED MATERIAL SUBROUTINE (UMAT) IN LS-DYNA**

The material models discussed in Chapter 3 were coded in FORTRAN to generate a user defined material subroutine in LS-DYNA. The developed material card was used to run simple FE simulations to test the performance of the material card on simple models and capture the isolated behavior of each material model (Curing Kinetics / viscoelastic / plastic) and then the material card was used to run complex multi-body simulations. The general approach used for material card development is shown in *Figure 4.1*.

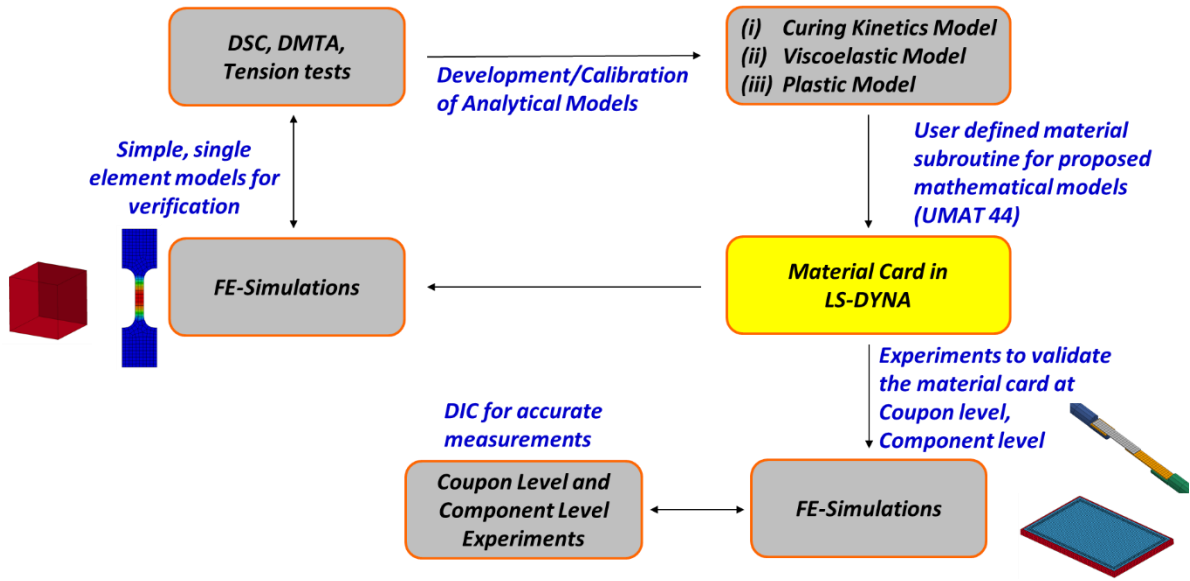


Figure 4.1 General Approach for UMAT development

The material card formulation was based on incremental theory of plasticity (KWANSOO CHUNG 1993, Abedrabbo, Pourboghrat et al. 2006). According to this theory, the strain increment for each time step 'n', the previous stress state 'n-1' and other history variables are provided to the code and are used in solving the stress state of the current time step 'n'. The code initially assumes that the strain increment in the time step is totally viscoelastic and a viscoelastic predictor stress state called as trial stress is calculated using the viscoelastic material model. The code then calculates the effective stress and compares it to the yield stress at that total strain which is calculated using the plastic flow stress constitutive model. If the effective stress at the time step exceeds the flow stress, it represents that the material has yielded. The stresses are then cut back by the plastic corrector term to fall on the flow stress curve using cutting plane algorithm. After several

iterations, a converged value of plastic strain and stress state is obtained and is reported back to the program.

The implementation of curing kinetics model was fairly straightforward as it only took the value of the current temperature and the value of degree of cure from the previous time-step as a history variable. The equation was directly coded in FORTRAN. The implementation of viscoelastic and plastic model was complicated and has been discussed in detail in this chapter.

## **4.1 Implementation of viscoelastic material description**

The implementation of viscoelastic model was based on a generalized Maxwell element. Considering a purely isochoric viscoelastic behavior, the stress tensor for the next time step is the sum of the purely elastic stress and a factor governing the viscoelastic contribution from each branch of the generalized Maxwell element:

$$dev \underline{\sigma}^{n+1} A = dev \underline{\sigma}_0^{n+1} + \sum_{j=1}^N h_j^{n+1} \quad (10)$$

Where n is the time step and N is the number of branches in the Maxwell model.

$$\underline{\sigma}_0^{n+1} = \bar{C}^e \underline{\varepsilon}^{n+1} \quad (11)$$

The vectors  $\underline{h}_j$  are internal state variables for each branch  $j$  of the Maxwell element which account for the stress contribution due to the viscoelastic behavior. They describe the relaxation behavior in terms of the decay of stresses.

The isotropic elasticity tensor operator in the Eq. (11) is:

$$\bar{\bar{C}}^e = \lambda \underline{\underline{1}} \otimes \underline{\underline{1}} + 2\mu_0 \bar{\bar{\Pi}} \quad (12)$$

If  $\lambda = K_\infty - 2/3\mu_0$  and  $\mu_\infty$  are the first and second Lame constants and  $(\underline{\underline{1}} \otimes \underline{\underline{1}})_{ijkl} = \delta_{ij}\delta_{kl}$  and  $\Pi_{ijkl} = \frac{1}{2}(\delta_{ik}\delta_{jl} + \delta_{il}\delta_{jk})$  are the second order and symmetric fourth order identity tensors respectively.

Applying the same relationship for the viscoelastic decay of stresses also to the volumetric stress, the stress tensor for the step  $n+1$  can be calculated from the given equation:

$$\begin{aligned} \underline{\sigma}^{n+1} &= dev \underline{\sigma}^{n+1} + \frac{1}{3} tr \underline{\sigma}^{n+1} \underline{\underline{1}} \\ &= dev \underline{\sigma}_0^{n+1} + \sum_j \underline{h}_j^{n+1} + \left( K_\infty \varepsilon_V^{n+1} + \sum_j v_j^{n+1} \right) \end{aligned} \quad (13)$$

Because

$$tr \underline{\sigma}^{n+1} = K_\infty \varepsilon_V^{n+1} \quad (14)$$

The evolution of the history variables is defined by the following expressions:

For the isochoric part,

$$\underline{h}_j^{n+1} = \exp\left(-\frac{\Delta t}{\tau_j}\right) \underline{h}_j^n + \gamma_j \frac{1 - \exp\left(-\frac{\Delta t}{\tau_j}\right)}{\frac{\Delta t}{\tau_j}} [\operatorname{dev} \underline{\sigma}_0^{n+1} - \operatorname{dev} \underline{\sigma}_0^n] \quad (15)$$

For the volumetric part,

$$v_j^{n+1} = \exp\left(-\frac{\Delta t}{\kappa_j}\right) v_j^n + k_j \frac{1 - \exp\left(-\frac{\Delta t}{\kappa_j}\right)}{\frac{\Delta t}{\kappa_j}} K_\infty \Delta \varepsilon_V \quad (16)$$

In these expressions, the relaxation functions are defined in a normalized form, i.e. instead of the shear modulus and the bulk modulus the dimensionless values  $\gamma_j = \frac{\mu_j}{\mu_\infty}$

and  $k_j = \frac{K_j}{K_\infty}$  are used.

$$\operatorname{dev} \underline{\sigma}_0^n = \underline{\sigma}_0^n - \frac{1}{3} \operatorname{tr}(\underline{\sigma}_0^n) \underline{1} = \bar{\bar{C}}^e \underline{\varepsilon}^n - K_\infty \varepsilon_V^n \underline{1} \quad (17)$$

The last term in Eq. (15) may now be transformed in the following way:

$$\begin{aligned} \operatorname{dev} \underline{\sigma}_0^{n+1} - \operatorname{dev} \underline{\sigma}_0^n &= \operatorname{dev} (\underline{\sigma}_0^{n+1} - \underline{\sigma}_0^n) \\ &= \operatorname{dev} (\bar{\bar{C}}^e \underline{\varepsilon}^{n+1} - \bar{\bar{C}}^e \underline{\varepsilon}^n) \\ &= \operatorname{dev} (\bar{\bar{C}}^e \Delta \underline{\varepsilon}) = \bar{\bar{C}}^e \Delta \underline{\varepsilon} - K_\infty \Delta \varepsilon_V \underline{1} \end{aligned} \quad (18)$$

Substituting Eq. (18) into (15) gives

$$\underline{h}_j^{n+1} = \exp\left(-\frac{\Delta t}{\tau_j}\right) \underline{h}_j^n + \gamma_j \frac{1 - \exp\left(-\frac{\Delta t}{\tau_j}\right)}{\frac{\Delta t}{\tau_j}} [\bar{\bar{C}}^e \Delta \underline{\varepsilon} - K_\infty \Delta \varepsilon_V \underline{1}] \quad (19)$$

An equation for the stress update can be derived using Eq. (13)

$$\begin{aligned}
\underline{\sigma}^{n+1} &= \frac{1}{3} \operatorname{tr} \underline{\sigma}_0^{n+1} + \sum_j v_j^{n+1} \underline{1} + \operatorname{dev} \underline{\sigma}_0^{n+1} + \sum_j \underline{h}_j^{n+1} \\
&= \underline{\sigma}_0^{n+1} + \sum_j v_j^{n+1} + \sum_j \underline{h}_j^{n+1} \\
&= \bar{\bar{C}}^e \underline{\varepsilon}^{n+1} + \sum_j v_j^{n+1} \underline{1} + \sum_j \underline{h}_j^{n+1}
\end{aligned} \tag{20}$$

The above equations were changed to Voigt notation in order to develop a FORTRAN algorithm which can be used to implement in a user defined material subroutine in LS-DYNA.

$$\begin{aligned}
\underline{\sigma} &= (\sigma_{11} \ \sigma_{22} \ \sigma_{33} \ \sigma_{12} \ \sigma_{23} \ \sigma_{13})^t \\
\underline{\varepsilon} &= (\varepsilon_{11} \ \varepsilon_{22} \ \varepsilon_{33} \ \varepsilon_{12} \ \varepsilon_{23} \ \varepsilon_{13})^t
\end{aligned} \tag{21}$$

In this notation, the first term of Eq. (20) has the following form:

$$\bar{\bar{C}}^e \underline{\varepsilon}^{n+1} = \begin{bmatrix} \lambda + 2\mu_\infty & \lambda & \lambda & 0 & 0 & 0 \\ \lambda & \lambda + 2\mu_\infty & \lambda & 0 & 0 & 0 \\ \lambda & \lambda & \lambda + 2\mu_\infty & 0 & 0 & 0 \\ 0 & 0 & 0 & 2\mu_\infty & 0 & 0 \\ 0 & 0 & 0 & 0 & 2\mu_\infty & 0 \\ 0 & 0 & 0 & 0 & 0 & 2\mu_\infty \end{bmatrix} \underline{\varepsilon}^{n+1} \tag{22}$$

$$= \begin{bmatrix} 2\mu_\infty \varepsilon_{11}^{n+1} + \lambda(\varepsilon_{11}^{n+1} + \varepsilon_{22}^{n+1} + \varepsilon_{33}^{n+1}) \\ 2\mu_\infty \varepsilon_{22}^{n+1} + \lambda(\varepsilon_{11}^{n+1} + \varepsilon_{22}^{n+1} + \varepsilon_{33}^{n+1}) \\ 2\mu_\infty \varepsilon_{33}^{n+1} + \lambda(\varepsilon_{11}^{n+1} + \varepsilon_{22}^{n+1} + \varepsilon_{33}^{n+1}) \\ 2\mu_\infty \varepsilon_{12}^{n+1} \\ 2\mu_\infty \varepsilon_{23}^{n+1} \\ 2\mu_\infty \varepsilon_{13}^{n+1} \end{bmatrix}$$

$$= \begin{bmatrix} 2\mu_\infty \varepsilon_{11}^{n+1} + \lambda \varepsilon_V^{n+1} \\ 2\mu_\infty \varepsilon_{22}^{n+1} + \lambda \varepsilon_V^{n+1} \\ 2\mu_\infty \varepsilon_{33}^{n+1} + \lambda \varepsilon_V^{n+1} \\ 2\mu_\infty \varepsilon_{12}^{n+1} \\ 2\mu_\infty \varepsilon_{23}^{n+1} \\ 2\mu_\infty \varepsilon_{13}^{n+1} \end{bmatrix}$$

The last term in the Eq. (20) looks like this in the Voigt notation:

$$\bar{\bar{C}}^e \underline{\Delta \varepsilon} - K_\infty \Delta \varepsilon_V \underline{1} = \begin{bmatrix} 2\mu_\infty \Delta \varepsilon_{11} + \lambda \Delta \varepsilon_V \\ 2\mu_\infty \Delta \varepsilon_{22} + \lambda \Delta \varepsilon_V \\ 2\mu_\infty \Delta \varepsilon_{33} + \lambda \Delta \varepsilon_V \\ 2\mu_\infty \Delta \varepsilon_{12} \\ 2\mu_\infty \Delta \varepsilon_{23} \\ 2\mu_\infty \Delta \varepsilon_{13} \end{bmatrix} - K_\infty \begin{bmatrix} \Delta \varepsilon_V \\ \Delta \varepsilon_V \\ \Delta \varepsilon_V \\ 0 \\ 0 \\ 0 \end{bmatrix} \quad (23)$$

Substituting Eq. (23) into (19) gives

$$\underline{h}_j^{n+1} = \exp\left(-\frac{\Delta t}{\tau_j}\right) \begin{bmatrix} h_{j,11}^n \\ h_{j,22}^n \\ h_{j,33}^n \\ h_{j,12}^n \\ h_{j,23}^n \\ h_{j,13}^n \end{bmatrix} + \gamma_j \frac{1 - \exp\left(-\frac{\Delta t}{\tau_j}\right)}{\frac{\Delta t}{\tau_j}} \begin{bmatrix} 2\mu_\infty \Delta \varepsilon_{11} + (\lambda - K_\infty) \Delta \varepsilon_V \\ 2\mu_\infty \Delta \varepsilon_{22} + (\lambda - K_\infty) \Delta \varepsilon_V \\ 2\mu_\infty \Delta \varepsilon_{33} + (\lambda - K_\infty) \Delta \varepsilon_V \\ 2\mu_\infty \Delta \varepsilon_{12} \\ 2\mu_\infty \Delta \varepsilon_{23} \\ 2\mu_\infty \Delta \varepsilon_{13} \end{bmatrix} \quad (24)$$

The above equations were transferred to a FORTRAN subroutine. The parameters required for the viscoelastic material law coded in the material card are  $\mu_0$  instantaneous shear modulus;  $\mu_j, \tau_j$  shear modulus and shear relaxation time for the  $j^{\text{th}}$  branch of the generalized Maxwell element;  $K_0$  instantaneous bulk modulus;  $K_j, \kappa_j$  bulk modulus and bulk relaxation time of the  $j^{\text{th}}$  branch of the generalized Maxwell element.

## 4.2 Implementation of plastic constitutive equation

In terms of incremental stress updates used by typical FEA codes, the viscoelastic stress result is the predictor stress or trial stress and now the plastic corrector step needs to be added if the yield limit is exceeded.

The formulation was based on isotropic Von-Mises yield function to calculate the effective stress from the stress state.

$$\bar{\sigma} = \sqrt{\frac{1}{2} [(\sigma_{11} - \sigma_{22})^2 + (\sigma_{22} - \sigma_{33})^2 + (\sigma_{33} - \sigma_{11})^2 + 6(\sigma_{12}^2 + \sigma_{23}^2 + \sigma_{13}^2)]} \quad (25)$$

The flow stress used in the formulation was based on Johnson-Cook flow stress model, given in Eq. (7), (8) and (9).

The yield function represented by Eq. (25) can be written as:

$$\phi(\bar{\sigma}, \bar{\varepsilon}^P, \dot{\varepsilon}, T) = \bar{\sigma}(\underline{\sigma}, T) - H(\bar{\varepsilon}^P, \dot{\varepsilon}, T) = 0 \quad (26)$$

where  $H$  is the hardening rule defined by Eq. (7).  $T$  is the temperature during the thermal time step.

The equations used for iteratively integrating the plastic constitutive equations for rate and temperature dependent plasticity with associated flow rule are:

$$\text{Associative flow rule: } \dot{\varepsilon}^P = \dot{\lambda} \frac{d\phi}{d\underline{\sigma}} \quad (27)$$

$$\text{Yield Function: } \phi \leq 0 \quad (28)$$

$$\text{Normality parameter: } \dot{\lambda} \geq 0 \quad (29)$$

$$\text{Kuhn-Tucker condition: } \dot{\lambda} \phi = 0 \quad (30)$$

$$\text{Consistency condition: } \dot{\lambda} \dot{\phi} = 0 \quad (31)$$

where  $\dot{\lambda}$  is the plastic multiplier.

## 4.3 Material card inputs and outputs

### 4.3.1 Inputs:

The inputs provided to the material card through the LS-DYNA keyword file contain the material properties and model fitting values for curing kinetics model, viscoelastic model and plastic model. There are some dummy variables left in the keyword input for further development of material card and integration of thermal expansion and shrinkage in the adhesive.

<b>Card 1</b>	1	2	3	4	5	6	7	8
<b>Variable</b>	MID	RO	MT	LMC	NHV	IORTHO	IBULK	IG
<b>Type</b>	A8	F	I	I	I	I	I	I

<b>Card 2</b>	1	2	3	4	5	6	7	8
<b>Variable</b>	IVECT	IFAIL	ITHERM	IHYPER	IEOS	LMCA		
<b>Type</b>	I	I	I	I	I	I		

<b>LMC Card</b>	CM1	CM2	CM3	CM4	CM5	CM6	CM7	CM8
<b>Card 3</b>	1	2	3	4	5	6	7	8
<b>Variable</b>	EALPHA	AALPHA	K1	K2	M	N	D	ALPHAC
<b>Type</b>	F	F	F	F	F	F	F	F

<b>LMC Card</b>	CM9	CM10	CM11	CM12	CM13	CM14	CM15	CM16
<b>Card 4</b>	1	2	3	4	5	6	7	8
<b>Variable</b>	IDOC	TMSCL	ALPHATH	EPSSH	TREF	R	TGO	TGINF
<b>Type</b>	F	F	F	F	F	F	F	F

<b>LMC Card</b>	CM17	CM18	CM19	CM20	CM21	CM22	CM23	CM24
<b>Card 5</b>	1	2	3	4	5	6	7	8
<b>Variable</b>	LAMBDA	AGEL	KINFO	NMAXW	PLON			
<b>Type</b>	F	F	F	F	F			

<i>LMC Card</i>	<i>CM25</i>	<i>CM26</i>	<i>CM27</i>	<i>CM28</i>	<i>CM29</i>	<i>CM30</i>	<i>CM31</i>	<i>CM32</i>
<i>Card 6</i>	1	2	3	4	5	6	7	8
<i>Variable</i>	<i>GFC</i>	<i>BULKFC</i>	<i>WLFTONLY</i>	<i>WLFT</i>	<i>C1</i>	<i>C2</i>	<i>C3</i>	<i>C4</i>
<i>Type</i>	<i>F</i>	<i>F</i>	<i>F</i>	<i>F</i>	<i>F</i>	<i>F</i>	<i>F</i>	<i>F</i>

<i>LMC Card</i>	<i>CM33</i>	<i>CM34</i>	<i>CM35</i>	<i>CM36</i>	<i>CM37</i>	<i>CM38</i>	<i>CM39</i>	<i>CM40</i>
<i>Card 7</i>	1	2	3	4	5	6	7	8
<i>Variable</i>	<i>AJC</i>	<i>BJC</i>	<i>NJC</i>	<i>TOJC</i>	<i>TMJC</i>	<i>MJC</i>	<i>CJC</i>	<i>EPDOTREF</i>
<i>Type</i>	<i>F</i>							

<i>LMC Card</i>	<i>CM41</i>	<i>CM42</i>	<i>CM43</i>	<i>CM44</i>	<i>CM45</i>	<i>CM46</i>	<i>CM47</i>	<i>CM48</i>
<i>Card 8</i>	1	2	3	4	5	6	7	8
<i>Variable</i>								
<i>Type</i>								

**LMCA Card**      Repeat the card based on the number of branches in Maxwell model ( max 20 branches)

<i>Card 7</i>	1	2	3	4	5	6	7	8
<i>Variable</i>	<i>Muj</i>	<i>TAUj</i>	<i>Kj</i>	<i>KAPj</i>	<i>Muj+1</i>	<i>TAUj+1</i>	<i>Kj+1</i>	<i>KAPj+1</i>
<i>Type</i>	<i>F</i>	<i>F</i>	<i>F</i>	<i>F</i>	<i>F</i>	<i>F</i>	<i>F</i>	<i>F</i>

### **List of Variables**

MID            Material Identification Number

RO            Mass Density

MT            Material Card Number (UMAT 44)

LMC            Number of material constants (40)

NHV            Number of History variables; 30 + (NMAXW x 7)

IORTHO       Orthotropic flag (0)

IBULK	Address of bulk modulus in material constants array (26)
IG	Address of shear modulus in material constants array (25)
IVECT	Vectorization flag (0)
IFAIL	Failure flag (0)
ITHERM	Temperature flag (on = 1), compute element temperature
IHYPER	Deformation gradient flag (0)
IEOS	Equation of State (0)
LMCA	Number of additional material constants (64)
EALPHA	Curing Kinetics Model; Activation Energy
AALPHA	Curing Kinetics Model; Pre-exponential Factor
K1	Curing Kinetics Model; K1
K2	Curing Kinetics Model; K2
M	Curing Kinetics Model; M
N	Curing Kinetics Model; N
D	Curing Kinetics Model; Diffusion Parameter (0 for the current calibration)
ALPHAC	Curing Kinetics Model; Diffusion Parameter (0 for the current calibration)
IDOC	Curing Kinetics Model; Initial Degree of Cure

TMSCL	Time Scale factor for the simulation
ALPHATH	Coefficient of thermal expansion for the adhesive
EPSSH	Coefficient of shrinkage for the adhesive
TREF	Reference Temperature for shrinkage and thermal strains
R	Universal gas constant
TG0	DiBenedetto equation: Glass transition temperature for uncured adhesive
TGINF	DiBenedetto equation: Glass transition temperature for fully cured
LAMBDA	DiBenedetto equation: lambda
AGEL	Cure level at start of gelification
KINFO	Long term bulk modulus at uncured state
NMAXW	Number of Maxwell branches
PLON	0 - Plastic model off; 1- Plastic model on
GFC	Instantaneous shear modulus at full cure state
BULKFC	Instantaneous bulk modulus at full cure state
WLFTONLY	1 - For using only WLF shift function and a reference temperature WLFT; 0 - For using WLF shift function for T>Tg and coded function for T<Tg.
WLFT	WLF Shift function: Reference temperature

C1	WLF Shift function: Parameter A
C2	WLF Shift function: Parameter B
C3	Shift function: Parameter C (0 for the current calibration)
C4	Shift function: Parameter D (0 for the current calibration)
AJC	Plastic Model (Johnson Cook Flow stress model): A
BJC	Plastic Model (Johnson Cook Flow stress model): B
NJC	Plastic Model (Johnson Cook Flow stress model): N
T0JC	Plastic Model (Johnson Cook Flow stress model): T <sub>0</sub>
TMJC	Plastic Model (Johnson Cook Flow stress model): T <sub>m</sub>
MJC	Plastic Model (Johnson Cook Flow stress model): m
CJC	Plastic Model (Johnson Cook Flow stress model): C
EPDOTREF	Plastic Model (Johnson Cook Flow stress model): Reference strain rate, $\dot{\epsilon}$
MUj	Maxwell Model: Shear relaxation modulus for 1st branch
TAUj	Maxwell Model: Shear decay time for 1st branch
Kj	Maxwell Model: Bulk relaxation modulus for 1st branch
KAPj	Maxwell Model: Bulk decay time for 1st branch
MUj+1	Maxwell Model: Shear relaxation modulus for 2nd branch

TAUj+1	Maxwell Model: Shear decay time for 2nd branch
Kj+1	Maxwell Model: Bulk relaxation modulus for 2nd branch
KAPj+1	Maxwell Model: Bulk decay time for 2nd branch

### 4.3.2 Outputs:

The material card allows to output several parameters in the d3plot file in LS-DYNA as history variables. The history variables serve several purposes. They are primarily used to carry over the values of stress, strain or any other internal variables from a time step to the next. The history variables can initially be used to debug the material card and later used to obtain the output parameters from the material card. The history variables used in the material card are listed below:

HISV (1)	Equivalent Plastic Strain
HISV(2)	Hydrostatic Pressure, $p = (\text{sig xx} + \text{sig yy} + \text{sig zz}) / 3$
HISV(5-10)	Fluid Strain, 11,22,33,12,23,13
HISV (11-16)	Elastic Strain, 11,22,33,12,23,13
HISV (17)	Scaled Time, truedt
HISV (18)	Temperature
HISV (19)	Degree of cure, alpha
HISV (20)	Rate of cure, dalpha
HISV (31-37)	For first Maxwell branch, Six state variables $h_j$ (11,22,33,12,23,13), $v_j$
HISV (38-44)	For second Maxwell branch, Six state variables $h_j$ (11,22,33,12,23,13), $v_j$
HISV (45-51)	So on..

## **4.4 Material Card Verification:**

The material card was tested and debugged on simple single element models. The approach of using a single element was used to eliminate the effects of other parameters and isolate the performance of the individual modules.

### **4.4.1 Verification of curing kinetics model**

The curing kinetics model was tested on a single solid element model. The element was modeled to go from a temperature of 100°C to 250°C at three different heating rates (2°C/min, 5°C/min and 10°C/min). The initial degree of cure for the element (IDOC) was set to 0. The FE simulation captured the curing of the solid element as the temperature rose with time. The degree of cure vs. time saved in the finite element output history variable 19, was extracted for comparison. It was compared to mathematically calculated degree of cure vs. time obtained by integrating the curing kinetics equation for the same temperature vs. time history. The finite element results were an exact match with the mathematical results as shown in *Figure 4.2*.

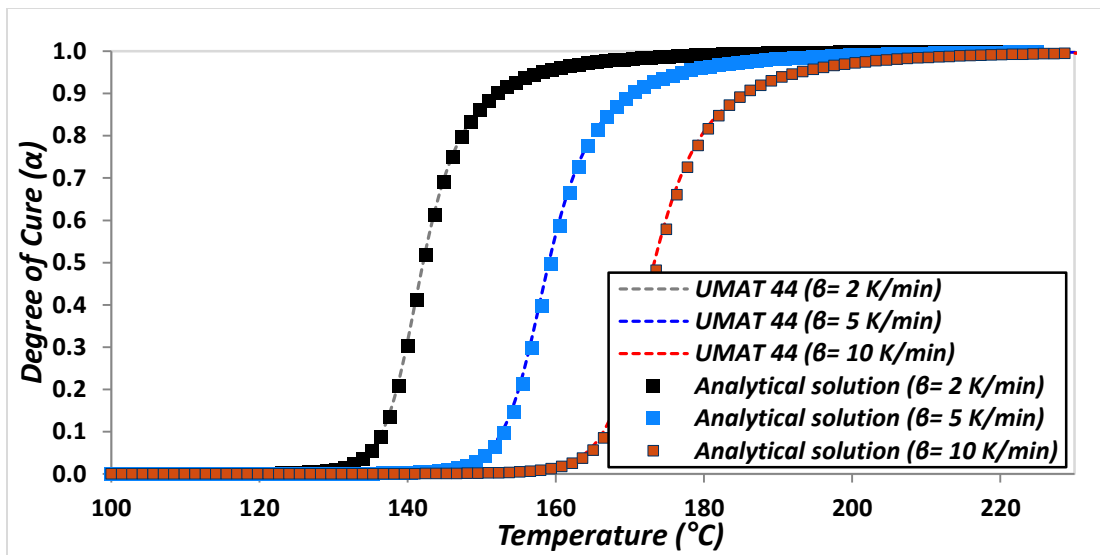


Figure 4.2 FE model results vs. mathematically calculated results for degree of cure

#### 4.4.2 Verification of viscoelastic model

The viscoelastic model was also verified using a single element model for a variety of scenarios. The material card was used with the plastic model turned off (PLON = 0 in the keyword file) to isolate the viscoelastic behavior. For a strain of 10%, the stress response was extracted as an output from the LS-DYNA model. The stress vs. time and strain were used to calculate the modulus vs. time. The model was tested for different temperatures. The modulus relaxation curves obtained from the FE model at different temperatures were compared to the shifted master curves at the modeled temperatures and a good fit was found as shown in *Figure 4.3*.

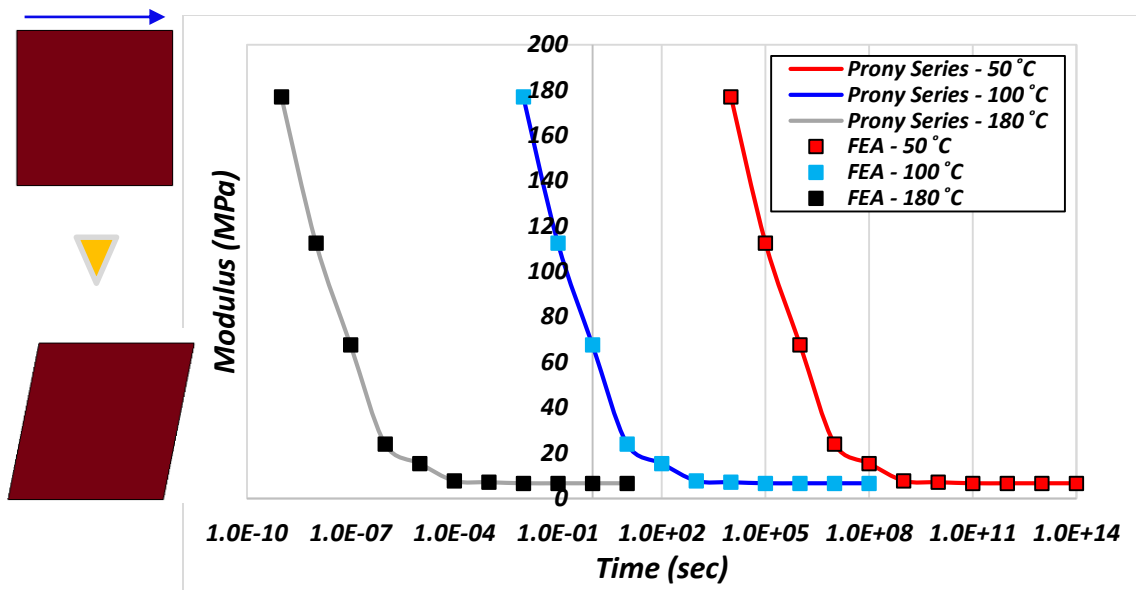
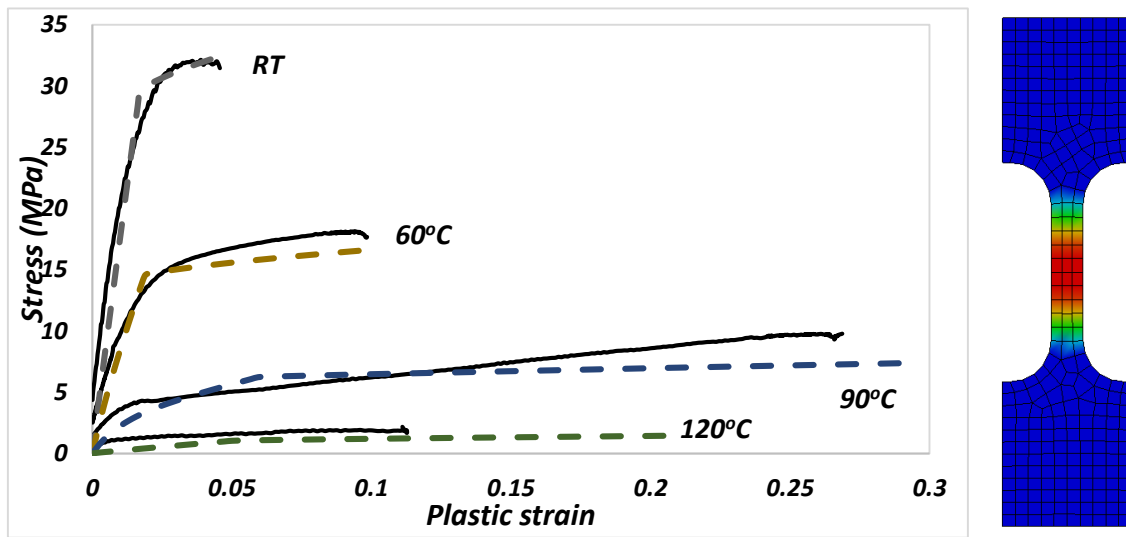


Figure 4.3 Single Element FE model; Comparison of FE model results vs. Prony series expansion

#### 4.4.3 Verification of viscoelastic-plastic coupled model

The verification of the coupled response of viscoelastic-plastic model was performed on a finite element simulation on tensile specimen geometry. The material card was used with plastic model turned on (PLON = 1) in order to get a combined response of viscoelastic and plastic models. The simulations were run for a fully cured adhesive at 20°C, 60°C, 90°C, 120°C at a constant strain rate of 0.001/s. The predictions from the finite element model were in very good agreement with the experimental stress-strain curves. The slopes of the curve in the beginning, determined by the viscoelastic model match the experimental curves at a good level. Although the viscoelastic model was calibrated using DMA data acquired in shear deformation mode, the predicted modulus values in tensile mode are in agreement with the young's modulus values obtained from the tensile tests.

The yield values and the trend of the plastic curves at different temperatures matched with the experimental tensile curves, as shown in *Figure 4.4*.



*Figure 4.4 Viscoelastic-plastic model performance in FE simulation (dashed lines) vs. experimental stress-strain curves (solid lines); Geometry used for FE simulation*

This was an assurance that the modeling approach was reliable and could be trusted for more complex simulations.

# **Chapter 5**

## **5. FINITE ELEMENT SIMULATIONS AND MODEL VALIDATION**

### **5.1 Experiments for model validation at coupon level:**

The experiments discussed in the chapter 2 were used to validate the adhesive material models developed for Henkel adhesive EP 5089. A special setup was built to allow curing of an adhesive bonded single lap shear joint specimen in the furnace, while the thermal displacements were being recorded using optical measurement technique – digital image correlation.

There were three main outcomes of the experiments: (i) Y-Displacement across the joint, which is a measure of the increasing overlap area due to thermal expansion in the heating phase of the temperature cycle. (ii) Z-Displacement across the joint, which is a measure of the bending/distortion in the structure due to restriction in the contraction of the

substrates in the cooling phase of the temperature cycle. (iii) Force applied by the adhesive bond to restrict the contraction in the substrates in the cooling phase, which is also responsible for the setting of residual stresses in the adhesive. The three output parameters for the two sets of experiments: (i) DP980-AA7071 and (ii) AA7071-AA7071 were used to validate the adhesive material models.

### **5.1.1 Finite element model:**

#### **5.1.1.1 Model geometry:**

Two simulation models were built in LS-DYNA to perform the experimental validation based on the experimental setup and two different substrate combinations: a multi-material combination of DP980 steel - AA7071 and a similar material combination of AA7071-AA7071. The simulation models consisted of six parts: Top and bottom grip rods made of Nickel-Iron (INVAR) alloy, top and bottom metal substrates (DP980-AA7071 or AA7071-AA7071), solid adhesive elements, and a top substrate spacer. The specimen dimensions were based on the experimental as shown in *Figure 5.1*. The substrates were 100 mm long and 20 mm wide. The overlap length of the single lap shear joint was 20 mm. The thickness of the DP980 steel was 1.42 mm, and the thickness of AA7071 substrate was 2.55 mm. Three simulations with varying adhesive bond thickness were done for each of the two substrate combinations to compare the effects of adhesive bondline thickness on the simulation results. A picture of the complete model geometry with the dimensions of the grip rods and temperature regions is shown in *Figure 5.2*.

### **5.1.1.2 Boundary conditions**

The grip rods were constrained at the top and bottom by fixing all six degrees of freedom.

The experimentally obtained temperature profiles for the full baking cycle recorded for each test [Akshat et al., 2019] from the four thermocouples were fed to the four regions of the simulation model as shown in *Figure 5.2*. The parts of the top and bottom grip outside the furnace were given a temperature of 25°C. The actual duration of the temperature cycle was 12000 seconds (2400 seconds of heating followed by cooling phase) which was too long and computationally expensive with the typical time steps used for the solid adhesive mesh of size 1 mm. After a time scaling analysis, the simulation was time scaled by 1000x and the termination time was set to 12 seconds as a compromise between the prediction accuracy and computation speed.

### **5.1.1.3 Model parameters**

Solid elements were used for modeling the grip rods, substrates and adhesive bead. The metal substrates and grip rods were modeled using the material model \*MAT\_ELASTIC\_PLASTIC\_THERMAL which takes temperature dependent properties of the material including coefficient of thermal expansion. The thermal material card used for the substrates, grips and adhesive was \*MAT\_THERMAL\_ISOTROPIC\_TD\_LC in LS-DYNA which takes the values for conductivity and specific heat capacity as a function of temperature. The material properties for the two substrate materials were obtained from tensile tests performed at room temperature and high temperature and are given in *Table 5.1*.

The adhesive material models developed in section 2 and 3 were adjusted to the coded material card MAT\_ADHESIVE\_CURING\_VISCOELASTIC in LS-DYNA. A layer of null shell elements \*MAT\_NULL was used between the solid adhesive elements and the substrates to avoid negative volume errors. The adhesive elements were tied to the substrates using \*CONTACT\_TIED\_SURFACE\_TO\_SURFACE contact definition in LS-DYNA.

<b>Property</b>	<b>DP980 (@25°C - @200°C)</b>	<b>AA7071 (@25°C - @200°C)</b>	<b>INVAR (@25°C - @200°C)</b>
<b>E</b>	204 GPa – 196 GPa	64 GPa – 52 GPa	137 GPa – 126 GPa
<b>Yield Strength</b>	650 MPa – 550 MPa	405 MPa – 256 MPa	725 MPa – 650 MPa
<b>CTE</b>	1.15E-5 – 1.15E-5	2.18E-5 – 2.18E-5	2.0E-6 – 2.0E-6
<b>Density</b>	7.87 g/cm <sup>3</sup>	2.7 g/cm <sup>3</sup>	8.2 g/cm <sup>3</sup>
<b>Poisson's Ratio</b>	0.28	0.33	0.30

Table 5.1 Material properties for substrates and INVAR grips used in the FE model

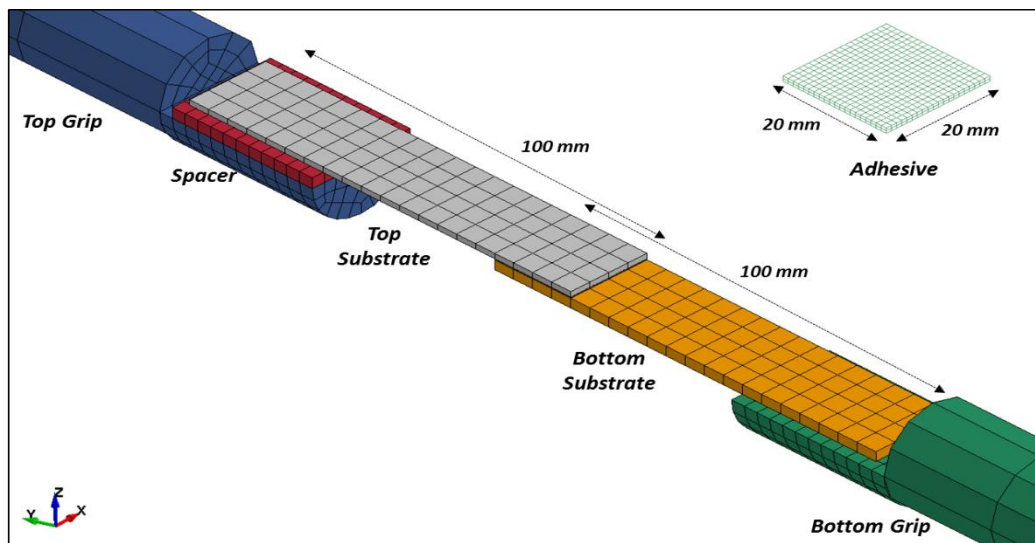
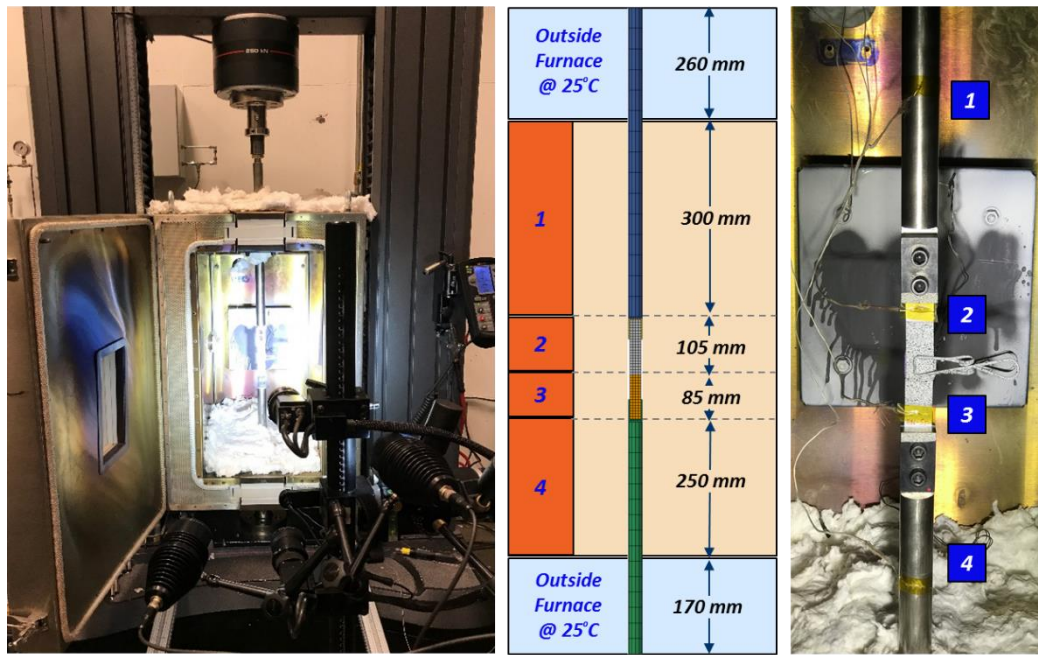


Figure 5.1 Lap shear joint geometry used for the experiments and FE model



*Figure 5.2 Experimental setup; finite element model with 4 temperature regions carrying different temperature profiles; four thermocouple positioned on the grip rods and substrates*

### 5.1.2 Comparison of FE and experimental results

For the purpose of comparison, the relative displacements in Y and Z direction on a 30 mm gauge length across the joint (as shown in *Figure 5.3*) were obtained from the FE model. A cross section was defined on the top grip in the simulation model and the force through the cross section was recorded for comparing with the experimentally obtained values.

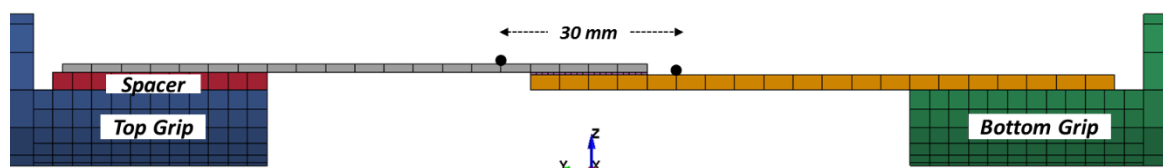


*Figure 5.3 FE model showing 30 mm extensometer across the joint*

### **5.1.2.1 Multi-material bond of DP980-AA7071**

A comparison of the Y-displacement, Z-displacement and force for DP980-AA7071 simulation models for varying thickness as compared to experimental data is shown in *Figure 5.4, 5.5, and 5.6.*

During the heating phase of the temperature cycle, the grips and the substrates expand and move relatively closer to each other therefore giving a negative Delta-Y across the joint as seen in *Figure 5.4*. During the temperature ramp, the adhesive is in an uncured liquid state and does not show any restriction to the thermal expansion of substrates which is in agreement with the initial zero force values in *Figure 5.6*. At around 1800 seconds, as the adhesive slowly cures and reaches the gelification point, the partially cured adhesive starts opposing any further expansion in the substrates and in turn picks up negative forces. At 2400 seconds, when the cooling cycle starts, the substrates begin to contract and move away from each other, showing a positive relative displacement across the joint. At this point, now fully cured adhesive restricts the thermal contraction in the substrates and in turn pick up positive forces as shown in *Figure 5.6*. As a consequence, the substrates do not return to their initial position generating a distortion in the geometry and bending across the joint giving a residual Delta-Y and Delta-Z at the end of the cooling cycle as shown in *Figure 5.4, 5.5*. The force applied by the adhesive bond gives rise to residual stresses in the adhesive.

The model prediction for Y-displacement, Z-displacement and force is in good agreement with the experimentally obtained data. As per *Figure 5.4*, the FE results for 0.30 mm thick adhesive show a delta-Y of -0.25 mm against the DIC obtained value of -0.30 mm. *Figure 5.5* shows an estimated delta-Z value of -1.05 mm against the experimental value of -1.10 mm. *Figure 5.6* shows a very close estimation of final force value of ~4000 N at the end of the temperature cycle.

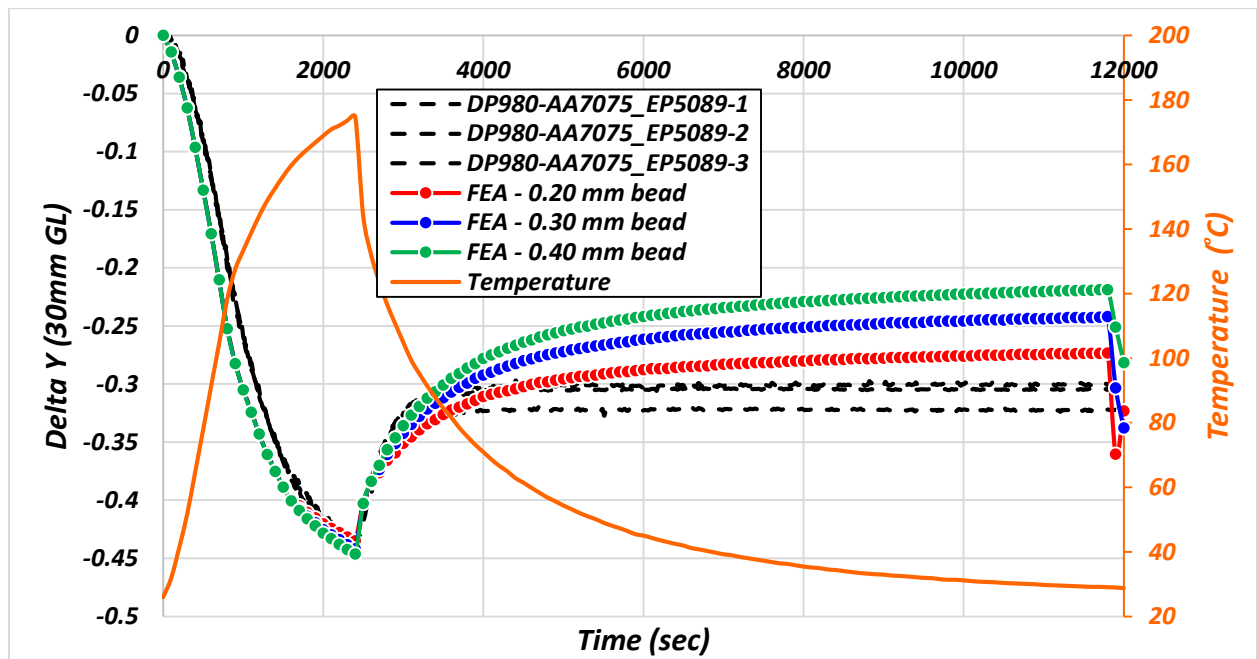


*Figure 5.4 Comparison of DIC measurements for Delta Y (30mm GL) vs. FE estimation for DP980-AA7075*

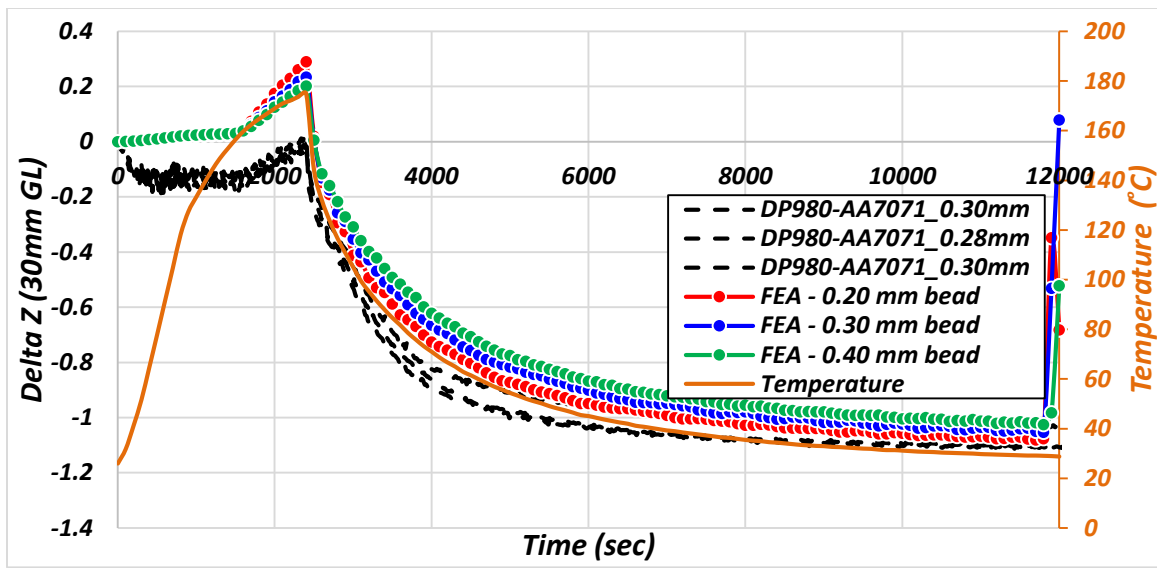


Figure 5.5 Comparison of DIC measurements for Delta Z (30mm GL) vs. FE estimation for DP980-AA7071

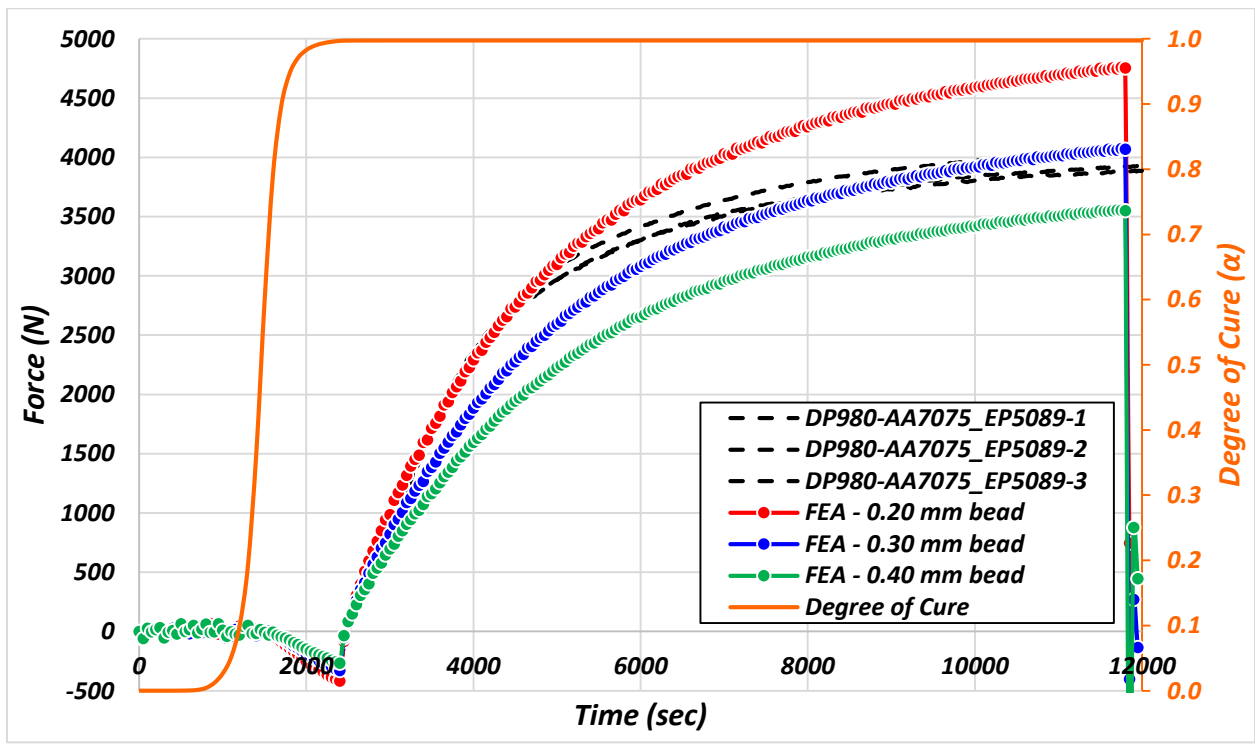
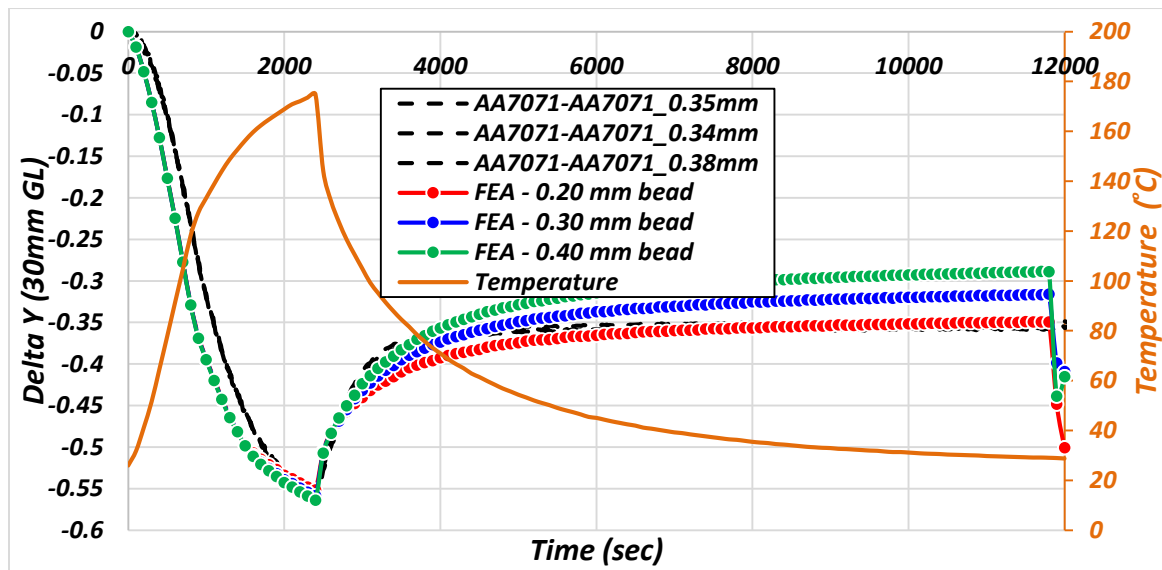


Figure 5.6 Comparison of experimentally measured force vs. FE estimation for DP980-AA7071

### 5.1.2.2 Similar material bond of AA7071-AA7071

A comparison of the Y-displacement for Z-displacement for AA7071-AA7071 simulation models for varying thickness as compared to experimental data is shown in *Figure 5.7, 22 and 23*. The relative displacement in the aluminum-aluminum joint is larger than the steel-aluminum joint owing to a higher CTE value for aluminum. The maximum delta-Y (at the peak temperature) is -0.56 mm for AA7071-AA7071 joint as compared to -0.45 mm for DP980-A7071 joint. A higher maximum relative displacement produces a higher residual delta-Y and delta-Z along with a higher force measurement. Another reason for a higher delta-Z value is a lower young's modulus value of AA7071 as compared to DP980 steel.



*Figure 5.7 Comparison of DIC measurements for Delta Y (30mm GL) vs. FE estimation for AA7071-AA7071*

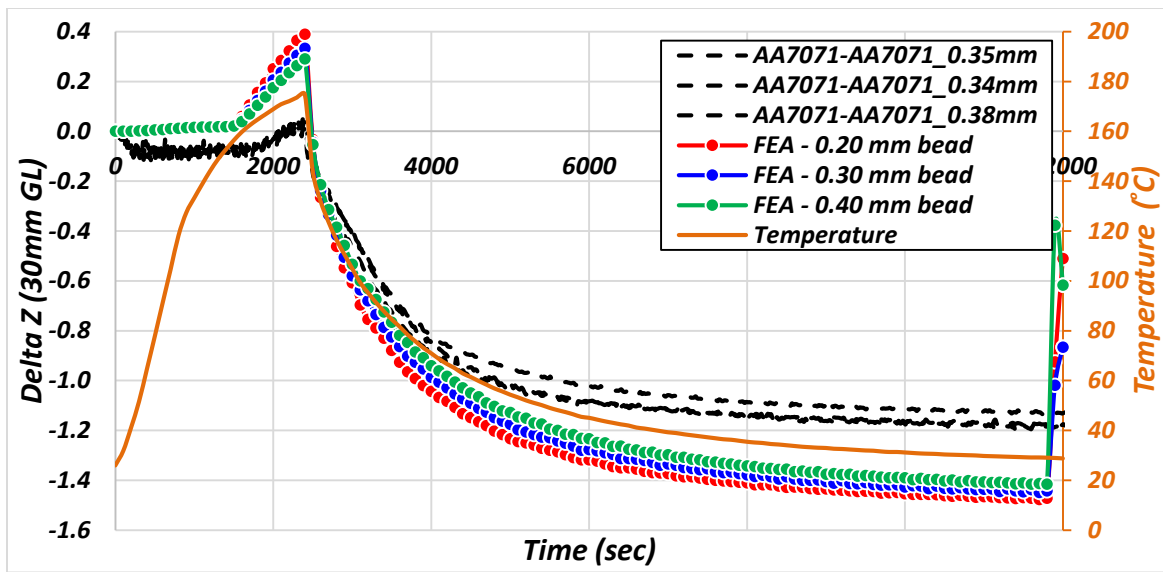


Figure 5.8 Comparison of DIC measurements for Delta Z (30mm GL) vs. FE estimation for AA7071-AA7071

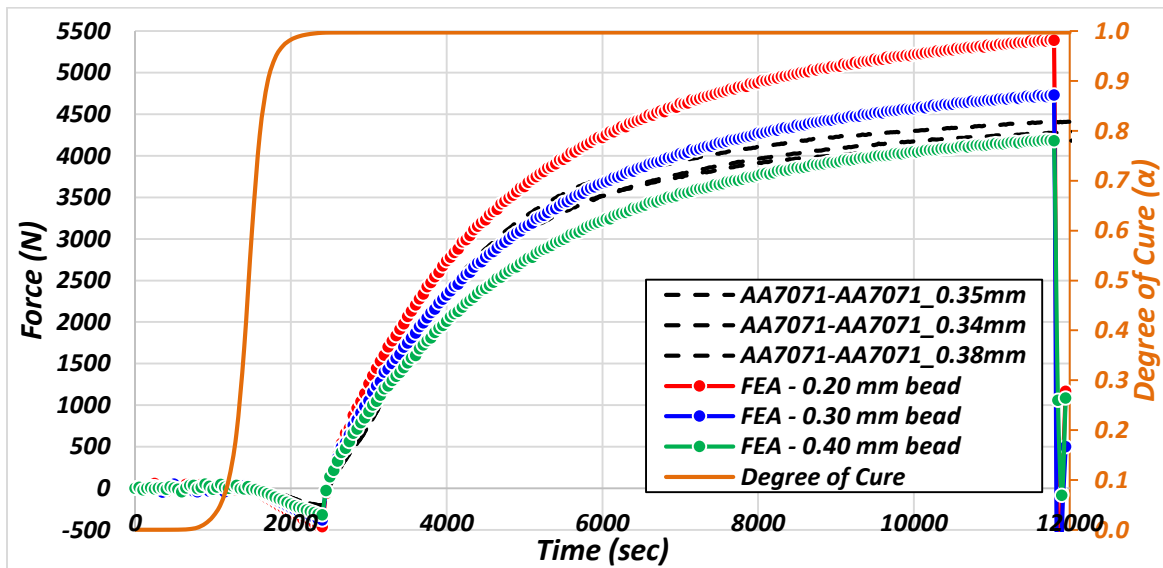


Figure 5.9 Comparison of experimentally measured force vs. FE estimation for AA7071-AA7071

The FE model prediction for Y-displacement, Z-displacement and force is in good agreement with the experimentally obtained data. As per Figure 5.7, the experimental

curves lie between the two FE generated curves for 0.30 mm thick adhesive and 0.40 mm thick adhesive show a delta-Y of approximately -0.35 mm. The model predicts a higher level of bending i.e. delta-Z across the joint as shown in *Figure 5.8*. *Figure 5.9* shows that an excellent prediction of force is obtained for AA7071-AA7071 bond with the experimental scatter lying between the predicted values for 0.30 mm and 0.40 mm thick adhesive i.e.  $\sim 4500$  N at the end of cooling cycle.

### 5.1.3 Computational results

The FE prediction for residual stress in the adhesive in different directions at a center element is shown in *Figure 5.10* and *Figure 5.11* for the two substrate combinations. The stresses are nearly zero in the beginning until it passes the point of gelification after approximately 1800 seconds. At the onset of gelification, a small shear stress in the YZ plane develops due to the relative displacement of the two substrates. Up to 2400 seconds, the stresses remain small because the stiffness of the adhesive is low at high temperatures even though it is already fully cured. Then the cooling phase starts and the displacement reverses its direction. The two substrates experience thermal contraction and start pulling each other through the adhesive layer, thereby inducing stresses in the adhesive. As a result, the shear stress changes its direction and the effective stress shows the corresponding deflection point. As the temperature of the system decreases, the stiffness of the adhesive increases and the residual stresses are set in the adhesive bond. The YZ-stress in the bond lies in the range of 10 MPa and the effective Von-Mises stress

reaches approximately 18 MPa. The stresses in the XY and ZX direction remain close to zero due to very small displacements in those directions.

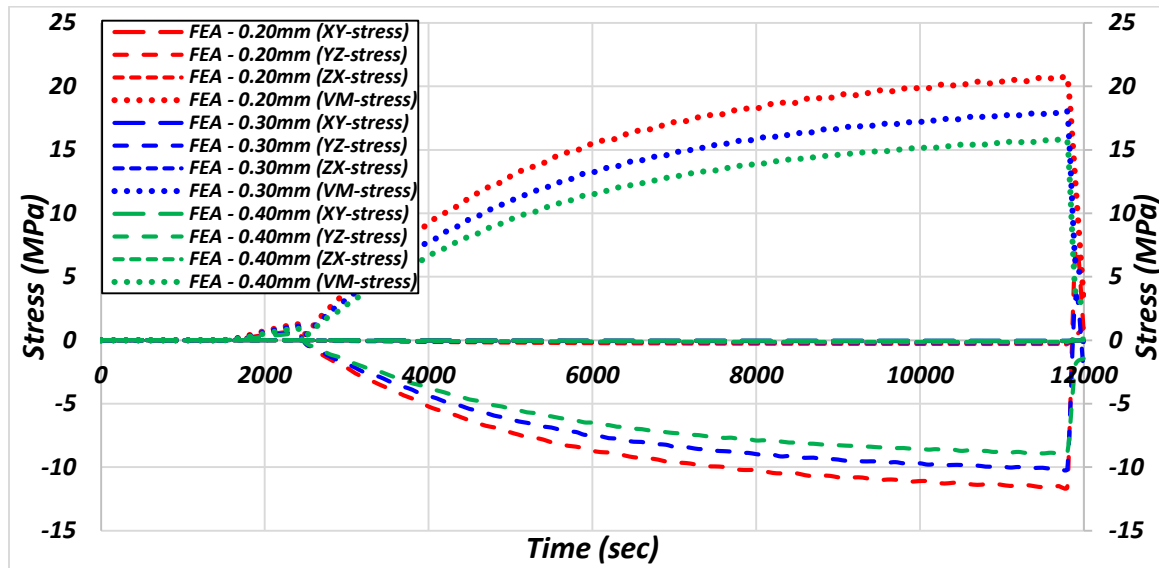


Figure 5.10 FE model prediction of residual stresses for 0.2 mm, 0.3 mm and 0.4 mm adhesive bead for DP980-AA7071

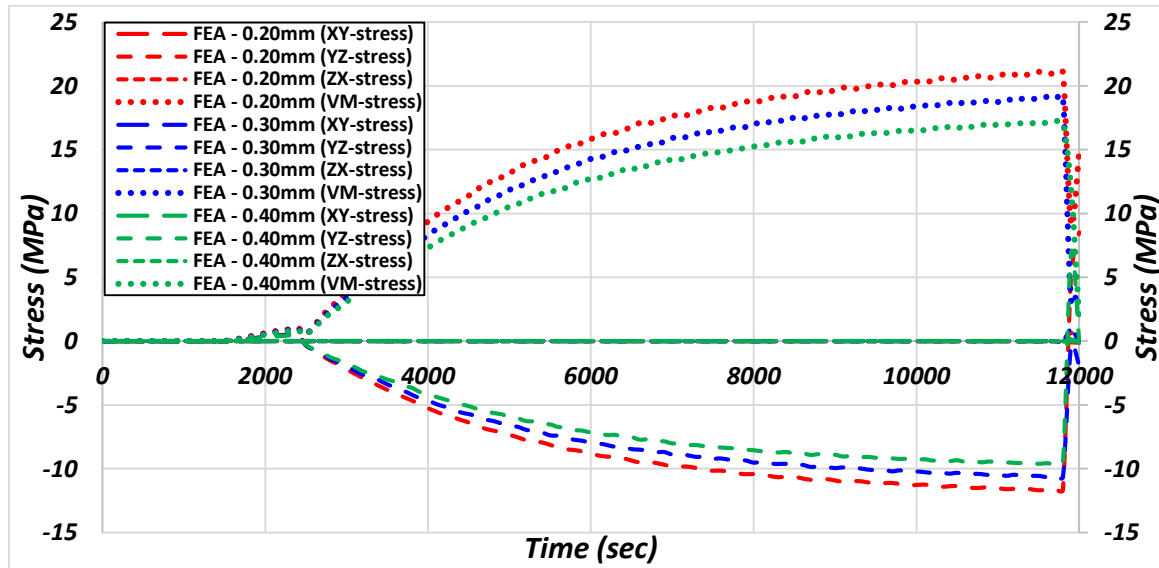


Figure 5.11 FE model prediction of residual stresses for 0.2 mm, 0.3 mm and 0.4 mm adhesive bead for AA7071-AA7071

The stress levels in the aluminum-aluminum joint show slightly higher values owing to higher thermal displacements in the aluminum substrate.

*Effect of thickness:* The finite element results for the different adhesive bead thicknesses show interesting results. With a decreasing adhesive thickness, the joint behaves stiffer, and as a result, produces greater residual displacement in delta-Y and delta-Z along with a higher force value. Subsequently, the adhesive bead thickness has an effect on the residual stresses in the adhesive bond. A contour plot of the effective stress in the adhesive bond with different thicknesses is shown in *Figure 5.12*.

#### **5.1.4 Concluding remarks**

This work developed a suite of models which work in conjunction to predict the manufacturing process induced effects on an adhesive joint. The models were calibrated for an automotive grade structural adhesive EP 5089 and the calibrated models were implemented into finite element simulations for two sets of substrates. The predicted results of the finite element simulations showed good agreement with the experimental results. The developed approach

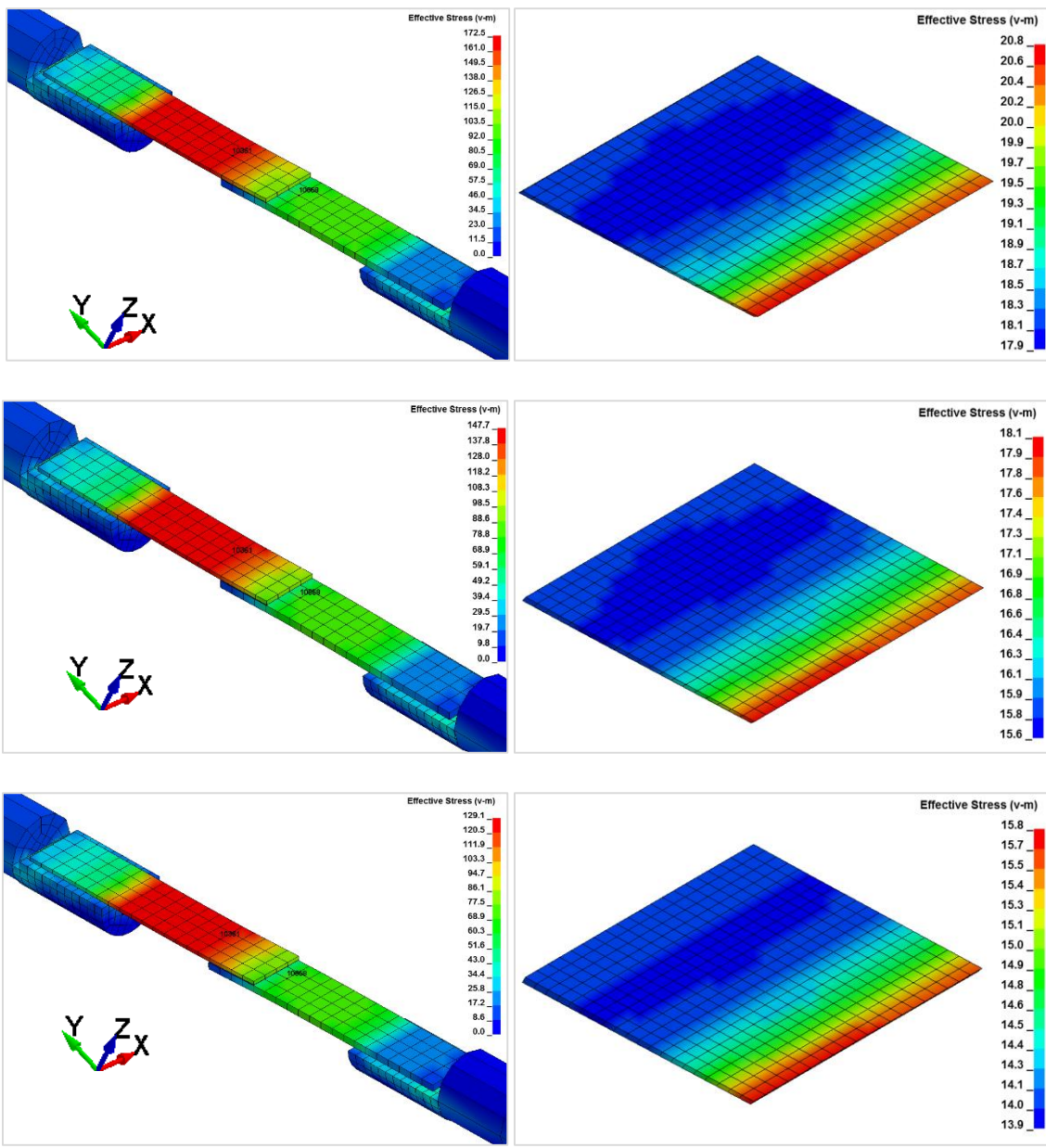


*Figure 5.12 FE predicted contour plots of effective stress in the substrates and residual stress in the adhesive for 0.2 mm, 0.3 mm and 0.4 mm adhesive bead (top to bottom) for DP980-AA7071*

based on only the viscoelastic modeling of adhesive gives satisfactory results at coupon level, and can be tested on a component or full vehicle level in the future.

## **5.2 Experiments for model validation at component level:**

The component level validation of the material model was done on the scaled-down roof component experiment, as discussed in the previous section.

### **5.2.1 Finite Element Model**

#### **5.2.1.1 Model Geometry:**

The validation was done using two models:

- Model I: With adhesive only
- Model II: With adhesive and mechanical fixations

***Model I (with adhesive only):*** The geometry of the finite element model was prepared identical to the test specimen with adhesive only. The steel frame was modeled by solid elements of size 5 mm. The thickness of the steel frame was 5 mm. The aluminum flat panel was modeled by shell elements of size 5 mm and the thickness of the panel was 1.10 mm. The adhesive was modeled by solid elements of size 2 mm and a bond thickness of 0.20 mm. The hard clamp in the top left of the test specimen was modeled using a single solid element in the FE model. The finite element model geometry is shown in *Figure 5.13.*

The top and bottom surfaces of the adhesive elements were tied to the interacting surfaces of the aluminum panel and steel frame using \*CONTACT\_TIED\_SURFACE\_TO\_SURFACE contact definition in LS-DYNA. The top and

bottom surfaces of the solid element were tied to the aluminum panel and steel frame, similar to the adhesive. The steel frame and the aluminum panel were modeled using the material model \*MAT\_ELASTIC\_PLASTIC\_THERMAL which takes temperature dependent properties of the material including coefficient of thermal expansion. The thermal material card used for the substrates, grips and adhesive was \*MAT\_THERMAL\_ISOTROPIC\_TD\_LC in LS-DYNA which takes the values for conductivity and specific heat capacity as a function of temperature. The material properties for the steel frame, aluminum panel and steel clamp were obtained from tensile tests performed at room temperature and the results are shown in *Figure 5.14*.

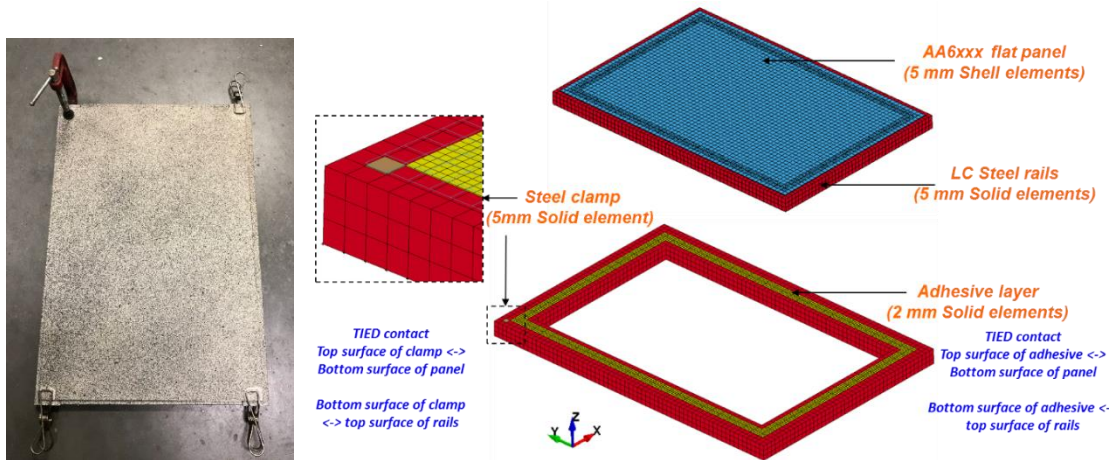


*Figure 5.13 Finite element model I with adhesive only, clamped on the top left corner*

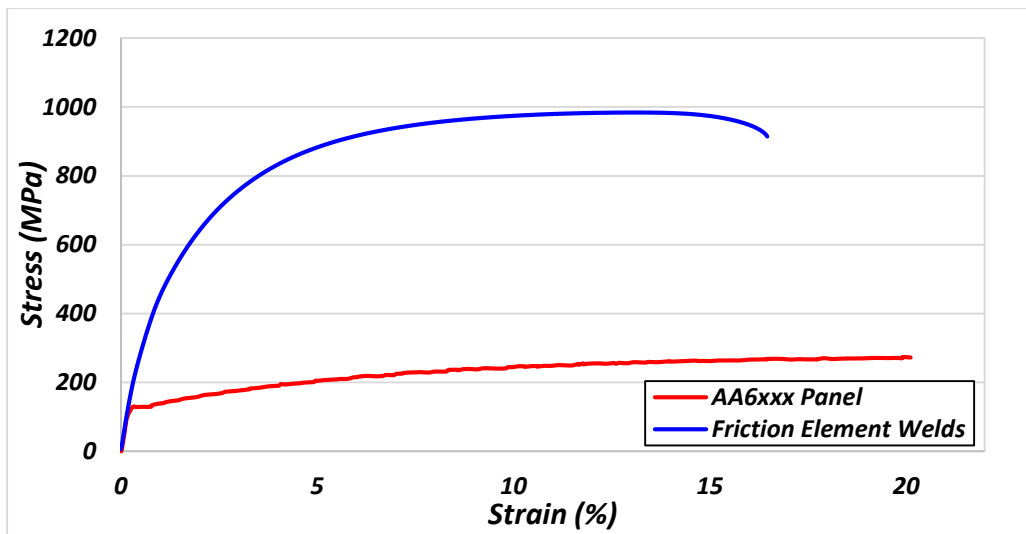
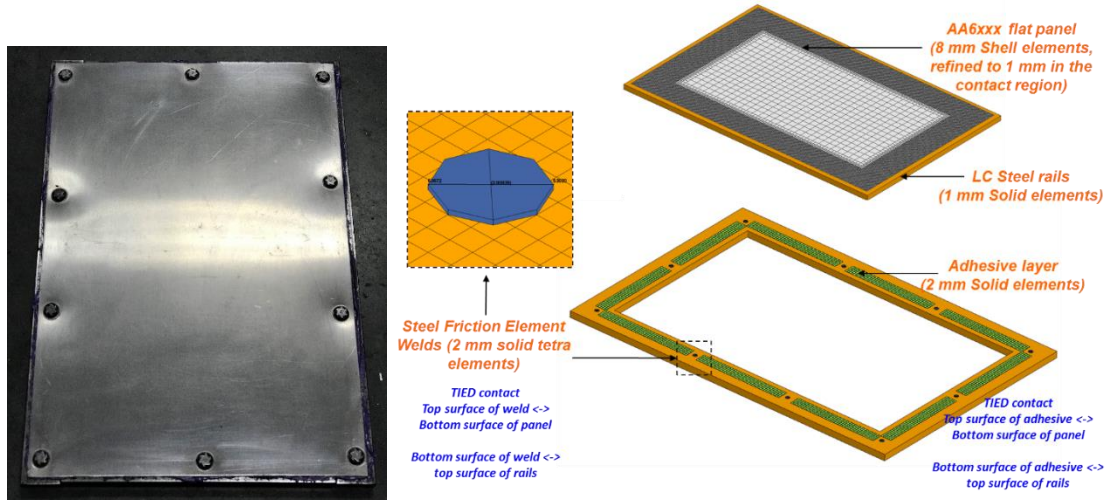


Figure 5.14 Material properties entered in FEA for aluminum panel and steel clamp and friction element welds

**Model II (with adhesive and mechanical fixation):** The geometry of the finite element model II was prepared identical to the test specimen with adhesive and mechanical fixations. The steel frame was modeled by solid elements of size 1 mm. The thickness of the steel frame was 5 mm. The aluminum flat panel was modeled by shell elements of size 8 mm, refined to 1 mm in the critical contact region and the thickness of the panel was 1.10 mm. The adhesive was modeled by solid elements of size 2 mm and a bond thickness of 0.20 mm. The top and bottom surfaces of the adhesive elements were tied to the interacting surfaces of the aluminum panel and steel frame using \*CONTACT\_TIED\_SURFACE\_TO\_SURFACE contact definition in LS-DYNA. The weld elements were modeled as octagonal solid geometries to replicate a circular weld of diameter 4 mm. The height of the weld element between the steel frame and aluminum

panel was 0.2 mm. The weld element top and bottom surfaces were tied to the top panel and bottom frame by TIED contact, similar to the adhesive elements. The weld elements were spaced at a gap of 100 mm from each other similar to the actual test specimen, as shown in *Figure 5.15*.



*Figure 5.15 Finite element model II with adhesive and mechanical fixations*

### 5.2.2. Comparison of FE predictions with experimental results

The displacements in the aluminum panel captured during the test were compared to the displacements predicted by the finite element model. The comparison was made based on the general trend of displacement contour in the panel and point displacements at the top left, top right, bottom left, bottom right and center point selected on the same location on the test specimen and the finite element model. The chosen point locations are shown in *Figure 5.16*.

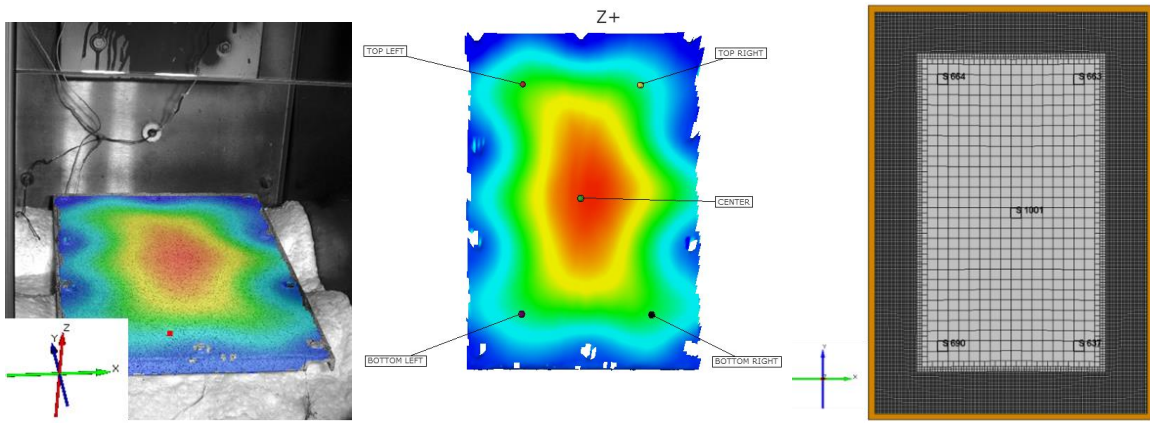


Figure 5.16 Points selected for comparison between the test and FE predictions

### 5.2.2.1 Model I (with adhesive only)

The finite element predictions and DIC generated displacements from the experiments are shown in *Figure 5.17, 5.18, and 5.19*. The displacements in the X, Y and Z direction are shown at the end of the heating phase and the cooling phase. As the temperature rises, the aluminum panel and the steel frame start expanding in the X and the Y direction. Since the adhesive is in the uncured state at the beginning of the test, the adhesive does not pose any restriction to the expansion across the adhesive bond. As a result, the aluminum panel expands freely in the X and Y direction. At the peak temperature, near the end of the heating phase, the adhesive gets fully cured and starts restricting any further movement across the joint. In the cooling phase, as the whole system starts to cool down, the aluminum panel and the steel frame start contracting to go back to their initial state. But, the fully cured adhesive puts restriction on the contraction of the panel and frame.

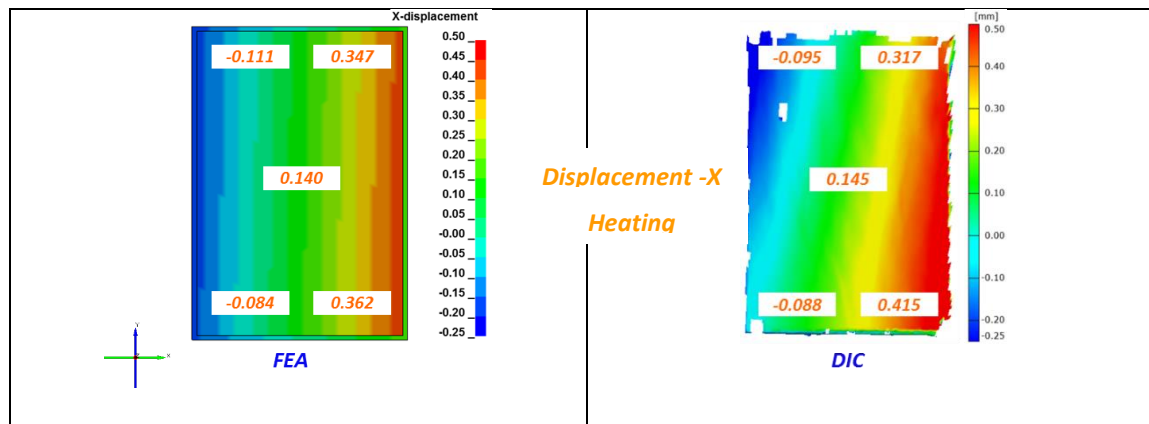
As a result, the panel and the steel frame go into an unintended distorted state. There is a residual displacement in the X and Y direction in the panel.

This behavior is well represented in the experiments as well as FE predictions. Having a hard constraint in the top left corner due to the clamp, the aluminum panel tends to expand more in the positive X direction and positive Y direction during the heating phase. At the end of the cooling phase, the magnitude of the displacements fall as a result of contraction, but there is a residual displacement due to the effect of adhesive. The trend in the displacements in the X and Y direction are similar for the experiments and finite element predictions. On comparing the point displacements, it was found that the values of Y-displacement in the experiments were found to be shifted. A small global movement in the whole test specimen inside the furnace may cause the displacements to drift in a certain direction. To remove this global movement, the displacements in Y-direction were shifted by 0.3 mm in the positive direction. The magnitude of relative point displacements after adjusting the DIC values matched the FE predictions to a good level.

An important thing to note here is that the experiments were run inside a convection furnace with DIC cameras looking through a glass window at a slanting angle. It was a challenge to get meaningful measurements in this scenario considering the difficulties in measurement due to heat waves inside the furnace and distortion due to glass between the test specimen and the cameras. Considering the discussed challenges, the trend in

the displacements in the experiments and finite element predictions have a good level of agreement.

The displacements in the Z-direction in this case are not much dependent on the adhesive behavior. The experiments show that the panel had a variation in the Z-contour, which is not predicted by the finite element model. This behavior can be explained by looking into the initial state of the aluminum panel. The aluminum panel was modeled as a perfectly flat sheet in finite element, which is not the case in the experiment. When a metal sheet is heated to a certain temperature, the internal stresses due to rolling are released and the minor distortions in the panel are observed. This phenomenon could not be captured in the finite element simulations. Under the light of these limitations, the finite element prediction of the displacements in the roof component with adhesive only shows an acceptable level of agreement with the experimental results.



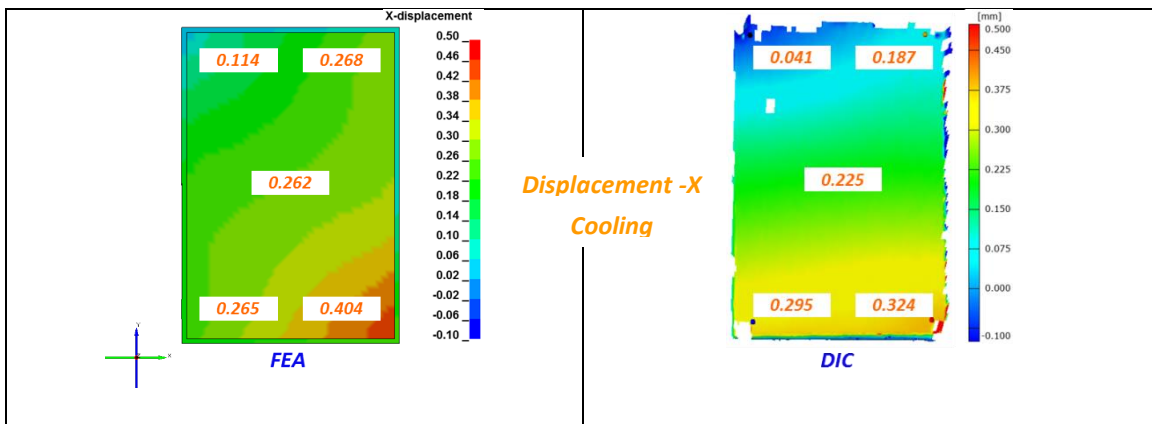


Figure 5.17 X-displacement prediction from finite element model vs. DIC generated values for Model I

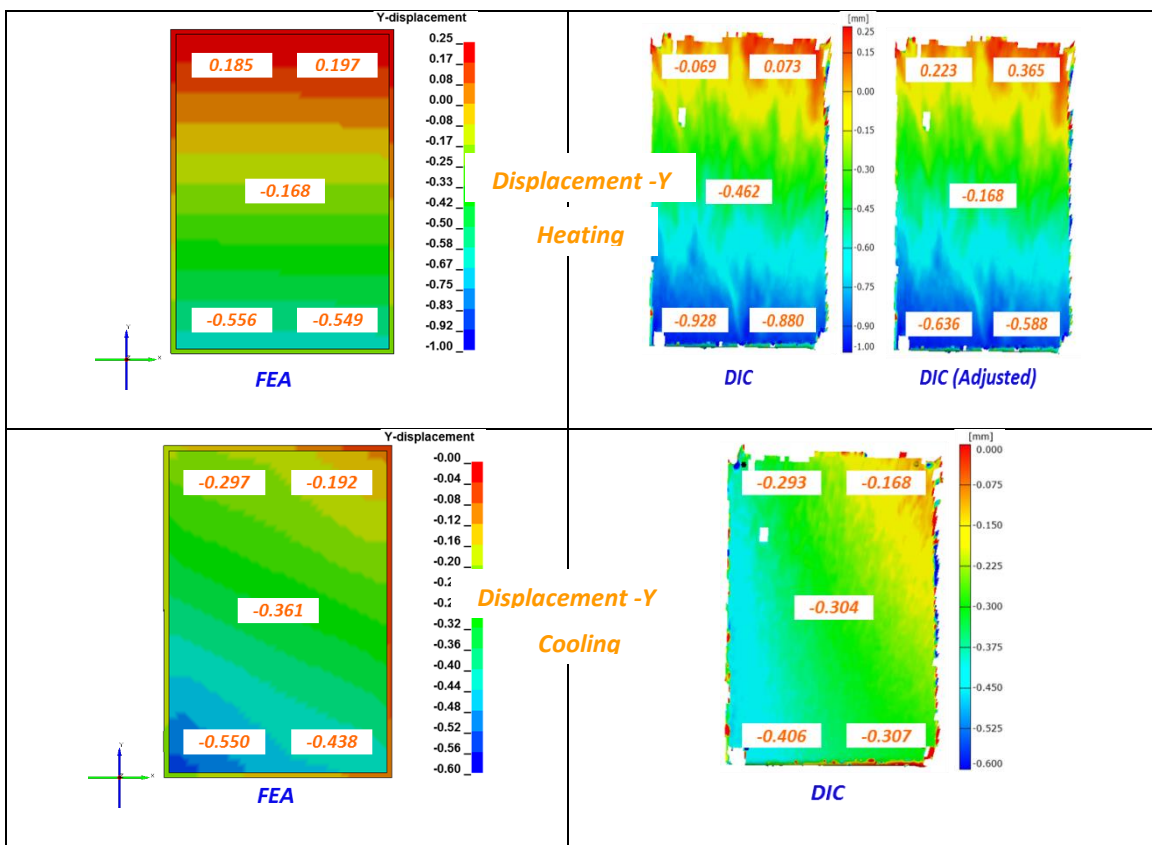


Figure 5.18 Y-displacement prediction from finite element model vs. DIC generated values for Model I

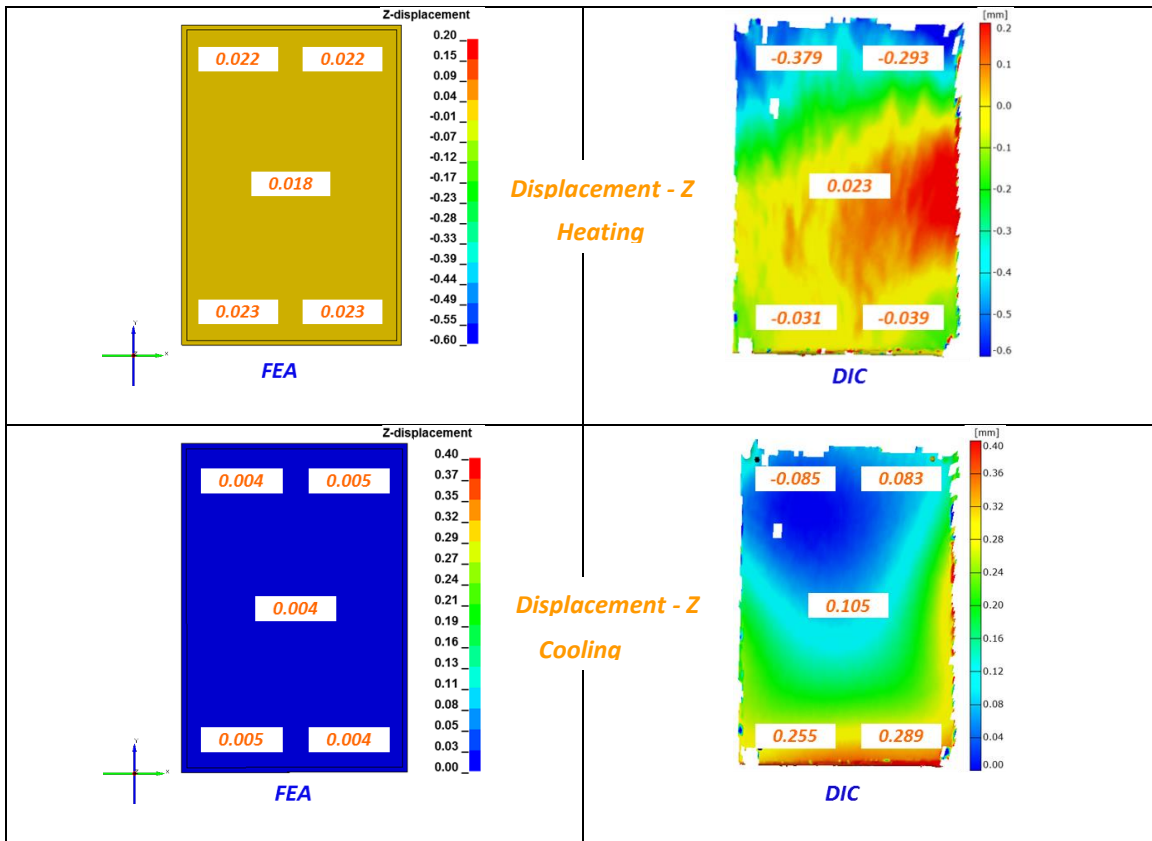


Figure 5.19 Z-displacement prediction from finite element model vs. DIC generated values for Model I

### 5.2.2.2. Model II (with adhesive and mechanical fixations)

The finite element predictions and DIC generated displacements from the experiments with adhesive and mechanical fixations are shown in *Figure 5.20, 5.21, and 5.22*. The displacements in the X, Y and Z direction are shown at the end of the heating phase and the cooling phase. In this case, the aluminum panel was locked in the four directions due to the friction element welds in the periphery of the panel. As the temperature rises, the aluminum panel and the steel frame start expanding in the X and the Y direction, but are constrained in those directions due to the friction element welds. As a result, the aluminum panel starts to bulge up in the Z-direction. Since the adhesive is in the uncured

state at the beginning of the test, the adhesive does not play a major role in the behavior of the roof component in the heating phase. As a result, the aluminum panel expands in the Z-direction. Due to the mechanical fixations, the X and Y displacements across the adhesive bond are much smaller in magnitude as compared to the model I. At the peak temperature, near the end of the heating phase, the adhesive gets fully cured with the panel in an expanded state. In the cooling phase, as the whole system starts to cool down, the aluminum panel and the steel frame start contracting to go back to their initial state. But, the fully cured adhesive puts restriction on the contraction of the panel and frame. As a result, the panel and the steel frame go into an unintended distorted state. There is a residual displacement in the X, Y and Z-direction in the panel.

This behavior is very well represented in the experiments as well as FE predictions. The presence of friction element welds in the circumference of the panel lock the movement in the X and Y directions. Therefore, at the end of heating phase, the X and Y-displacements in the panel are negligible as compared to model I, while the bulging in the Z-direction is significant. At the end of the cooling phase, the magnitude of the displacements fall as a result of contraction, but there is a residual displacement due to the effect of the fully cured adhesive bond. The trend in the displacements in the X, Y and Z directions are similar for the experiments and finite element predictions. On comparing the point displacements, it was found that the values of X and Y-displacement in the experiments were found to be shifted. A small global movement in the whole test specimen inside the furnace may cause the displacements to drift in a certain direction.

To remove this global movement, the displacements in the X and Y-direction were shifted to match the displacement of the center point. The magnitude of relative point displacements after adjusting the DIC values matched the FE predictions to a good level.

Since this case and type of construction is closer to an actual scenario where the roof panel is bonded to the steel roof bows and also fixed by mechanical fixations, the displacements in the Z-direction are of significant importance. The experiments show that the panel bulged in the Z-direction to a significant value, which is also predicted well by the finite element model. This bulge in the center of the aluminum panel is due to the constraints in the circumference causes severe distortion in the roof component. The aluminum panel was modeled as a perfectly flat sheet in finite element, which although is not the case in the experiment, but the magnitude of upward bulging in the panel is high enough to compensate for minor variations in the initial flatness of the panel. The finite element prediction of the displacements in the roof component with adhesive and mechanical fixations shows an acceptable level of agreement with the experimental results.

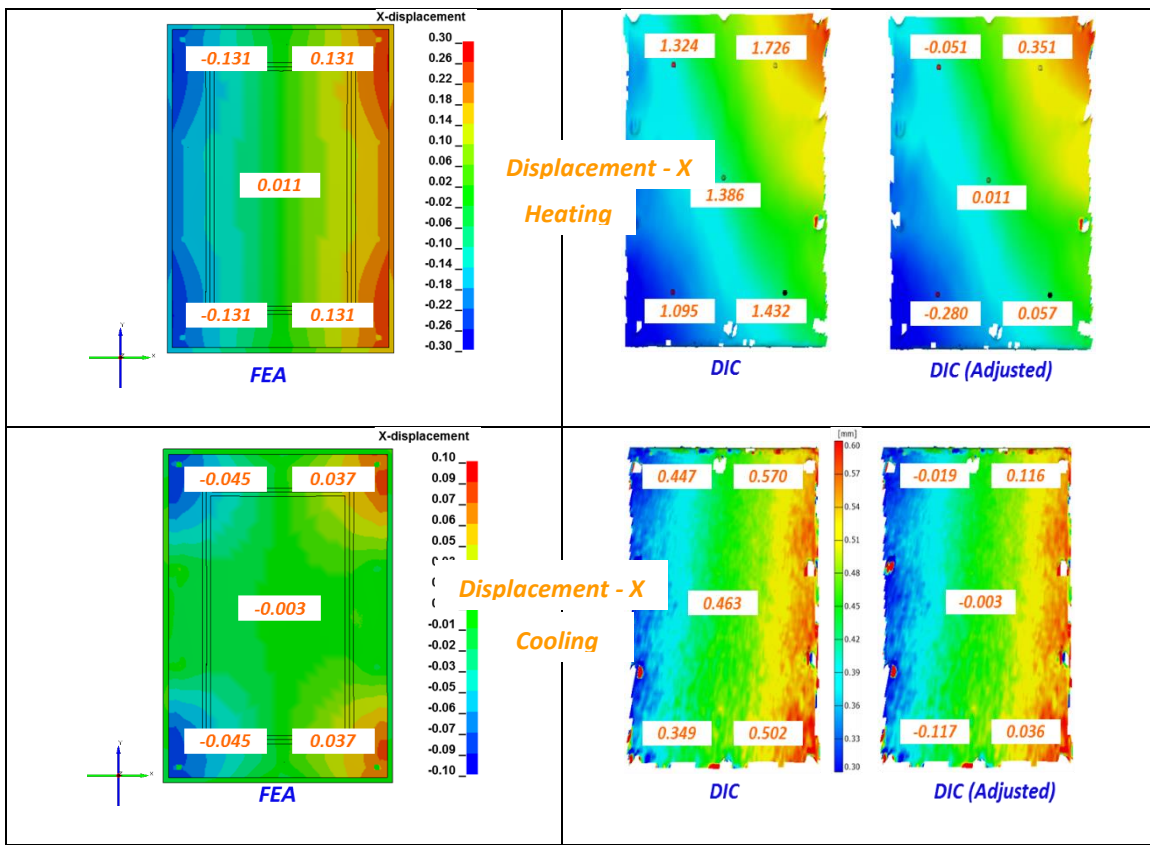
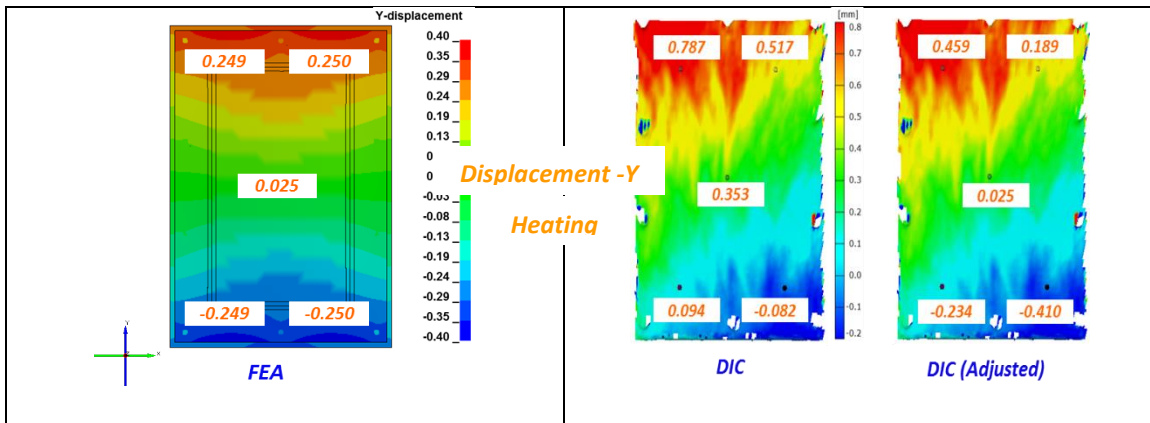


Figure 5.20 X-displacement prediction from finite element model vs. DIC generated values for Model II



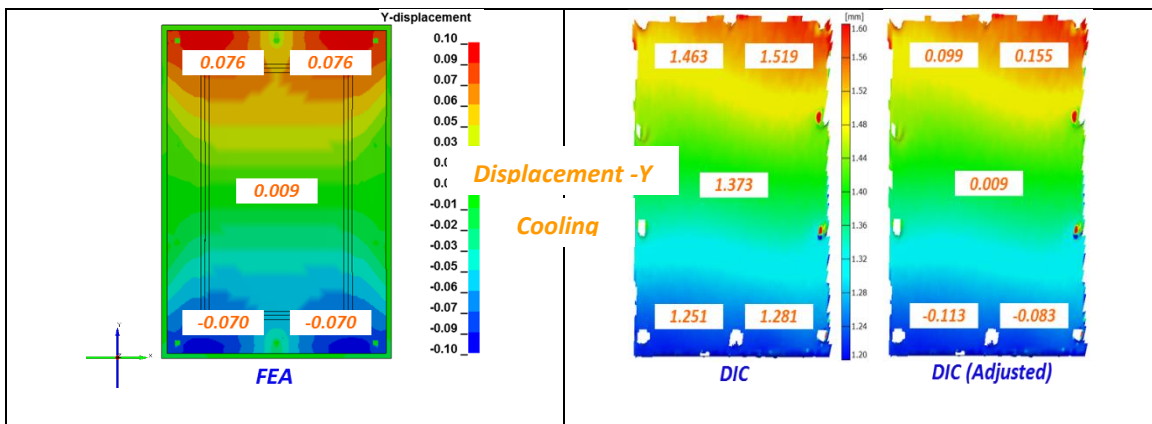


Figure 5.21 Y-displacement prediction from finite element model vs. DIC generated values for Model II

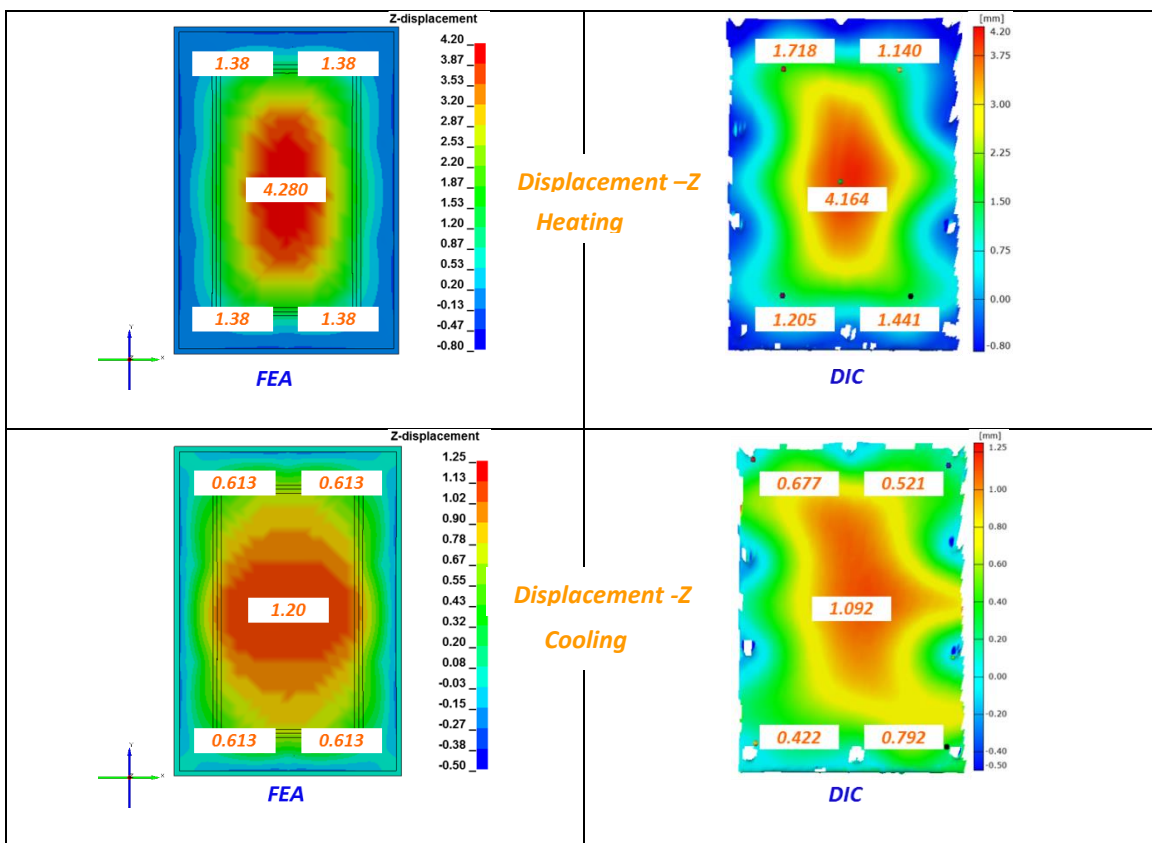


Figure 5.22 Z-displacement prediction from finite element model vs. DIC generated values for Model II

# **Chapter 6**

## **6. CONCLUSIONS**

### **6.1 FEA prediction results**

The finite element model was validated with the experimental results by comparing the general trend of the X, Y and Z displacements and the relative point displacements of chosen five points on the surface of the aluminum panel. Since the FE model predictions were in good agreement with the experiments, the predictions of residual stress state and magnitude in the adhesive bond can be studied with a confidence. The residual stresses developed in the adhesive joint in model I with adhesive only is shown in *Figure 6.1*. If the magnitude of stresses in the adhesive bond is compared to the plastic stress-strain curve of the fully cured adhesive, it accounts for approximately 25% of the yield limit of the adhesive. Such a high level of stresses in the adhesive bond is detrimental to the performance of the adhesive bond in the life cycle of the bonded structure, i.e. roof component.

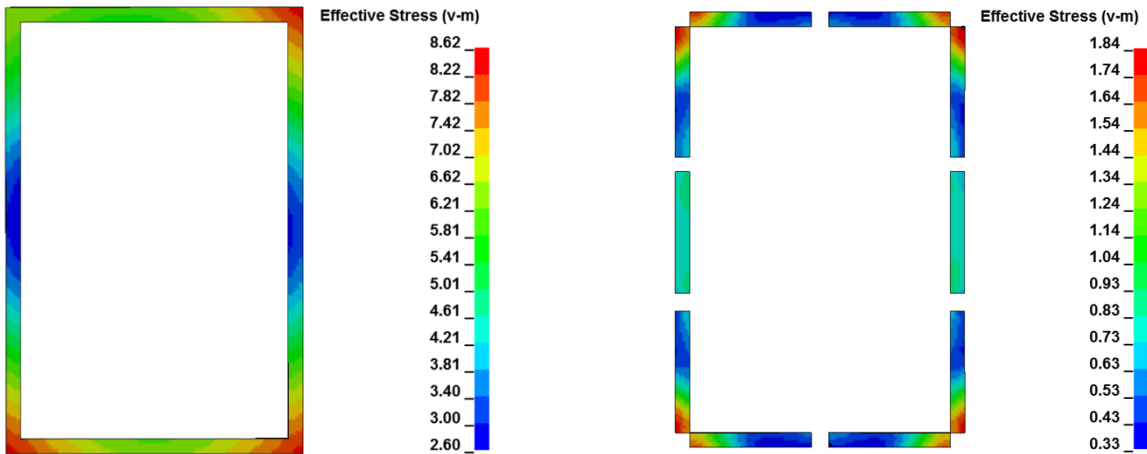


*Figure 6.1 Effective stress in the adhesive bond for model I: with adhesive only (left) and model II: with adhesive and mechanical fixations (right)*

**Effect of mechanical fixations:** The finite element predictions of the effective stress in the adhesive bond for model I and model II show that the addition of mechanical fixations to the model lowers the magnitude of the effective residual stresses. This is due to constraints in the X, Y directions which allow lower level of displacement across the adhesive bondline. The presence of mechanical fixations drops the residual stresses to ~5% of the yield limit of the adhesive. Therefore, the presence of adhesive is better for the adhesive.

Although the presence of fixations in the structure is good for the adhesive bond, it proves to be bad for the geometrical accuracy of the structure. It was observed that the upward bulge in the Z-direction was over 4mm for a 1/36<sup>th</sup> scaled-down model with a relatively high thickness to width ratio of the aluminum panel. The displacement in the Z-direction for model I and model II at the end of heating cycle are shown in *Figure 6.2* for the purpose of comparison.

The magnitude of upward bulging in the roof panel was expected to magnify for a full size 1:1 roof component with aluminum roof panel and steel roof bows. A finite element simulation was performed for a full size BMW X3 roof component (1900 x 1100 x 1.2mm) with fixations. The FE predictions (shown in *Figure 6.3*) showed that the center of the roof component bulged by 35 mm at the peak temperature. This magnitude of displacement will give rise to other practical problems and bonding defects. At this level of bulging, the aluminum panel will not remain in contact with the adhesive applied on the cross-bows and the adhesive will be cured without staying in contact with the two bonding surfaces. Therefore, Z-displacement of such a high order is expected to cause de-bonding in the cross-bows during the curing process of the body structure.

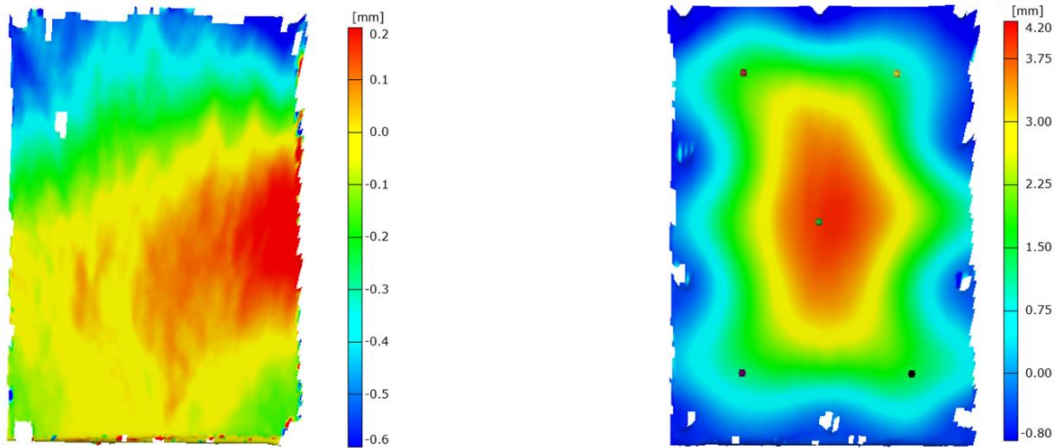


*Figure 6.2 Z-displacement in the aluminum panel at the end of heating cycle for model I: with adhesive only (left) and model II: with adhesive and mechanical fixations (right)*

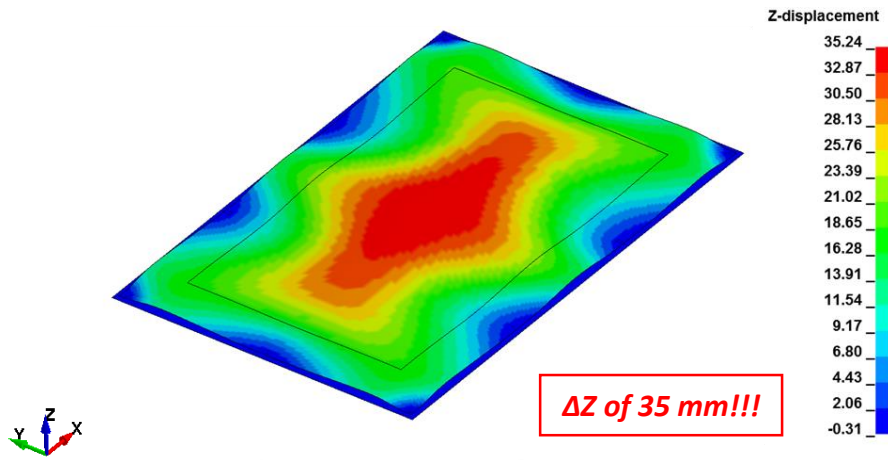


*Figure 6.3 Z-displacement in the aluminum panel for a full size 1:1 roof component with adhesive and mechanical fixations*

**Effect of choice of adhesive:** The choice of adhesive can play a role in the optimization of the bonded structure design. Changing the stiffness of the adhesive can help in changing the magnitude of the residual stresses. *Figure 6.4* shows the effects of having a low stiffness adhesive as compared to a high stiffness adhesive.

An adhesive with a lower modulus will have lower residual stresses in the bond due to the manufacturing induced thermal displacements. It would be beneficial for the adhesive but would have adverse effects on the overall rigidity of the bonded structure. On the other hand, an adhesive with a high modulus will provide high rigidity to the bonded structure, but will give rise to a higher level of manufacturing induced residual stresses.



*Figure 6.4 Effect of the choice of adhesive on the adhesive bond and the body structure stiffness*

## 6.2 Concluding remarks

This work proposed a suite of viscoelastic-plastic models which work in conjunction to predict the manufacturing process induced effects on an adhesive joint. The models were calibrated for an automotive grade structural adhesive EP 5089. The material models were coded into a user-defined material subroutine for LS-DYNA. The developed material card was implemented into finite element simulations for performing two types of component level validations on a roof component with adhesive only and with adhesive and mechanical fixations. The predicted results of the finite element simulations showed good agreement with the experimental results for both the scenarios. The developed approach based on only the viscoelastic-plastic modeling of adhesive gives satisfactory results at component level and sheds light on several important points to consider during the design process.

There are a variety of parameters that play a role in the design process of a lightweight structure: (i) material combination i.e. steel, aluminum, magnesium or CFRP; (ii) adhesive type i.e. low, medium or high stiffness adhesive; (iii) bondline geometry i.e. bondline width and adhesive thickness; (iv) curing cycle (v) fixation design i.e. type, spacing, quantity of joints. The discussed problems were not so significant in a steel intensive structure owing to a low thermal expansion in steel. But, these concerns enlarge in dealing with multi-material structures composed of aluminum or magnesium with relatively higher coefficient of thermal expansion. The developed package of material models and experiments can fill that gap and enable the design of an optimized multi-material lightweight structure by helping in answering the design related critical questions.

## 7. REFERENCES

- Abedrabbo, N., F. Pourboghrat and J. Carsley (2006). "Forming of aluminum alloys at elevated temperatures – Part 2: Numerical modeling and experimental verification." *International Journal of Plasticity* **22**(2): 342-373.
- Abou Msallem, Y., F. Jacquemin, N. Boyard, A. Poitou, D. Delaunay and S. Chatel (2010). "Material characterization and residual stresses simulation during the manufacturing process of epoxy matrix composites." *Composites Part A: Applied Science and Manufacturing* **41**(1): 108-115.
- Adam, G. and J. H. Gibbs (1965). "On the Temperature Dependence of Cooperative Relaxation Properties in Glass-Forming Liquids." *The Journal of Chemical Physics* **43**(1): 139-146.
- Badrinarayanan, P., Y. Lu, R. C. Larock and M. R. Kessler (2009). "Cure characterization of soybean oil-Styrene-Divinylbenzene thermosetting copolymers." *Journal of Applied Polymer Science* **113**(2): 1042-1049.
- Bihamta, R. (2017). "Modeling Adhesive Joints in the Automotive IndustryDevelopments, Challenges, and Future." *Modeling, Simulation and Testing Autmotive Lightweight Materials*.
- Bogetti, G. (1991). "Process-induced stress and deformation in thick section thermoset composite laminates." *Journal of Composite Materials* **26**(5).
- Brauner, C., S. Bauer and A. S. Herrmann (2014). "Analysing process-induced deformation and stresses using a simulated manufacturing process for composite multispar flaps." *Journal of Composite Materials* **49**(4): 387-402.
- Budhe, S., M. D. Banea, S. de Barros and L. F. M. da Silva (2017). "An updated review of adhesively bonded joints in composite materials." *International Journal of Adhesion and Adhesives* **72**: 30-42.
- Cai, H., P. Li, G. Sui, Y. Yu, G. Li, X. Yang and S. Ryu (2008). "Curing kinetics study of epoxy resin/flexible amine toughness systems by dynamic and isothermal DSC." *Thermochimica Acta* **473**(1-2): 101-105.
- Courtois, A., M. Hirsekorn, M. Benavente, A. Jaillon, L. Marcin, E. Ruiz and M. Lévesque (2018). "Viscoelastic behavior of an epoxy resin during cure below the glass transition temperature: Characterization and modeling." *Journal of Composite Materials*: 002199831878122.
- D. Rosu, C. N. C., F. Mustata, C. Ciobanu (2002). "Cure kinetics of epoxy resins studied by non-isothermal DSC data." *Thermochimica Acta* **383**: 119-127.
- da Silva, L. F. M., P. J. C. das Neves, R. D. Adams, A. Wang and J. K. Spelt (2009). "Analytical models of adhesively bonded joints—Part II: Comparative study." *International Journal of Adhesion and Adhesives* **29**(3): 331-341.
- Daoqiang Lu, C. P. W. (2000). "E!ects of shrinkage on conductivity of isotropic conductive adhesives." *International Journal of Adhesion & Adhesives* **20** (2000) (20): 189-193.
- Doolittle, A. K. (1951). "Studies in Newtonian Flow. II. The Dependence of the Viscosity of Liquids on Free-Space." *Journal of Applied Physics* **22**(12): 1471-1475.
- Douglas Adolf, J. E. M. (1996). "Calculation of Stresses in Crosslinking Polymers." *Journal of Composite Materials* **30**(1): 13-34.
- Duemichen, E., M. Javaditehran, M. Erdmann, V. Trappe, H. Sturm, U. Braun and G. Ziegmann (2015). "Analyzing the network formation and curing kinetics of epoxy resins by in situ near-infrared measurements with variable heating rates." *Thermochimica Acta* **616**: 49-60.

- Farahani, S., A. Yelne, F. Akhavan Niaki and S. Pilla (2019). "Numerical Simulation for the Hybrid Process of Sheet Metal Forming and Injection Molding Using Smoothed Particle Hydrodynamics Method." **1**.
- Gyan P. Johari, M. G. (1970). "Viscous Liquids and the Glass Transition. II. Secondary Relaxations in Glasses of Rigid Molecules." *J Chem Phys* **53**(6).
- H. Kazan, S. F., and S. Pilla (2019). "Influences of Process Parameters on Penetration in a Hybrid Single Shot Manufacturing of Carbon Fiber/Epoxy-Polypropylene Structure." *SPE-ANTEC (in press), Detroit, MI.*
- Hardis, R., J. L. P. Jessop, F. E. Peters and M. R. Kessler (2013). "Cure kinetics characterization and monitoring of an epoxy resin using DSC, Raman spectroscopy, and DEA." *Composites Part A: Applied Science and Manufacturing* **49**: 100-108.
- Hossain, M., G. Possart and P. Steinmann (2008). "A small-strain model to simulate the curing of thermosets." *Computational Mechanics* **43**(6): 769-779.
- Hu, J., J. Shan, J. Zhao and Z. Tong (2016). "Isothermal curing kinetics of a flame retardant epoxy resin containing DOPO investigated by DSC and rheology." *Thermochimica Acta* **632**: 56-63.
- Hu, P., X. Han, L. F. M. da Silva and W. D. Li (2013). "Strength prediction of adhesively bonded joints under cyclic thermal loading using a cohesive zone model." *International Journal of Adhesion and Adhesives* **41**: 6-15.
- Jamie M. Kropka, M. E. S. a. R. S. C. (2013). "Role of Residual Stress on the Strength of Adhesive Joints." *Sandia National Laboratories SAND2013-10717C*.
- Javdanitehran, M., D. C. Berg, E. Duemichen and G. Ziegmann (2016). "An iterative approach for isothermal curing kinetics modelling of an epoxy resin system." *Thermochimica Acta* **623**: 72-79.
- Kamal, M. R. (1974). "Thermoset Characterization for Moldability Analysis." *Polymer Engineering & Science*.
- Kazan, H., T. Zheng, S. Farahani and S. Pilla (2019). "Degree of cure, mechanical properties, and morphology of carbon fiber/epoxy- PP hybrids manufactured by a novel single shot method." *Materials Today Communications* **19**: 441-449.
- Khoun, L. and P. Hubert (2010). "Cure shrinkage characterization of an epoxy resin system by two in situ measurement methods." *Polymer Composites* **31**(9): 1603-1610.
- Kim, W. (1996). "Stress Relaxation Behaviour of 3051-6 Epoxy Resin During Cure." *Polymer Engineering and Science*.
- Kim, Y. G. and D. G. Lee (1998). "Influence of Fabrication Residual Thermal Stresses on Rubber-toughened Adhesive Tubular Single Lap Steel-Steel Joints under Tensile Load." *The Journal of Adhesion* **65**(1-4): 163-185.
- KWANSOO CHUNG, O. R. (1993). "A DEFORMATION THEORY OF PLASTICITY BASED ON MINIMUM WORK PATHS." *International Journal of Plasticity* **9**: 907-920.
- Li, G., Z. Huang, P. Li, C. Xin, X. Jia, B. Wang, Y. He, S. Ryu and X. Yang (2010). "Curing kinetics and mechanisms of polysulfone nanofibrous membranes toughened epoxy/amine systems using isothermal DSC and NIR." *Thermochimica Acta* **497**(1-2): 27-34.
- Liu, W., Q. Qiu, J. Wang, Z. Huo and H. Sun (2008). "Curing kinetics and properties of epoxy resin-fluorenyl diamine systems." *Polymer* **49**(20): 4399-4405.
- M. Kaliske, H. R. (1997). "Formulation and implementation of three-dimensional viscoelasticity at small and finite strains." *Computational Mechanics* **19 (1997)** 228 – 239.
- M. Kemal Apalak \*, R. G. (2002). "On non-linear thermal stresses in an adhesively bonded single lap joint." *Computers and Structures* **80**: 85–98.

- Ma, C., Y. Tian, Y. Gong, J. Zhang, H. Qi and C. Wang (2018). "Study of the Effect of Curing Residual Stress on the Bonding Strength of the Single Lap Joint Using a High-Temperature Phosphate Adhesive." *Materials (Basel)* **11**(7).
- Malcolm L. Williams, R. F. L., and John D. Ferry (1955). "The Temperature Dependence of Relaxation Mechanisms in Amorphous Polymers and Other Glass-forming Liquids." *Journal of the American Chemical Society* **77 (14)**: 3701–3707.
- Marques, E. A. S., L. F. M. da Silva, M. D. Banea and R. J. C. Carbas (2014). "Adhesive Joints for Low- and High-Temperature Use: An Overview." *The Journal of Adhesion* **91**(7): 556-585.
- Mauro Zarrelli\*, A. A. S. a. I. K. P. (2002). "Investigation of cure induced shrinkage in unreinforced epoxy resin." *Plastics, Rubber and Composites Processing and Applications* **31(2002)**. **377-384**.
- May, M., H. Voß and S. Hiermaier (2014). "Predictive modeling of damage and failure in adhesively bonded metallic joints using cohesive interface elements." *International Journal of Adhesion and Adhesives* **49**: 7-17.
- Meschut, G., O. Hahn and D. Teutenberg (2014). "Influence of the curing process on joint strength of a toughened heat-curing adhesive." *Welding in the World* **59**(2): 209-216.
- Meuwissen, M. H. H., H. A. de Boer, H. L. A. H. Steijvers, K. M. B. Jansen, P. J. G. Schreurs and M. G. D. Geers (2006). "Prediction of mechanical stresses induced by flip-chip underfill encapsulants during cure." *International Journal of Adhesion and Adhesives* **26**(4): 212-225.
- R.A. Dickie\*, D. R. B., S.M. Ward, D.A. Wagner (1997). "Modeling paint and adhesive cure in automotive applications." *Progress in Organic Coatings* **31 (1997)** **209–216**.
- Reedy, E. D. and T. R. Guess (1996). "Butt joint strength: effect of residual stress and stress relaxation." *Journal of Adhesion Science and Technology* **10**(1): 33-45.
- Ruiz, T. (2004). "Thermomechanical properties furing cure of glass polyester RTM composites." *Journal of Composite Materials* **39**(10).
- S. Farahani, A. F. A., B. M. Dariani, and S. Pilla (2018). "An analytical model for non-hydrostatic sheet metal bulging process by means of polymer melt pressure." *Journal of Manufacturing Science and Engineering*.
- Saseendran, S. (2016). "Effect of Degree of Cure on Viscoelastic Behavior of Polymers." *LTU Thesis*.
- Sheng Dong, A. S., Allen Sheldon (2017). "Modeling of Curing Adhesives between Jointed Steel and Aluminum Plates using MAT\_277 in LS-DYNA." *11th European LS-DYNA Conference 2017, Salzburg, Austria*.
- SINDEE L. SIMON, G. B. M., OLIVIER SINDT "Modeling the Evolution of the Dynamic Mechanical Properties of a Commercial Epoxy During Cure after Gelation." *Journal of Applied Polymer Science Vol. 76*: 495–508.
- Tim Welters, C. H., Manuel Schiel (2013). "Composite\_and\_Multi-material\_Joints\_in\_Body\_Applications." *Henkel AG & Co. KGaA, Internal Report*.
- Travis A. Bogetti, J. W. G. J. (1992). "Process-Induced stress and deformation in thick-section thermoset composite laminates." *Journal of Composite Materials* **26**(5).
- Wang, H., Y. Zhang, L. Zhu, Z. Du, B. Zhang and Y. Zhang (2011). "Curing behaviors and kinetics of epoxy resins with a series of biphenyl curing agents having different methylene units." *Thermochimica Acta* **521**(1-2): 18-25.
- Xiaogang Huang, J. W. G. J., Travis Bogetti (2000). "Process induced stress for woven fabric thick section composite structures." *Composite Structures* **49**: 303-312.
- Yu, Y., I. A. Ashcroft and G. Swallowe (2006). "An experimental investigation of residual stresses in an epoxy–steel laminate." *International Journal of Adhesion and Adhesives* **26**(7): 511-519.

Zhang, J., Y. C. Xu and P. Huang (2009). "Effect of cure cycle on curing process and hardness for epoxy resin." Express Polymer Letters 3(9): 534-541.